

INAUGURAL-DISSERTATION

zur Erlangung der Doktorwürde der
NATURWISSENSCHAFTLICH - MATHEMATISCHEN
GESAMTFAKULTÄT

der

RUPRECHT-KARLS-UNIVERSITÄT
HEIDELBERG

vorgelegt von
Diplom-Mathematiker

Sven Eike Wetterauer

aus Heidelberg

Tag der mündlichen Prüfung: _____

**Design of Numerical Methods for
the Simulation of Multiscale
Lithium Ion Battery Models**

Gutachter: **Dr. Thomas Carraro**

Abstract

In this thesis numerical methods for the solution process of the Newman-type lithium ion battery (LIB) model with a distribution of spherical particles with different radii are derived. Since the Newman-type LIB model is a multiscale model, where the scales cannot be completely separated, it has a pseudo two-dimensional structure. To be solved it needs the solution of a so called cell problem. Furthermore, it consists of a homogenized and a microscopic part that have to be solved coupled. The solution process of the cell problem is done with the CutCell method to improve reconstruction properties of the microstructure. Therefore, the condition number of a Laplace problem with the CutCell method is investigated and it is shown that a simple preconditioner can improve the condition problems due to the CutCell method. Furthermore, a goal oriented a posteriori error estimator based on the dual weighted residual (DWR) method is derived for the CutCell method. For the LIB model the condition number is investigated and a simple preconditioner is suggested. Based on the DWR method a goal oriented error estimator is derived and tested for the pseudo two-dimensional problem. The model behavior of this extension is investigated, especially the occurrence of the different deintercalation properties of the particles with different radii. Furthermore, a simplified model for small charge/discharge rates for an anode is derived and compared to the full model. In the end, the sensitivity of full Newman-type model with respect to two parameters, which are hard to determine experimentally, is investigated.

Zusammenfassung

In dieser Dissertation werden numerische Methoden zur Lösung einer Erweiterung des Lithium Ionen Batterien (LIB) Modells von Newman hergeleitet. Diese Erweiterung beinhaltet die Rekonstruktion des Aktivmaterials mit einer Verteilung von sphärischen Partikeln. Da es sich bei diesem LIB Modell um ein Multiskalenmodell handelt, bei dem sich die Skalen nicht komplett trennen lassen, hat das Modell eine pseudo-zweidimensionale Struktur. Zur Lösung dieses Problems muss zunächst ein sogenanntes Zellproblem gelöst werden. Außerdem besteht dieses Modell aus einem homogenisierten und einem mikroskopischen Teil, die gekoppelt gelöst werden müssen. Um eine bessere Rekonstruktion der Mikrostruktur zu erreichen, wird das Zellproblem mit der CutCell Methode gelöst. Für die CutCell Methode wird die Konditionszahl für ein Laplace Problem untersucht und ein einfacher Vorkonditionierer benutzt, um die Konditionszahl zu verbessern. Außerdem wird ein zielorientierter a posteriori Fehlerschätzer basierend auf der Dual Weighted Residual Methode (DWR) für

die CutCell Methode hergeleitet. Für das LIB Modell wird die Konditionszahl untersucht und eine einfacher Vorkonditionierer vorgeschlagen. Zusätzlich wird für das LIB Modell ein zielorientierter Fehlerschätzer basierend auf der DWR Methode für das pseudo-zweidimensionale Problem hergeleitet und getestet. Das Verhalten der Erweiterung des Batteriemodells wird untersucht, vor allem im Hinblick auf das unterschiedliche Deinterkalationsverhalten der Partikel mit unterschiedlichen Radien. Außerdem wird ein vereinfachtes Modell für kleine Lade- und Entladeraten hergeleitet und mit dem vollen Modell verglichen. Zum Ende der Dissertation werden für das Batteriemodell die Sensitivitäten zweier Parameter, die experimentell nur schwer bestimmt werden können, untersucht.

Contents

1	Introduction	9
1.1	Contributions of the thesis	11
1.2	Overview of thesis	12
2	Derivation of the battery model	15
2.1	Modeling of a lithium ion battery	15
2.1.1	Performance measurement	20
2.2	Homogenization of 3D model	20
2.2.1	Cell problem	26
2.2.2	Concentration in active material	27
2.2.3	Newman model	27
2.3	Extension to a radius distribution	29
3	Methodology for the calculation of effective transport parameters	35
3.1	Introduction	35
3.2	Discretization	38
3.2.1	Finite element method	38
3.2.2	CutCell method	40
3.2.3	Quadrature formula	41
3.3	A priori error estimates	44
3.3.1	Linearization error	44
3.4	Condition number of CutCells	47
3.4.1	Stiffness matrix	50
3.4.2	Preconditioning	54
3.5	Error estimation and adaptivity	55
3.5.1	Reconstruction of the dual solution	60
3.5.2	Refinement strategy	62
3.6	Numerical examples	63
3.6.1	Manufactured solutions	63
3.6.2	Real microstructures	69
3.6.3	Smaller real microstructure	72
3.6.4	Comparison with voxel based solver	75

4	Solution process of LIB model	79
4.1	Newman Model	79
4.1.1	Existence and Uniqueness	83
4.1.2	Discretization	85
4.1.3	Cathode half cell	90
4.1.4	Potential of a half cell	94
4.2	Condition number of the Jacobian matrix	94
4.3	A posteriori error estimate and mesh adaptivity	96
4.3.1	Refinement strategy	107
4.3.2	Efficiency of error estimator	109
4.3.3	Mesh adaptivity	110
4.4	Behavior of LIB model	115
4.4.1	Anode half cell	119
4.5	Simplified model for small charge/discharge rates	126
4.6	Sensitivity of LIB model	130
5	Conclusions	137
5.1	Conclusions	137
	Acknowledgment	141
	Literature	145

1 Introduction

Lithium ion batteries (LIB) already play an important role in daily life as batteries for several electrical devices as mobile phones, laptops, etc. Furthermore, due to the exhaustion of fossil energy resources electromobility has become more and more important in the last years. One main disadvantage of electrical cars so far is the range that can be driven with one battery charge and the recharge time of the battery. Therefore, the improvement of batteries play an important role for the future of electromobility.

Lithium ion batteries have several advantages in comparison to other types of batteries, like a high energy density, low self discharge rates and high cell voltages. In comparison to the advantages, there are also some disadvantages, like special protection against overcharging, worse ageing effects in comparison to other battery types and a high cost factor in production.

The goal of simulations on lithium ion batteries is to help to improve the lifetime and capacity of LIBs. The advantage of simulating the processes in batteries are that adjustments like different used materials or different geometries can be tested rather simply without the need to actually build this battery physically, which might get quite expensive.

A battery consists of several galvanostatic cells. In this thesis only single galvanostatic cells are considered, therefore whenever the term battery is used, actually a single galvanostatic cell is meant. A cell consists of two electrodes, anode and cathode, which are both connected to a current collector and by that with an external electrical circuit. Inside the cell, the space between the electrodes is filled with an electrolyte, which might be solid or liquid. This thesis focuses on liquid electrolytes. In order to prevent short circuits the electrodes are separated in space by the so called separator that might also consist of other materials besides electrolyte.

Both electrode materials in anode and cathode have the ability to intercalate lithium. The difference between a charged and a discharged battery is the storage of lithium in either one of the electrodes. If lithium is stored mainly in the anode, the cell is charged, and if lithium is stored in the cathode, the cell is discharged. The lithium transport between the electrodes is done through the electrolyte. For every lithium ion deintercalated in the anode a single electron migrates through the current collector of the anode and the external electrical circuit to the cathode, providing electrical energy.

Research on lithium ion batteries is a hot topic for quite some time now and many aspects of them are already investigated. Numerical simulations are divided into two different approaches, either on the full 3D model, which is quite expensive in computational time due to its size, or a simplified model, which has a pseudo two-dimensional (P2D) structure. Most groups work on the P2D model, while the full 3D model is only used by a few research groups, for example [35], [37], [30]. The P2D model was first derived by Doyle and Newman, [22], based on a work of Newman [43]. The derivation of Newman was based purely on electrochemical considerations, not on a mathematical framework. There are several publications, which later gave a mathematical framework for the model of Newman. In 2011 Ciucci and Lai gave a derivation of the P2D model by an asymptotic expansion method, [18]. In her PhD thesis, [49], Taralova gave a derivation using rigorous homogenization theory and gave the first comparison between a 3D and a P2D model for different ratios between the macroscopic and the microscopic scale. The well-posedness of the model was only shown in 2018 by J. Díaz and co-authors in the publication [21], who managed to show the existence and uniqueness of the P2D model in weak-mild formulation.

Before the publication of Díaz other groups were also working on the existence and uniqueness of this model, where an important intermediate step was achieved by the group of Dörfler, where Maier showed the existence of a simplified model consisting of two elliptic equations coupled in a similar fashion to the actual LIB model in [23].

The P2D model of Newman reconstructs the electrode material by spheres of a single radius. Since in general the electrodes consist of a microstructure constructed by several particles of different sizes, Ender introduced an extension of the Newman model to comply with the different sizes, [25], [24].

For the solution process of the P2D model two steps are necessary. First a stationary problem needs to be solved on the real microstructure in three space dimensions to calculate effective parameters. The second step is to actually solve the P2D model that uses the effective parameters calculated in the first step.

In both steps partial differential equations need to be solved. Standard numerical methods for the solution of partial differential equations are the finite element method (FEM) [10], the finite difference method or the finite volume method, [5]. In this work the focus is on the finite element method, where the implementation is based on the FEM library deal.II developed by Bangerth, Kanschat and others, [1], [3]. Finite element methods for the solution of problems on a microstructure can be separated into two different kinds, fitted methods and unfitted methods. Fitted methods create a mesh such that the microstructure is resolved by the mesh, this approach is used for example by Frei and Richter [28]. For unfitted methods the mesh does not need to align with the microstructure, but the information of the shape of the microstructure is defined in other ways,

for example in the CutCell method, [12], [14], [15]. The CutCell method can be seen as a variant of the eXtended finite element method (XFEM), that was described by Moës, Dolbow and Belytschko, [41], [47], and also investigated by Hansbo and Hansbo [31], [32] and Burman [13]. For the XFEM, it is well known that ill conditioning can occur, [38]. A method to improve the condition number was given by the ghost cell penalty method as shown by Burman in [11].

The numerical method for the solution of the P2D model is also the finite element method. An improvement of this solution process is done in different ways, for example Farkas, [27] and Iliev, [36], uses an operator splitting method to improve the computation time. In this thesis the dual weighted residual (DWR) method first introduced by Becker and Rannacher, [7], is used to improve the performance of the solution process. The DWR method was further adapted and applied to different problems, [4]. Goll and Carraro, [16], already used the DWR method in an electrochemical framework, where they developed a posteriori error estimators for a coupled system of a homogenized problem and auxiliary problems.

1.1 Contributions of the thesis

In this work the focus is on the investigation of numerical aspects of the solution of the extended P2D model, introduced by Ender. Due to the simplification of Newman's model from a 3D model to a P2D model, the solution process is divided into two parts.

- Calculation of effective parameter by a cell problem.
- Solving the P2D model.

The P2D model needs effective parameter, which have information of the geometry of the microstructure domain. These effective parameters can be calculated by a stationary 3D simulation on the microstructure.

The state of the art way to calculate the effective parameter is to reconstruct the microstructure on a voxel based mesh, which has poor reconstruction properties of the surface of the microstructure domain. In this thesis a variant of the finite element method, the CutCell method, is used to allow better reconstruction properties of the microstructure. Especially the surface of the microstructure can be reconstructed in a better way with the CutCell method.

Form a numerical point of view, the contributions of this work are an investigation of the condition number of the stiffness matrix of a Laplace problem using the CutCell method. The condition number is investigated both numerically and theoretically. An upper bound for the condition number is proven in this thesis, where numerical investigations suggest that the upper bound is not sharp.

Furthermore, a goal oriented a posteriori error estimation based on the dual weighted residual method is derived for the CutCell method. The challenges in this derivation are mainly given by the definition of a proper reconstruction of the exact dual solution, which cannot be done by standard means for the CutCell method.

An a posteriori error estimation is also derived for the extended P2D model by Ender. The biggest challenge in this topic is the actual derivation of the error estimators, which is non standard due to the non standard structure of the model as a pseudo two-dimensional model.

Beside that in this thesis the behavior of the extended P2D model is investigated. The particles of different sizes introduced in this model are intercalated or deintercalated by lithium in a non uniform way. This intercalation behavior and an explanation of this behavior is an important result mainly for the engineering community to understand the processes in a LIB in a better way.

Furthermore, the introduction of an even further simplified model in comparison to the P2D model is given. For specific setups it is shown numerically that the concentration of lithium in the active material is almost constant, therefore the diffusion in the active material is neglected by a volume averaging process. By this process a one-dimensional model is derived and validated under specific conditions.

The last contribution of this thesis is a sensitivity analysis of the P2D LIB model. In the P2D model there are parameters needed that cannot be determined easily in an experiment. Therefore, the sensitivity analysis is a first step in the direction of a parameter estimation process.

1.2 Overview of thesis

The thesis is organized as described in the following. In chapter 2 the derivation of the used lithium ion battery model is shown. Starting from electrochemical considerations first a full lithium ion battery model is derived in section 2.1. The three-dimensional model, derived there, is in general not beneficial, due to high computational costs. These high computational costs are based on the fact that the electrodes of a LIB are in general microstructures that need a fine meshing for the reconstruction of the domain and therefore during the numerical solution of the problems, large equation systems are produced. Therefore, in section 2.2 a simplified model is shown and derived by a homogenization process. This homogenized model was first introduced by Doyle and Newman [22] and the derivation by rigorous homogenization was first done by Taralova [49]. In the community this model is well established and widely used in different commercial software, which are used by many engineers in this field. In the last section of

chapter 2 an extension of the Newman model, done by Ender in his work [25], is shown. The extension of Ender has the advantage of a better reconstruction of the microstructure of the used materials in the electrodes. In this section furthermore an extension of the derivation of Taralova is shown in order to derive Ender's model with rigorous homogenization theory.

In chapter 3 the numerical aspects of the solution of the cell problem are considered. This cell problem generates several numerical difficulties that will be addressed. Since the cell problem needs to be solved on a part of the real microstructure, this microstructure needs to be reconstructed properly, which is done with the CutCell method. Furthermore, an a priori error estimate is shown for the Laplace problem using a CutCell method. In section 3.4 the condition number of the stiffness matrix of a Laplace problem with a CutCell method is considered and also a proper preconditioner is shown in order to reduce a bad condition number introduced by the CutCell method. Furthermore, in order to reduce computational costs local mesh refinement based on goal oriented a posteriori error estimations is shown. This procedure is based on the well known dual weighted residual method (DWR). The DWR method was not yet used for a CutCell method, which produces several challenges in its derivation and implementation. These challenges and the solution thereof are shown in section 3.5. Finally this chapter is closed with numerical examples showing the advantages of the CutCell method and the DWR method for problems on test microstructures and real microstructures.

In chapter 4 numerical aspects of the solution of the LIB model by Ender are considered. The challenges of this model are the structure of the model equations that are defined on a pseudo two-dimensional mesh. This special structure of the model equations is given due to the homogenization process that only homogenizes a part of the model, while another part remains in the microscopic domain. In section 4.1.1 first the publication of Díaz, Gómez-Castro and Ramos [21] is shown that proves existence and uniqueness of this model. Furthermore, in section 4.1.2 the discretization of this model using a finite element method is shown. The discretization is not trivial due to the special coupling of the model equations. Since the LIB model is nonlinear, Newton's method is used for the solution process. In section 4.2 the condition number of the Jacobian matrix needed for Newton's method is considered. Furthermore, a suitable easy preconditioner is shown to reduce the bad conditioning of this matrix. Since the LIB model is time dependent the computational costs can still be high for this model due to the number of used timesteps. In order to reduce the computational costs in every time step again a local mesh refinement based on the DWR method is introduced. In the last sections of this chapter the behavior of Ender's model is considered. The fact that Ender's model uses a better reconstruction of the microstructure influences the charging and discharging behavior of an electrode

depending on the size of the different particles in a microstructure. In section 4.4 this behavior is investigated and explained based on the model equations. The discharge behavior in the anode of the LIB allows for a further simplification of the model by a volume averaging leading to a one-dimensional model. Section 4.5 shows this simplification and the boundaries of its feasibility. In the last section 4.6 of this chapter the sensitivities of this model with respect to two different parameters are considered.

2 Derivation of the battery model

The state of the art model of a lithium ion battery (LIB) is the so called Newman model, which was first introduced by Doyle and Newman in [22]. In this chapter, the derivation of the Newman model will be recapitulated. First the electrochemical processes in a LIB will be explained and based on these, a 3D model will be derived. In a second step the Newman model will be derived using rigorous homogenization theory, as shown by Taralova in her PhD thesis [49]. In the last section of this chapter an extension of the Newman model is shown, which was first introduced by Ender [24], [25]. The derivation of this extension with the help of rigorous homogenization theory was not done before, but will be shown here, by making a minor adjustment of the derivation of Taralova.

2.1 Modeling of a lithium ion battery

A lithium ion battery (LIB) consists of two separated electrodes, the anode and the cathode. The volume between the electrodes is filled with an electrolyte, a fluid or solid material that allows for Li-ion transport. In this work only a liquid electrolyte is considered. Since this volume separates anode and cathode, it is called separator. The electrodes themselves consist of materials, in which lithium can be intercalated and deintercalated. Anode and cathode material need to have different electrochemical potentials, such that lithium ions migrate from anode to cathode. During discharge the following processes occur in a LIB. The initial state is that the lithium ions are concentrated in the anode material. During discharge lithium ions are deintercalated from the anode material into the surrounding electrolyte. For every deintercalated lithium ion one electron migrates from the anode material to the connected current collector (CC). The electron then migrates as an electric current to the current collector of the cathode material and enters the cathode material there. The deintercalated lithium ion migrates through the electrolyte to the cathode material due to the difference in electrochemical potential between the materials. In the cathode material the lithium ions are then intercalated and by a diffusion process distributed in the material.

This process continues until either the lithium concentration in the cathode material is high enough to counter the potential difference between electrode

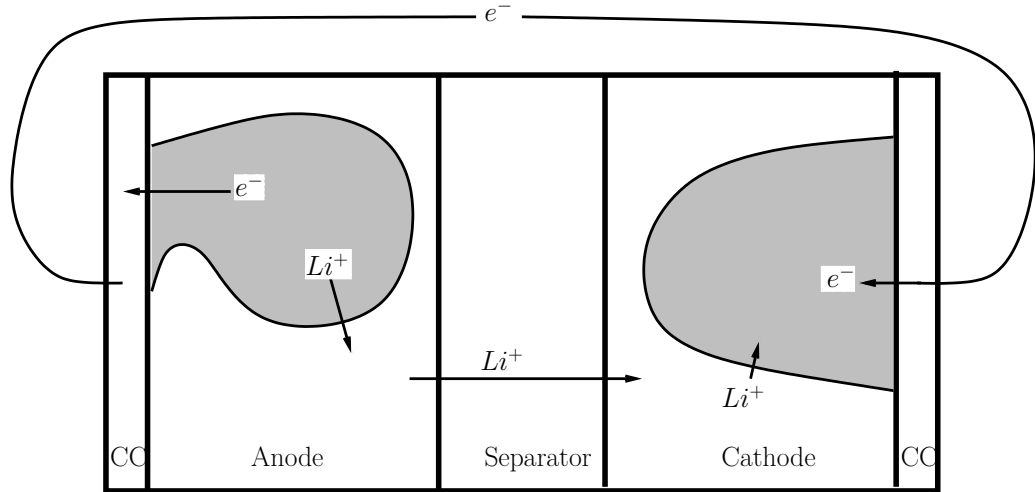


Figure 2.1: Simplified scheme of the dynamic in a LIB during discharge.

materials or until the electrical circuit is interrupted. This whole process is shown schematically in figure 2.1. The intercalation and deintercalation occurs on the surface of the electrode materials. Therefore, a larger surface allows for better intercalation and deintercalation properties and the electrode materials are generally chosen as porous microstructures.

To derive the model equations for these processes, only one electrode and the separator will be considered, since the processes in the electrodes work in the same way and therefore the same model equations hold true.

The half cell consists of two different phases, the material phase and the electrolyte phase, for which the notation Ω_{mat} and Ω_{el} will be used respectively. In figure 2.1 the grey domain corresponds to Ω_{mat} , while the white domain in anode, separator and cathode corresponds to Ω_{el} . In both domains the model needs to address both charge and mass conservation.

In Ω_{mat} the mass conservation is given by Fick's second law, with a flux condition on the boundary due to the intercalation/deintercalation of lithium. The discharge of the LIB is assumed to happen in the time interval $T := (0, t_{end})$.

$$\partial_t c_s - \nabla \cdot (D_s \nabla c_s) = 0 \quad \text{in } T \times \Omega_{mat}, \quad (2.1)$$

$$D_s \partial_n c_s = \frac{j_{ct}}{F} \quad \text{on } T \times \Gamma, \quad (2.2)$$

$$D_s \partial_n c_s = 0 \quad \text{on } T \times \partial\Omega_{mat} \setminus \Gamma, \quad (2.3)$$

$$c_s(0) = c_{s,0} \quad \text{in } \Omega_{mat}. \quad (2.4)$$

The function

$$c_s \in \mathcal{C}^1(T, \mathcal{C}^2(\Omega_{mat}) \cap \mathcal{C}^1(\overline{\Omega_{mat}})) \quad (2.5)$$

describes the distribution of the concentration of lithium ions in the domain Ω_{mat} . The subscript s refers to the fact that this domain consists of a solid material, while the electrolyte is a liquid material. The boundary Γ is defined as the interface between the open domains Ω_{mat} and Ω_{el}

$$\Gamma := \partial\Omega_{mat} \cap \partial\Omega_{el}.$$

The exchange current density j_{ct} describes the flow of current, if lithium is intercalated or deintercalated. The normal vector n on Γ is chosen to be the outside normal of Ω_{mat} , therefore a positive j_{ct} describes intercalation of lithium, while a negative j_{ct} describes deintercalation. Since lithium ions are once positively charged, this current density can be recalculated into a flux of lithium ions with the help of Faraday's constant $F = 96485 \frac{As}{mol}$. On the boundary $\partial\Omega_{mat} \setminus \Gamma$, lithium ions cannot be intercalated and therefore a no flux condition is given there. This boundary marks the transition between the electrode material and the current collector, where only electrons can transit. The function $c_{s,0}$ describes the initial concentration distribution of lithium ions in the material phase Ω_{mat} . The transport of electrons in the material domain Ω_{mat} is described by Ohm's law

$$j = \sigma_s \nabla \phi_s. \quad (2.6)$$

As used above the subscript s refers to the fact that this equation holds true on the solid material domain Ω_{mat} . The function

$$\phi_s \in \mathcal{C}(T, \mathcal{C}^2(\Omega_{mat}) \cap \mathcal{C}^1(\overline{\Omega_{mat}})) \quad (2.7)$$

is the electrical potential in this domain, σ_s the conductivity and j a current density.

The conservation of charge leads to the fact that the divergence of the current density vanishes in the domain Ω_{mat}

$$-\nabla \cdot (\sigma_s \nabla \phi_s) = 0 \quad \text{in } T \times \Omega_{mat}, \quad (2.8)$$

$$\sigma_s \partial_n \phi_s = 0 \quad \text{on } \Gamma_{cc}, \quad (2.9)$$

$$\sigma_s \partial_n \phi_s = j_L \quad \text{on } T \times \partial\Omega_{mat} \setminus (\Gamma \cup \Gamma_{cc}), \quad (2.10)$$

$$\sigma_s \partial_n \phi_s = j_{ct} \quad \text{on } T \times \Gamma. \quad (2.11)$$

Γ_{cc} describes the common boundary with a current collector in anode and cathode. The boundary conditions in this formulation account for the deintercalation

of lithium and the simultaneous transition of electrons from the material phase to the current collector.

In the next step the model equations in the electrolyte will be derived. In this domain the same conservation laws apply, but the theory for transport in concentrated solutions needs to be used [50]. Due to the mass conservation the model equation for the lithium concentration in the electrolyte

$$c_l \in \mathcal{C}^1(T, \mathcal{C}^2(\Omega_{el}) \cap \mathcal{C}^1(\overline{\Omega_{el}})) \quad (2.12)$$

is therefore given by

$$\partial_t c_l - \nabla \cdot (D_l \nabla c_l) = \frac{j}{F} \nabla t_+ \quad \text{in } T \times \Omega_{el}, \quad (2.13)$$

$$D_l \partial_n c_l = (1 - t_+) \frac{j_{ct}}{F} \quad \text{on } T \times \Gamma, \quad (2.14)$$

$$D_l \partial_n c_l = 0 \quad \text{on } T \times \partial\Omega_{el} \setminus \Gamma, \quad (2.15)$$

$$c_l(0) = c_{l,0} \quad \text{in } \Omega_{el}. \quad (2.16)$$

The structure of these model equation is similar to the corresponding equation in the material domain. The subscript l in this case refers to the fact that the electrolyte is in general liquid. The parameter t_+ is the transport number of lithium ions in electrolyte, which will be assumed to be constant in this work. Therefore, the right hand side of equation (2.13) will be $\nabla t_+ = 0$.

For concentrated solutions the electrochemical potential in electrolyte

$$\phi_l \in \mathcal{C}(T, \mathcal{C}^2(\Omega_{el}) \cap \mathcal{C}^1(\overline{\Omega_{el}})) \quad (2.17)$$

can be derived by Ohm's law together with charge conservation and therefore yields the model equations

$$-\nabla \cdot (\sigma_l \nabla \phi_l) - \nabla \cdot (\kappa \nabla \log(c_l)) = 0 \quad \text{in } T \times \Omega_{el}, \quad (2.18)$$

$$\sigma_l \partial_n \phi_l = j_{ct} \quad \text{on } T \times \Gamma, \quad (2.19)$$

$$\sigma_l \partial_n \phi_l = 0 \quad \text{on } T \times \partial\Omega_{el} \setminus \Gamma. \quad (2.20)$$

The coefficient κ is defined as

$$\kappa := \sigma_l \frac{2RT}{F} (1 - t_+) \left(1 + \frac{\partial \log(f_{\pm})}{\partial \log(c_l)}\right) \quad (2.21)$$

in this equation. In this definition the temperature T , the molar gas constant $R = 8.314 \frac{\text{kg m}^2}{\text{s}^2 \text{mol K}}$ and the mean molar activity coefficient f_{\pm} of the electrolyte is used.

The electrochemical details of this derivation can be found in literature, for example [22], [25], [30] and [35].

These four sets of model equations, (2.1)-(2.4), (2.8)-(2.11), (2.13)-(2.16) and (2.18)-(2.20), together define the model equations for the processes in a lithium ion battery electrode. The equations build a set of two parabolic concentration equations for the lithium concentrations c_l and c_s in the material and the electrolyte phase and two elliptic equations describing the behavior of the electrochemical potential ϕ_l and the electrical potential ϕ_s in the two phases. All four model equations are coupled by an exchange current density that describes the intercalation or deintercalation of lithium in the material domain.

Exchange current density

The coupling between the model equations is given by an exchange current density, which can be modeled with the help of a Butler-Volmer equation, as Doyle and Newman described in their work [29].

$$j_{ct} = j_0 \left(\exp\left((1 - \alpha)\frac{RT}{F}\eta\right) - \exp\left(\alpha\frac{RT}{F}\eta\right) \right), \quad (2.22)$$

$$j_0 = kF (c_l)^\alpha \left(1 - \frac{c_l}{c_{s,max}} \right)^{1-\alpha} (c_s)^\alpha, \quad (2.23)$$

$$\eta = \phi_s - \phi_l - \phi_{OCV}(c_s) - \frac{RT}{F} \log\left(\frac{c_l}{c_{l,0}}\right). \quad (2.24)$$

The term η describes the overpotential of this system at every point in time, $c_{s,max}$ is theoretical maximal concentrations of lithium ions in the active material. The maximal concentration is a theoretical value, since speaking from an electrochemical point of view, it would be possible to intercalate lithium into the active material without a boundary. But at some point the lithium would irreversibly destroy the structure of the active material, which cannot be modeled by these model equations. Therefore, a maximal concentration is applied to the exchange current density. Furthermore in this definition the open circuit voltage ϕ_{OCV} is defined. This voltage describes the potential difference between anode and cathode at different states of charge.

From the set of equations for the potential in the material phase (2.8), a condition on the exchange current density can be derived using a Gaussian theorem

$$\int_{\Gamma_{cc}} j_L dx = \int_{\Omega_{mat}} \nabla \cdot (\sigma_s \nabla \phi_s) dx - \int_{\Gamma} j_{ct} dx \quad (2.25)$$

$$= - \int_{\Gamma} j_{ct} dx. \quad (2.26)$$

This condition has to hold true also from a physical point of view, since for every lithium ion that is deintercalated a single electron migrates from the active material to the current collector.

The computation of a solution of the above model yields several challenges. The model is defined in three space dimensions, which in general makes computations slow due to a large number of degrees of freedom. Furthermore, the above problem is defined on a microstructure, therefore dealing with two different space scales, which makes discretization of this model complex and is increasing the number of degrees of freedom even more.

To get rid of the two space scales, a homogenization procedure is done on this model, which will be described in section 2.2.

2.1.1 Performance measurement

To measure the performance of a battery the potential difference between the current collectors of anode and cathode is measured. During a charge or discharge cycle of a battery a constant current density j_L is applied to the battery. This parameter is applied to the model as a Neumann boundary condition for the electrical potential ϕ_s , as seen in equation (2.10).

For a constant current density the potential difference between anode and cathode is measured, as a function over time.

Definition 2.1.1 (Potential of the battery). *Let ϕ_s be the solution of the LIB model, to be more precise the solution of equations (2.8)-(2.11). The measurement of interest will be called potential curve in the remainder of this thesis and is defined as a function*

$$\Phi : T \rightarrow \mathbb{R}, \tag{2.27}$$

$$t \mapsto \frac{1}{|\Gamma_{cathode}|} \int_{\Gamma_{cathode}} \phi_s(x, t) dx - \frac{1}{|\Gamma_{anode}|} \int_{\Gamma_{anode}} \phi_s(x, t) dx. \tag{2.28}$$

In this notation Γ_{anode} and $\Gamma_{cathode}$ describe the interface of the active material with the current collectors of anode and cathode respectively.

Remark 2.1.2. *The potential curve is defined here as a function of time. In literature it is often defined as a function of the state of charge, [25], or the (specific) capacity of the battery, [20], [39]. These other definitions are in general a linear transformation of the above definition, since both state of charge and the capacity can be calculated as linear functions of the time.*

2.2 Homogenization of 3D model

The specifics discussed in this section are given in the work of Taralova, [49]. For a general framework on homogenization theory, the book of Hornung [34] is

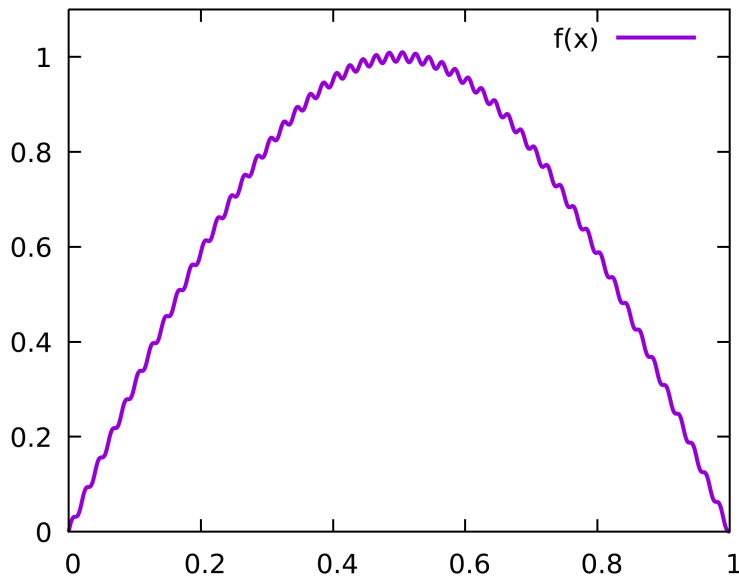


Figure 2.2: Example for a function that can be split into macroscopic and microscopic behavior, $f(x) = \sin(\pi x) + 0.01 \sin(100\pi x)$.

referred. In her thesis, Taralova gave a mathematical derivation of the so called Newman model, which is derived by rigorous homogenization of the 3D model. In this section this derivation will be recapitulated shortly.

The principle idea of homogenization theory is that the behavior of a function can be split into two parts, the macroscopic and the microscopic part. The macroscopic part describes the behavior over the whole domain of interest, while the microscopic part describes the behavior based on local aspects of the model equations. In figure 2.2 this splitting is shown for an exemplary function, in which the macroscopic behavior is half a period of a sin function and the microscopic behavior is also a sin function with a much smaller period. The overall behavior of this function is a half period of a sine functions, while the local, microscopic behavior shows small oscillations. For a given model equation both the macroscopic and the microscopic behavior of the solution is included, therefore both parts are connected to each other. Problems like this for example occur on microstructures, as the electrodes of a LIB. The overall solution behavior is here influenced by local features of the solution, given by the coupling with the microstructure material.

Depending on the goal functional of interest, the exact microscopic behavior of the solution might not be relevant and a proper macroscopic behavior of the so-

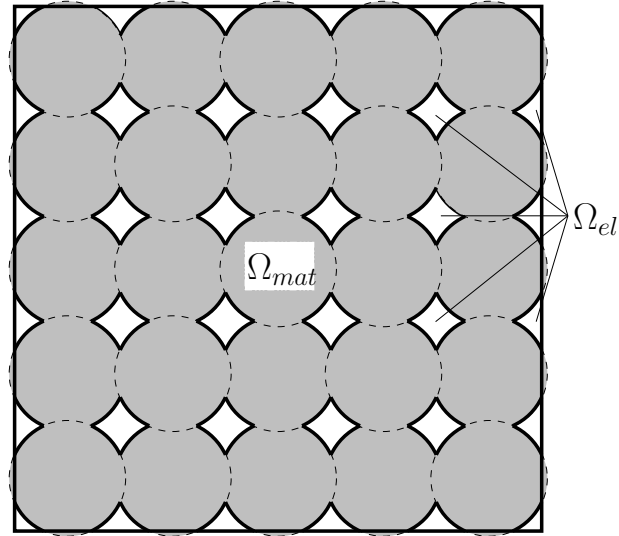


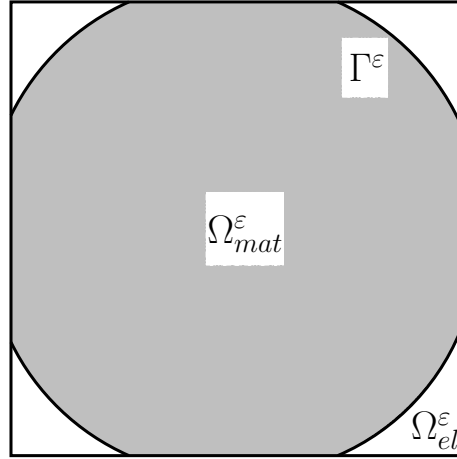
Figure 2.3: Periodic microstructure, reconstructing a single electrode of a LIB.

lution could be a good enough approximation to compute the given functional. Therefore, the goal of homogenization is to define a model describing the macroscopic behavior of the solution, without taking into account all local solution aspects. This process leads to a simpler model, since the solution of a system of equations on the microstructure might lead to very slow solution processes, since the microstructure might lead to a big effort for a correct reconstruction. A solution process only on the macroscopic domain is much faster.

In short, the goal of homogenization theory is to derive a set of model equations on the macroscopic domain, such that the influence of the microscopic solution aspects on the macroscopic solution is maintained. This is done, by taking into account the different length scales of the macroscopic and the microscopic domains. The quotient of the length scales will be described as a parameter ε in this section. The derivation of the set of macroscopic equations is then done by considering the limit process of $\varepsilon \rightarrow 0$.

To describe the homogenization process, Ω_{mat} and Ω_{el} are assumed to be periodic. Even more, Ω_{mat} is assumed to consist of touching spheres, as depicted in figure 2.3. In this case, figure 2.4 shows a periodicity cell Y . For the electrolyte domain in the periodicity cell Y the notation Ω_{el}^ε is used, while Ω_{mat}^ε describes the material domain inside Y . For the interface between the domains Ω_{mat}^ε and Ω_{el}^ε the notation Γ^ε is used.

During the derivation of the macroscopic solution behavior, both length scales need to be considered. Therefore, the variable x will be used for the macroscopic


 Figure 2.4: Periodicity cell Y .

domain, while the variable $y = \frac{x}{\varepsilon}$ describes the microscopic behavior. The homogenization process, will now be only shown for the model equation describing the concentration in electrolyte.

$$\begin{aligned}
 \partial_t c_l - \nabla \cdot (D_l \nabla c_l) &= 0 && \text{in } T \times \Omega_{el}, \\
 D_l \partial_n c_l &= \frac{(1 - t_+) j_{ct}}{F} && \text{on } T \times \Gamma, \\
 D_l \partial_n c_l &= 0 && \text{on } T \times \partial\Omega_{el} \setminus \Gamma, \\
 c_l(0) &= c_{l,0} && \text{in } \Omega_{el}.
 \end{aligned}$$

Due to the splitting of the solution behavior in macroscopic and microscopic parts, several replacements can be done in these model equations.

$$\begin{aligned}
 c_l(x) &\rightarrow c_l\left(x, \frac{x}{\varepsilon}\right) = c_l(x, y), \\
 \nabla &\rightarrow \nabla_x + \frac{1}{\varepsilon} \nabla_y.
 \end{aligned}$$

Applying these properties into the equation, yields the equation

$$\partial_t \chi c_l - \left(\nabla_x + \frac{1}{\varepsilon} \nabla_y \right) \cdot \left(D_l \chi \left(\nabla_x + \frac{1}{\varepsilon} \nabla_y \right) c_l \right) = 0 \quad \text{in } \Omega,$$

where additionally the Heaviside function was used

$$\begin{aligned} \chi : \Omega &\rightarrow \mathbb{R}, \\ \chi(x) &\mapsto \begin{cases} 1, & \text{if } x \in \Omega_{el}, \\ 0, & \text{if } x \in \Omega_{mat}, \end{cases} \end{aligned}$$

to describe this equation on the whole domain $\Omega = \Omega_{mat} \cup \Omega_{el}$. The solution $u = c_l$ is expanded into different powers of ε

$$u(x, y) = u_0(x, y) + \varepsilon u_1(x, y) + \varepsilon^2 u_2(x, y) + \mathcal{O}(\varepsilon^3),$$

where the term $u_0(x, y)$ describes the macroscopic behavior of the solution. Applying this expansion, the terms of the model equation can be sorted by the different powers of ε . The terms with a factor of ε^{-2} yield the equation

$$\nabla_y \cdot (D_l \chi \nabla_y u_0(x)) = 0.$$

Together with the periodicity in the variable y , this equation shows that u_0 is constant in the variable y ,

$$u_0(x, y) = u_0(x).$$

The ε^{-1} terms yield the equation

$$\nabla_y \cdot (D_l \chi (\nabla_x u_0(x) + \nabla_y u_1(x, y))) = 0, \quad (2.29)$$

where the fact that $u_0(x)$ is independent of y was used again. The ε^0 terms yield the equation

$$\chi \partial_t u_0(x) = \nabla_x \cdot (D_l \chi (\nabla_x u_0(x) + \nabla_y u_1(x, y))) \quad (2.30)$$

$$+ \nabla_y \cdot (D_l \chi (\nabla_x u_1(x, y) + \nabla_y u_2(x, y))). \quad (2.31)$$

This equation will now be integrated over the periodicity cell and scaled with the volume of the periodicity cell Y . Since the periodicity cell is defined on the microscopic scale, this is an integration over the y variable.

$$\delta \partial_t u_0(x) = \nabla_x \cdot (D_l (\delta \nabla_x u_0(x) + \frac{1}{|Y|} \int_Y \chi \nabla_y u_1(x, y))) dy \quad (2.32)$$

$$+ \frac{1}{|Y|} \int_Y \nabla_y \cdot (D_l \chi (\nabla_x u_1(x, y) + \nabla_y u_2(x, y))) dy, \quad (2.33)$$

with the porosity $\delta := \frac{|\Omega_{el}^\varepsilon|}{|Y|} = \frac{|\Omega_{el}|}{|\Omega|}$.

Remark 2.2.1. *In literature the notation for the porosity is commonly ε or ε_l . Since the same notation is used for the quotient of the length scales, the porosity is denoted by δ in this chapter. Later, in chapter 4, the more common notation ε_l for the porosity will be used.*

Using a Gaussian theorem this leads to

$$\delta \partial_l u_0(x) = \nabla_x \cdot (D_l(\delta \nabla_x u_0(x) + \frac{1}{|Y|} \int_Y \chi \nabla_y u_1(x, y))) dy \quad (2.34)$$

$$+ \frac{1}{|Y|} \int_{\Gamma_\varepsilon} \chi n \cdot (D_l(\nabla_x u_1(x, y) + \nabla_y u_2(x, y))) dy, \quad (2.35)$$

where the term on $\partial Y \setminus \Gamma_\varepsilon$ vanishes due to the periodicity of u .

Before proceeding with the derivation of the homogenized model, equation (2.26) will be considered with respect to ε . Due to the fact that ε describes the difference in the length scales of the macroscopic and microscopic domains, it can be shown that the number $N(\varepsilon)$ of periodic cells in the whole domain Ω behaves like $N(\varepsilon) = \mathcal{O}(\varepsilon^{-3})$.

$$I = \int_{\Gamma_{cc}} j_L dx = \int_{\Gamma} j_{ct} dx \quad (2.36)$$

$$= \sum_{i=1}^{N(\varepsilon)} \int_{\Gamma_\varepsilon} j_{ct} dy \quad (2.37)$$

$$= \frac{1}{\varepsilon^3} \int_{\hat{\Gamma}_\varepsilon} \varepsilon^2 j_{ct} d\hat{y}, \quad (2.38)$$

where the microscopic boundary Γ_ε in the periodicity cell and the transformation of the periodicity cell to a unit cell was used. Further using the fact that the total flux I is independent of ε , this result yields

$$j_{ct} = \mathcal{O}(\varepsilon). \quad (2.39)$$

By using the expansion of c_l and the corresponding expansions of ϕ_l and ϕ_s it can be shown that

$$j_{ct} = \varepsilon j_{ct,0} + \mathcal{O}(\varepsilon^2), \quad (2.40)$$

with a $j_{ct,0}$ independent of the microscopic variable y .

Sorting the boundary condition by powers of ε , the equations

$$D_l n \cdot \nabla_y u_0(x) = 0, \quad (2.41)$$

$$D_l n \cdot (\nabla_x u_0(x) + \nabla_y u_1(x, y)) = 0, \quad (2.42)$$

$$D_l n \cdot (\nabla_x u_1(x, y) + \nabla_y u_2(x, y)) = \frac{1-t_+}{F} j_{ct,0}, \quad (2.43)$$

are derived. Applying the last equation to (2.35) yields

$$\delta\partial_t u_0(x) = \nabla_x \cdot \left(D_t(\delta\nabla_x u_0(x) + \frac{1}{|Y|} \int_Y \chi \nabla_y u_1(x, y)) \right) dy \quad (2.44)$$

$$+ \frac{1}{|Y|} \int_{\Gamma_\varepsilon} \frac{1-t_+}{F} j_{ct,0} dy. \quad (2.45)$$

Since the exchange current density $j_{ct,0}$ is independent of y , the last term in this equation can be further simplified

$$\frac{1}{|Y|} \int_{\Gamma_\varepsilon} \frac{1-t_+}{F} j_{ct,0} dy = a_{spec} \frac{1-t_+}{F} j_{ct,0}, \quad (2.46)$$

with the specific surface area $a_{spec} := \frac{|\Gamma_\varepsilon|}{|Y|} = \frac{|\partial\Omega_{mat} \cap \partial\Omega_{el}|}{|\Omega|}$.

Remark 2.2.2. *It should be mentioned that in this derivation the following identities were used*

$$\frac{|\Omega_{el}^\varepsilon|}{|Y|} = \frac{|\Omega_{el}|}{|\Omega|} = \delta, \quad (2.47)$$

$$\frac{|\Gamma_\varepsilon|}{|Y|} = \frac{|\Omega_{el} \cap \Omega_{mat}|}{|\Omega|} = a_{spec}, \quad (2.48)$$

which follow directly from the periodicity of the domain Ω .

The last step in the homogenization of the concentration equation in electrolyte is to define the so called cell problem.

2.2.1 Cell problem

The cell problem is an auxiliary problem that helps to get rid of the term containing u_1 in (2.34). Therefore, the cell problem is defined as

Problem 2.2.3 (Cell problem). *For $j = 1, 2, 3$, find the Y -periodic solutions w_j that solve the equations*

$$\nabla_y \cdot \nabla_y w_j = 0 \quad \text{in } \Omega_{el}^\varepsilon, \quad (2.49)$$

$$n \cdot \nabla_y w_j = -e_j \cdot n \quad \text{on } \Gamma_\varepsilon. \quad (2.50)$$

With the help of the solutions w_j of this auxiliary problem, equation (2.29) with boundary condition (2.42) can be solved for u_1

$$u_1(x, y) = \sum_{j=1}^3 \frac{\partial u_0}{\partial x_j}(x, t) w_j(y). \quad (2.51)$$

Due to this explicit representation of u_1 , equation (2.34) can be rewritten as

$$\delta \partial_t u_0(x) = \nabla_x \cdot (D_l^{eff} \nabla_x u_0(x)) + a_{spec} \frac{1-t_+}{F} j_{ct,0}, \quad (2.52)$$

with the effective diffusion tensor

$$(D_l^{eff})_{ij} = \frac{1}{|Y|} \int_{\Omega_{el}^\varepsilon} (D_l)_{ij} \left(\frac{\partial w_j}{\partial y_i}(y) + \delta_{ij} \right) dy. \quad (2.53)$$

In this equation δ_{ij} describes the Kronecker delta distribution.

Remark 2.2.4. *Although this cell problem is derived from a rigorous homogenization theory, the state of the art cell problem that is generally used to calculate effective parameter for a LIB model, is a different one. The state of the art cell problem will be discussed in section 3.1. To the knowledge of the author, a comparison between the rigorous cell problem and the state of the art cell problem was not yet done at this point.*

The derivation of the potential equations both in electrolyte and the active material can be done in the same way.

2.2.2 Concentration in active material

The behavior of the concentration c_s in the active material depends strongly on the charge or discharge current j_L . This is known by physical considerations and microscopic simulations, [49]. The distribution of c_s in the active material is uniform for small currents and it is nonuniform for larger currents. Therefore, the solution behavior of c_s could not be captured adequately, if the corresponding equation would be homogenized.

Consequently, the derivatives in equation (2.1) depend only on the microscopic variable y .

$$\partial_t c_s - \frac{1}{\varepsilon^2} \nabla_y \cdot (D_s \nabla_y c_s) = 0 \quad \text{in } \Omega_{mat}^\varepsilon, \quad (2.54)$$

$$\frac{1}{\varepsilon^2} D_s n \cdot \nabla_y c_s = \frac{1}{\varepsilon} \frac{j_{ct}}{F} \quad \text{on } \Gamma_\varepsilon. \quad (2.55)$$

With the help of the exchange current density j_{ct} , this model equation couples with the homogenized model equations point wise for almost all $x \in \Omega$.

2.2.3 Newman model

In the derivation of the homogenized model only the concentration equations (2.13) - (2.16) were considered. The concentration equation in the particles was

not considered, because it needed special treatment, since it was not homogenized, but remains in the microscopic framework. The concentration equation in the electrolyte was prototypically considered to show the homogenization process. Both potential equations can be homogenized in the same way as the concentration equation.

This procedure finally results in the partly homogenized LIB model

Problem 2.2.5 (Homogenized LIB model pseudo 3D). *Find the solutions c_l , ϕ_l and ϕ_s , defined in the spaces*

$$c_l \in \mathcal{C}^1(T, \mathcal{C}^2(\Omega) \cap \mathcal{C}^1(\overline{\Omega})), \quad (2.56)$$

$$\phi_l \in \mathcal{C}^0(T, \mathcal{C}^2(\Omega) \cap \mathcal{C}^1(\overline{\Omega})), \quad (2.57)$$

$$\phi_s \in \mathcal{C}^0(T, \mathcal{C}^2(\Omega) \cap \mathcal{C}^1(\overline{\Omega})), \quad (2.58)$$

such that the equations

$$\delta \partial_t c_l = \nabla \cdot (D_l^{eff} \nabla c_l) + \frac{1-t_+}{F} a_{spec} \dot{j}_{ct} \quad \text{in } \Omega, \quad (2.59)$$

$$0 = \nabla \cdot (\sigma_l^{eff} \nabla \phi_l) + a_{spec} \dot{j}_{ct} \quad \text{in } \Omega, \quad (2.60)$$

$$0 = \nabla \cdot (\sigma_s^{eff} \nabla \phi_s) - a_{spec} \dot{j}_{ct} \quad \text{in } \Omega, \quad (2.61)$$

with boundary conditions

$$D_l^{eff} \partial_n c_l = 0 \quad \text{on } \Gamma_{cc}^{hom}, \quad (2.62)$$

$$D_l^{eff} \partial_n c_l = D_l^{eff} \partial_n c_l^{sep} \quad \text{on } \Gamma_{sep}^{hom}, \quad (2.63)$$

$$D_l^{eff} \partial_n c_l = 0 \quad \text{on } \partial\Omega \setminus (\Gamma_{cc}^{hom} \cup \Gamma_{sep}^{hom}), \quad (2.64)$$

$$\sigma_l^{eff} \partial_n \phi_l = 0 \quad \text{on } \Gamma_{cc}^{hom}, \quad (2.65)$$

$$\sigma_l^{eff} \partial_n \phi_l = \sigma_l^{eff} \partial_n \phi_l^{sep} \quad \text{on } \Gamma_{sep}^{hom}, \quad (2.66)$$

$$\sigma_l^{eff} \partial_n \phi_l = 0 \quad \text{on } \partial\Omega \setminus (\Gamma_{cc}^{hom} \cup \Gamma_{sep}^{hom}), \quad (2.67)$$

$$\sigma_s^{eff} \partial_n \phi_s = 0 \quad \text{on } \Gamma_{cc}^{hom}, \quad (2.68)$$

$$\sigma_s^{eff} \partial_n \phi_s = 0 \quad \text{on } \Gamma_{sep}^{hom}, \quad (2.69)$$

$$\sigma_s^{eff} \partial_n \phi_s = 0 \quad \text{on } \partial\Omega \setminus (\Gamma_{cc}^{hom} \cup \Gamma_{sep}^{hom}), \quad (2.70)$$

hold true.

For every $x \in \Omega$, find the solution

$$c_s \in \mathcal{C}(T, \mathcal{C}^2(\Omega_{mat}^\varepsilon) \cap \mathcal{C}^1(\overline{\Omega_{mat}^\varepsilon})), \quad (2.71)$$

such that the equation

$$\partial_t c_s = \frac{1}{\varepsilon^2} \nabla_y \cdot (D_s \nabla_y c_s) \quad \text{in } \Omega_{mat}^\varepsilon, \quad (2.72)$$

$$\frac{1}{\varepsilon^2} D_s \partial_n c_s = \frac{1}{F \varepsilon} j_{ct} \quad \text{on } \partial \Omega_{mat}^\varepsilon, \quad (2.73)$$

holds true.

For both sets of equations, the exchange current density, as defined in (2.24), needs to be fulfilled.

In this problem setting, the boundaries of the domain Ω was split into several parts, Γ_{sep}^{hom} is the common boundary between the electrode and separator, Γ_{CC}^{hom} the common boundary between electrode and the current collector.

Due to the shape of the domain Ω and the boundary conditions (2.64), (2.67) and (2.70), the homogenized equations are constant in two space directions. Therefore, the homogenized equations can be considered only in one space dimension. The concentration equation in the active material needs to be solved for every $x \in \Omega$ in the periodicity cell. The domain Ω_{mat}^ε is a sphere with radius R . If the diffusion tensor D_s is anisotropic or at least shows a radial symmetry, only the radial component of this equation needs to be considered. Therefore, this concentration equation can also be considered in only one space dimension.

Figure 2.5 shows a summary of the homogenization process. Starting with a 3D microstructure, due to the homogenization process a 1D homogenized domain is created, coupled with a microscopic problem on the periodicity cell.

Due to the way, the homogenized and the particle equations are coupled, this results in a model, which has a pseudo 2D structure, as depicted in figure 2.6. For the homogenized equations a 1D domain Ω_{hom} is defined. For every point $x \in \Omega_{hom}$, a second 1D domain Ω_r is defined, the boundary of which is coupled to the solutions on Ω_{hom} . The domain Ω_r is only shown for several points $x \in \Omega_{hom}$. The domain $\Omega_{hom} \times \Omega_r$ has a 2D structure, but since the differential operator of the particle equation is defined only in the direction of Ω_r , the system of equation is only of pseudo 2D structure (P2D).

2.3 Extension to a radius distribution

The Newman model, as described in the previous section, is the state of the art model for the simulation of the processes in a LIB. In this model, the active material is reconstructed by spheres of the same radius. Since in real microstructures, the active material particles might be of very different sizes, Ender defined a variant of the Newman model allowing a reconstruction of the active material by several spherical particles with a distribution of radii, [24], [25].

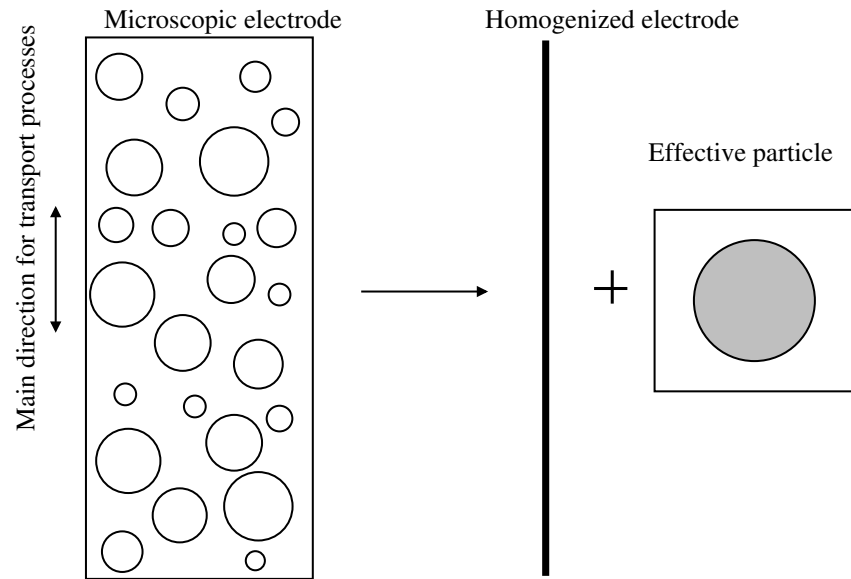


Figure 2.5: Scheme of the homogenization process resulting in a pseudo two-dimensional domain.

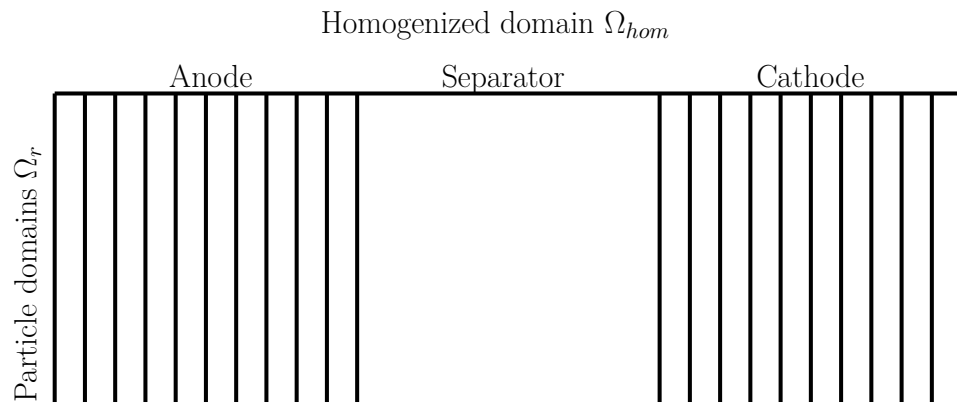


Figure 2.6: Sketch of the pseudo 2D structure of the battery.

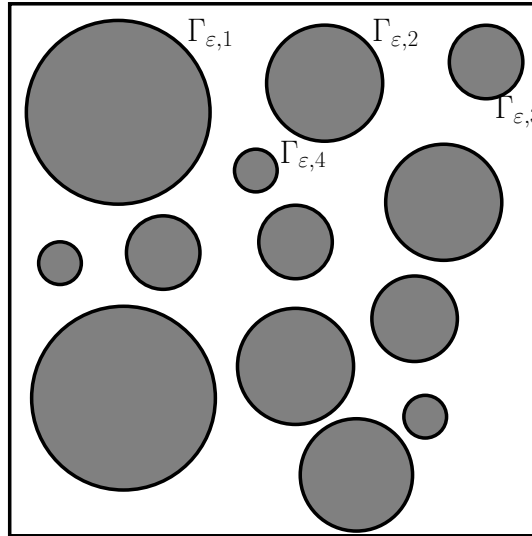


Figure 2.7: Modified periodicity cell Y for a radius distribution. The grey area corresponds to Ω_{mat} , while the white area depicts Ω_{el} .

The model of Ender was only defined as an extension of the Newman model, but was not derived using rigorous homogenization theory. In the following, the homogenization process, described in the work of Taralova, will be slightly modified to show that the model of Ender can also be derived using this approach. Basically the only modification in the derivation of Taralova, is to define the periodicity cell in a different way. The microstructure should be reconstructed using spherical particles satisfying a suitable distribution of radii.

In the following it is assumed that the distribution of radii contains N_R different radii, with the volume fractions vol_i for $i = 1, \dots, N_R$. The volume fraction defines the volume contribution of the particles of radius R_i to the volume of the complete microstructure.

For this given distribution of radii, a periodicity cell is defined that contains a distribution of spheres, such that the given volume fractions are fulfilled, as depicted in figure 2.7. This different definition of the periodicity cell, influences the homogenization process in two different steps. First the step of replacing the 3D particle equation (2.55) by a 1D equation using spherical symmetry, produces now N_R 1D equations.

Remark 2.3.1. *Due to the homogenization process the homogenized solutions c_l , ϕ_l and ϕ_s are constant in a periodicity cell. Therefore, all spheres with the same radius behave in the same way and can be represented by a single 1D equation. The number of spheres with the same radius is taken into account by using the*

volume fraction.

The second step that changes is equation (2.46).

$$\frac{1}{|Y|} \int_{\Gamma_\varepsilon} \frac{1-t_+}{F} j_{ct,0} dy = \sum_{i=1}^{N_R} \frac{1}{|Y|} \int_{\Gamma_{\varepsilon,i}} \frac{1-t_+}{F} j_{ct,0,i} dy \quad (2.74)$$

$$= \sum_{i=1}^{N_R} a_{spec,i} \frac{1-t_+}{F} j_{ct,0,i}. \quad (2.75)$$

In this notation $\Gamma_{\varepsilon,i}$ describes the surface of the spheres with radius R_i , and $a_{spec,i}$ the corresponding specific surface area.

For real microstructures in general only the total specific surface area can be measured. With the help of the volume fraction vol_i the fraction of specific surface for the radius R_i can be described by the formula

$$a_{spec,i} = a_{spec,tot} \frac{vol_i R_i^{-1}}{\sum_i vol_i R_i^{-1}}, \quad (2.76)$$

as described by Ender in his work, [24]. This formula can be derived by deriving a connection between the volume fraction vol_i and the number n_i of spheres of radius R_i in the periodicity cell. With the help of n_i the specific surface area for radius R_i can be described by

$$a_{spec,i} = n_i \frac{4\pi R_i^2}{|Y|} = \frac{3\delta vol_i}{R_i}. \quad (2.77)$$

Since the total specific surface area $a_{spec,tot}$ is the sum thereof, equation (2.76) can be derived.

Independent of the extension to a distribution of radii, Ender describes in his work, that an additional scaling factor for the boundary condition (2.73) of the particle equation is needed. This is due to the fact that in the homogenized equations, a specific surface area a_{spec} of the real microstructure is used. This real specific surface area does not need to coincide with the specific surface area of the spheres in the periodicity cell. Therefore, an additional scaling of the boundary condition is needed, in order to maintain mass conservation. This scaling is achieved by the ratio of the real specific surface area a_{spec} and the specific surface area $\frac{3}{(1-\delta)vol_i R_i}$ of a sphere with radius R_i , where the porosity δ was used.

With the above derivation, finally the extension of the Newman model, introduced by Ender in his work [24] and [25], can be formulated. To formulate this problem, the notation Ω_{R_i} will be used to describe the 1D domain in direction of the radius of a sphere with radius R_i . The problem will be formulated for a single electrode, defined by the domain $\Omega_{hom} = (x_{cc}, x_{sep})$, the boundaries of this domain are the current collector and the separator.

Problem 2.3.2. *Find the solutions*

$$c_l \in \mathcal{C}^1(T, \mathcal{C}^2(\Omega_{hom}) \cap \mathcal{C}^1(\overline{\Omega_{hom}})), \quad (2.78)$$

$$\phi_l \in \mathcal{C}(T, \mathcal{C}^2(\Omega_{hom}) \cap \mathcal{C}^1(\overline{\Omega_{hom}})), \quad (2.79)$$

$$\phi_s \in \mathcal{C}(T, \mathcal{C}^2(\Omega_{hom}) \cap \mathcal{C}^1(\overline{\Omega_{hom}})), \quad (2.80)$$

such that the equations

$$\delta \partial_t c_l = \partial_x (D_l^{eff} \partial_x c_l) + \frac{1-t_+}{F} q_{ct} \quad \text{in } \Omega_{hom}, \quad (2.81)$$

$$0 = \partial_x (\sigma_l^{eff} \partial_x \phi_l) + \partial_x \frac{2RT}{F} \sigma_l^{eff} (1-t_+) \left(1 + \frac{\partial \log f_{\pm}}{\partial c_l}\right) \partial_x c_l + q_{ct} \quad \text{in } \Omega_{hom}, \quad (2.82)$$

$$0 = \partial_x (\sigma_s^{eff} \partial_x \phi_s) - q_{ct} \quad \text{in } \Omega_{hom}, \quad (2.83)$$

with boundary conditions

$$D_l^{eff} \partial_x c_l(x_{cc}) = 0 \quad D_l^{eff} \partial_x c_l(x_{sep}) = D_l^{eff} \partial_x c_l^{sep}(x_{sep}), \quad (2.84)$$

$$\sigma_l^{eff} \partial_x \phi_l(x_{cc}) = 0 \quad \sigma_l^{eff} \partial_x \phi_l(x_{sep}) = \sigma_l^{eff} \partial_x \phi_l^{sep}(x_{sep}), \quad (2.85)$$

$$\sigma_s^{eff} \partial_x \phi_s(x_{cc}) = j_L \quad \sigma_s^{eff} \partial_x \phi_s(x_{sep}) = 0, \quad (2.86)$$

hold true. Simultaneously, for every $x \in \Omega_{hom}$ and for $i = 1, \dots, N_R$, find a solution

$$c_{s,i} \in \mathcal{C}^1(T, \mathcal{C}^2(\Omega_{R_i}) \cap \mathcal{C}^1(\overline{\Omega_{R_i}})), \quad (2.87)$$

such that the equation

$$\partial_t c_{s,i} = \frac{1}{r^2} \partial_r D_s r^2 \partial_r c_{s,i} \quad \text{in } \Omega_{R_i}, \quad (2.88)$$

$$D_s \partial_r c_{s,i}(R_i) = \frac{3a_{spec,i}}{(1-\delta)vol_i R_i F} j_{ct,i}, \quad (2.89)$$

$$c_{s,i}(0, r) = c_{s,0}. \quad (2.90)$$

holds true. Both sets of equations are coupled by a Butler Volmer equation j_{ct} , defined by (2.24).

In this problem setting, the functions c_l^{sep} and ϕ_l^{sep} are concentration and potential solutions in the separator, for which a continuous flux condition is assumed. To define the model problem in the separator, the same model equations hold true, but only the concentration c_l and the potential ϕ_l need to be considered, since there is no active material in the separator domain.

Parameter	Description
δ	porosity of electrolyte phase
D_l	ionic diffusion coefficient in electrolyte
D_s	ionic diffusion coefficient in active material
σ_l	conductivity in electrolyte
σ_s	conductivity in active material
t_+	transference number
F	Faraday constant
f_{\pm}	molar activity coefficient
R	molar gas constant
T	temperature
a_{spec}	specific surface area
k	reaction rate

Table 2.1: Summary of all needed parameters.

Remark 2.3.3. *A comparison between problem 2.2.5 and 2.3.2 shows that there is an inconsistency in the derivation of the LIB model. In model 2.3.2 the microscopic equation of the particles has been written in a variable that is not scaled with ε . During the homogenization of the model $\varepsilon \rightarrow 0$ is considered. Since the particle equation is not homogenized, but remains in the microscopic domain, it is defined for a specific ε . This inconsistency is a result of this partial homogenization procedure.*

Since this model depends on several parameter, table 2.1 shows a summary of all needed parameter to define the model.

3 Methodology for the calculation of effective transport parameters

In this chapter the cell problem to calculate effective transport parameters is considered. Like mentioned in remark 2.2.4 the state of the art cell problem is not the one derived by rigorous homogenization theory, problem 2.2.3. The state of the art cell problem will first be described in this chapter. The remainder of the chapter then is about the solution process of this cell problem. First the discretization with the CutCell method is explained, then the bad condition number of the CutCell method is considered. The chapter closes with an a posteriori error estimation for this problem setting and its quality as refinement indicators for local mesh refinement.

3.1 Introduction

The state of the art method to calculate effective diffusion parameter is to compare the flux of a Laplace equation with mixed boundary conditions on a homogenized domain with the flux of the same problem on a representative volume element (RVE), as described for example by Tjaden, Brett and Shearing [51]. A RVE is a subdomain of the real microstructure, which has to be chosen such that the RVE is representative from the microscopic point of view. As a Laplace equation needs to be solved on the RVE, it should be chosen as small as possible to reduce computational costs. Ideally, if the microstructure is periodic, the RVE should be chosen as the periodicity cell, like describe in section 2.2. In realistic setups the microstructure is not periodic and therefore the choice of the correct size of the RVE is not known a priori.

The RVE is an open domain Ω , which is in general chosen such that it has the shape of a cuboid. The domain Ω subdivides into two other domains, the electrolyte domain and active material domain. It will be assumed now that the effective parameter should be calculated on the active material domain, which will therefore be denoted as Ω_{micro} .

The effective diffusion parameter can be calculated for each direction in space separately, the calculation in the z-direction will be shown. Therefore, the notation Γ_u and Γ_d for the opposing boundaries of Ω in z-direction and Γ for the

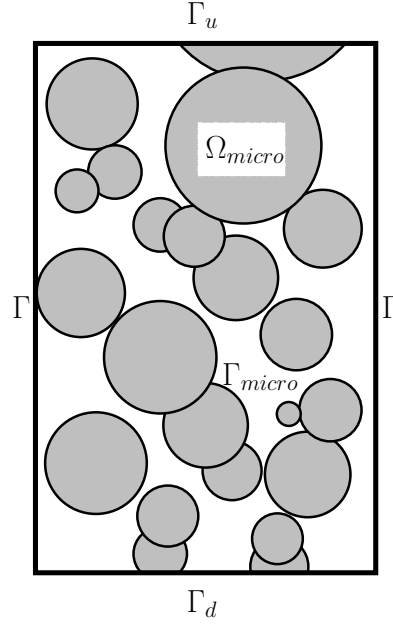


Figure 3.1: Sketch to explain the used notation.

rest of the boundary is used, as depicted in the following figure 3.1.

The domain Ω_{micro} has to have a non empty intersection with both boundaries Γ_u and Γ_d . If this would not be the case, diffusion in this direction would not be possible and therefore the RVE would not have been chosen in a proper way. The remainder of the boundary of Ω_{micro} will be denoted by Γ_{micro} . In general the domain Ω_{micro} will also have non empty intersection with the boundary Γ , but this is not necessarily needed.

After introducing the domain and some notation, the cell problem on the microstructure domain can be formulated:

Problem 3.1.1. Find the solution $u \in C^2(\Omega_{micro}) \cap C(\overline{\Omega_{micro}})$, such that the following equations hold:

$$-\nabla \cdot (D_{bulk} \nabla u) = 0 \quad \text{in } \Omega_{micro}, \quad (3.1)$$

$$u = 0 \quad \text{on } \Gamma_d, \quad (3.2)$$

$$u = 1 \quad \text{on } \Gamma_u, \quad (3.3)$$

$$D_{bulk} \partial_n u = 0 \quad \text{on } \Gamma_{micro}. \quad (3.4)$$

Depending on the active material used in the lithium ion battery, the bulk diffusion parameter $D_{bulk} = D_{bulk}(x)$ can depend on the spatial domain. This considerations are restricted to the easier case of a constant bulk parameter and

therefore $D_{bulk} = 1$ can be assumed. This can be easily seen as the parameter D_{bulk} can be canceled out in the above equations, if it is constant.

Although only a Laplace equation is considered, existence and uniqueness of this problem is not given in general, due to the complicated domain Ω_{micro} . Therefore, the above problem is reformulated in weak formulation, where existence and uniqueness is given by standard results.

Problem 3.1.2. *Find the solution $u \in U := H_d^1(\Omega_{micro})$ such that the following equation holds true:*

$$(\nabla u, \nabla \varphi)_{\Omega_{micro}} = 0 \quad \forall \varphi \in V := H_0^1(\Omega_{micro}). \quad (3.5)$$

Here H_d^1 describes the subset of the Sobolev space H^1 of functions that already fulfill the above Dirichlet boundary condition. H_0^1 denotes the subset of H^1 of functions that have compact support on $\Gamma_u \cup \Gamma_d$.

Definition 3.1.3 (Sobolev spaces). *The Sobolev space H^1 is the space of functions, that are bounded with respect to the H^1 norm,*

$$H^1(\Omega) := \{f : \Omega \rightarrow \mathbb{R} : \|f\|_{H^1(\Omega)} < \infty\}, \quad (3.6)$$

with

$$\|f\|_{H^1(\Omega)}^2 := \|f\|_{L^2(\Omega)}^2 + \|\nabla f\|_{L^2(\Omega)}^2. \quad (3.7)$$

In this definition the L^2 norm

$$\|f\|_{L^2(\Omega)}^2 := \int_{\Omega} |f|^2 dx \quad (3.8)$$

was used.

Since this problem should be compared with the similar problem on the homogenized domain, which is given by Ω , the homogenized problem is defined as:

Problem 3.1.4. *Find the solution $u_{hom} \in C^2(\Omega) \cap C(\bar{\Omega})$, such that the following equations hold:*

$$-\nabla \cdot (D_{eff} \nabla u_{hom}) = 0 \quad \text{in } \Omega, \quad (3.9)$$

$$u_{hom} = 0 \quad \text{on } \Gamma_d, \quad (3.10)$$

$$u_{hom} = 1 \quad \text{on } \Gamma_u, \quad (3.11)$$

$$D_{eff} \partial_n u_{hom} = 0 \quad \text{on } \Gamma. \quad (3.12)$$

Due to the shape of Ω and the given boundary conditions, the existence and uniqueness of this problem are trivially given. An explicit solution can even be formulated very easily, since a function linear in z -direction solves this problem:

$$u_{hom} = \frac{z}{L}. \quad (3.13)$$

With L the length of the domain Ω in z -direction is denoted.

After defining the problem on the micro domain and the homogenized domain, finally the effective diffusion parameter D_{eff} can be calculated by comparing the fluxes of the two problems over the boundary Γ_d .

The fluxes of these two problems are given by:

$$I_{micro} = D_{bulk} \int_{\Gamma_d \cap \partial\Omega_{micro}} \partial_n u do, \quad (3.14)$$

$$I_{hom} = D_{eff} \frac{|\Gamma_d|}{L}. \quad (3.15)$$

Therefore, the effective diffusion parameter is determined as

$$D_{eff} = D_{bulk} \frac{L}{|\Gamma_d|} \int_{\Gamma_d \cap \partial\Omega_{micro}} \partial_n u do. \quad (3.16)$$

In this derivation the crucial step is the solution of the problem on the microstructure domain, 3.1.2. Therefore, in the rest of this chapter, the solution process of this problem is considered further.

3.2 Discretization

3.2.1 Finite element method

In this section the solution process for problem 3.1.2 will be shown. There are different methods to solve this problem, for example the finite difference method, the finite volume method, [5] or the finite element method [10], [17], [8]. In this thesis the finite element method (FEM) is used, to be more precise the FEM variant called CutCells method, which is able to define a microstructure domain Ω_{micro} by an unfitted mesh.

The idea of the FEM is to define finite dimensional spaces U_h and V_h and to approximate the problem 3.1.2 on these spaces. The solution process is rather simple, as the problem can then be rewritten as a system of linear equations.

In general a finite element is a triple $(\mathcal{T}_h, Q_k, \Sigma)$ consisting of a mesh \mathcal{T}_h , a polynomial space Q_k and the space of degrees of freedom Σ . The mesh \mathcal{T}_h is a

set of closed subsets K of Ω_{micro} , such that the following conditions hold true:

$$\mathring{K}_1 \cap \mathring{K}_2 = \emptyset \quad \forall K_1 \neq K_2 \in \mathcal{T}_h, \quad (3.17)$$

$$\bigcup_{K \in \mathcal{T}_h} K = \overline{\Omega_{micro}}. \quad (3.18)$$

Generally the cells K are chosen to be either tetrahedra or hexahedra. In this thesis the FEM is used on hexahedra, since the FEM library deal.II [1], [3] is used for the implementation, which only considers hexahedra.

For computational reasons (a priori estimate and condition number) the mesh has to fulfill certain criteria for the radius h_K of a ball containing the cell K and the radius ρ_K of a ball contained in K need to be fulfilled

- Shape regularity: $\max_{K \in \mathcal{T}_h} \frac{h_K}{\rho_K} \leq c_1$,
- Size regularity: $\max_{K \in \mathcal{T}_h} \rho_K \leq c_2 \min_{K \in \mathcal{T}_h} h_K$.

To define the finite dimensional space U_h on this mesh, the space of trilinear polynomials on the unit cell $\hat{K} = (0, 1)^3$ is considered

$$Q_1 = \text{span}(1, x_1, x_2, x_3, x_1x_2, x_1x_3, x_2x_3, x_1x_2x_3).$$

For every cell K a transformation T_K of the unit cell \hat{K} to the cell K is used to define the cell-wise representation of the functions in the finite element space

$$\begin{aligned} U_h &= \{v \in C(\Omega_h) : v|_K \circ T_K \in Q_1, v = g_D \text{ on } \Gamma_D\}, \\ V_h &= \{v \in C(\Omega_h) : v|_K \circ T_K \in Q_1, v = 0 \text{ on } \Gamma_D\}. \end{aligned}$$

For simplicity the Dirichlet condition was written as a function g_D , where $\Gamma_D = \Gamma_u \cap \Gamma_d$ describes the whole Dirichlet boundary. It should be mentioned that depending on the choice of the transformation that the curvature of the boundary $\partial\Omega_{micro}$ is not represented correctly, but for example represented piecewise linear. Therefore, the condition $\bigcup_{K \in \mathcal{T}_h} K = \overline{\Omega_{micro}}$ might not be fulfilled entirely close to the boundary. Moreover the union of the cells create a new domain Ω_h .

Σ is the set of degrees of freedom. To be more precise it is a set of linearly independent functionals such that every $\varphi \in U_h$ is defined uniquely by these functionals. A typical choice, which will also be used throughout this work, is to use point evaluations for a given basis of U_h as functionals in Σ . Since a Lagrangian basis of U_h is used, this type of finite element is called Lagrangian finite element.

With the help of these finite dimensional spaces, the discretized version of 3.1.2 can be written

Problem 3.2.1. Find the solution $u_h \in U_h$ such that the following equation holds true:

$$(\nabla u_h, \nabla \varphi_h)_{\Omega_h} = 0 \quad \forall \varphi_h \in V_h. \quad (3.19)$$

For further information of standard FEM the books of Brenner and Scott, [10], Ciarlet, [17] and Braess, [8], are referred.

The problem with standard FEM is the creation of the mesh. Since the microstructure can be complicated, it is not easy to create a mesh representing the domain Ω_{micro} . Therefore, a variant of the FEM that can cope with the complicated microstructure, the so called CutCell method, is used.

3.2.2 CutCell method

For the CutCell method, a cuboid domain containing the domain Ω_{micro} is defined. Such a domain was already used, since the homogenized domain Ω , fulfills this condition. The domain Ω has the big advantage that it has a simple structure and it is easy to define a mesh on the domain. Since the domain of interest Ω_{micro} is only a subset of the domain Ω , the cells of this mesh can be distinguished between three different kinds:

- A cell can be contained in Ω_{micro} ,
- it can be only partially contained in Ω_{micro} ,
- or it cannot be contained at all.

To distinguish between the three kinds of cells, the domain Ω_{micro} is represented with the help of the level-set method, [44]. Therefore, a function that has the property to have different signs in the two domains Ω_{micro} and $\Omega \setminus \Omega_{micro}$ is defined

$$\phi(x) \begin{cases} < 0 & \text{for } x \in \Omega \setminus \Omega_{micro} \\ = 0 & \text{for } x \in \partial\Omega_{micro} \setminus \partial\Omega \\ > 0 & \text{for } x \in \Omega_{micro}. \end{cases} \quad (3.20)$$

This function is called level-set function. The most basic idea of such a function is to choose a signed distance function:

$$\phi(x) = \min_{y \in \partial\Omega_{micro}} \|x - y\|.$$

With the help of the level-set function, the three different kinds of cells can be distinguished, by evaluating the function in all nodes of the cell. If different signs occur the cell is only partially in the domain Ω_{micro} , otherwise depending on the sign it is either completely contained in the domain or not contained at all. It might occur that the boundary $\partial\Omega_{micro}$ intersects only one face of the cell K , such that this criteria based on the sign does not work. If this kind of cell occurs in the mesh, a local refinement of this cell is used in order to prevent this case.

The next step is to define the finite dimensional spaces U_h and V_h on this mesh. The domain Ω_{micro} is not yet described fully, by distinguishing different kinds of cells. The actual representation of the domain is included in the definition of U_h and V_h . Cells that are not contained in Ω_{micro} will be ignored. Cells that are completely contained are treated in the same way, as in the case of standard FEM. In this case a polynomial ansatz on the unit cell is defined and this function is transformed to the cell K . The interesting part, which also describes the boundary of Ω_{micro} are the cells only partially contained in Ω_{micro} . To define the functions in U_h and V_h in these cells, a polynomial ansatz on the unit cell \hat{K} is chosen again. Like in the standard case this ansatz is transformed to the real cell and then with the help of the level-set function, restricted to the domain $K \cap \Omega_{micro}$.

Due to this construction, all functions in the finite dimensional space are restricted to the domain Ω_{micro} . The finite dimensional spaces U_h and V_h are thus defined as

$$U_h = \{v \in C(\Omega) : v|_K \circ T_K \in Q_1 \text{ if } K \cap \partial\Omega = \emptyset, \quad (3.21)$$

$$v|_{K \cap \Omega} = \psi|_\Omega, \psi \circ T_K \in Q_1 \text{ if } K \cap \partial\Omega \neq \emptyset, \quad (3.22)$$

$$v = g_D \text{ on } \Gamma_D\}, \quad (3.23)$$

$$V_h = \{v \in C(\Omega) : v|_K \circ T_K \in Q_1 \text{ if } K \cap \partial\Omega = \emptyset, \quad (3.24)$$

$$v|_{K \cap \Omega} = \psi|_\Omega, \psi \circ T_K \in Q_1 \text{ if } K \cap \partial\Omega \neq \emptyset, \quad (3.25)$$

$$v = 0 \text{ on } \Gamma_D\}. \quad (3.26)$$

The cells completely contained in Ω_{micro} will be called full cells in the following, while the cells contained partially will be called cut cells, since they are cut by the boundary $\partial\Omega_{micro}$.

3.2.3 Quadrature formula

In this subsection the actual implementation of the CutCell method is shown, especially how the restriction to the domain Ω_{micro} is done. As described before,

a standard Lagrangian basis for the discrete spaces U_h and V_h is chosen. The basis functions are then defined on all full and cut cells. Since all basis functions need to be integrated on every single cell K , the integration is chosen in such a way that it is only done on the domain Ω_{micro} and thus the restriction of the functions to this domain is reached. There are several ways of adjusting the quadrature formula, one approach is to subdivide the cell K into hexahedra such that edges of these hexahedra align with $\partial\Omega_{micro}$. Integration will then be done on the hexahedra contained in the domain Ω_{micro} .

Remark 3.2.2. *It could be argued that with the help of these hexahedra, a mesh representing the domain Ω_{micro} could be defined and thus standard finite elements could be used. But in fact, with this approach the integration hexahedra could be very distorted such that the shape regularity and size regularity of the mesh might not be fulfilled anymore, resulting in numerical problems for standard FEM. For the CutCell method these hexahedra are only used for integration, therefore the mesh regularity does not influence the solution process and therefore numerical problems due to the mesh regularity are prevented.*

Another approach to do the integration only on a part of a cell is the so called moment fitting method, [42].

In the moment fitting method, the idea is to create quadrature formulas in a hierarchical way. The integration on a cut cell in 3D is created for a polynomial space up to a certain degree with the help of a quadrature formula on the boundaries of the same cell. Since some boundaries of the cell will also be cut, the integration there is done with a 2D quadrature formula on a cut face. This quadrature formula is then again reduced to an integration on the edges of the cut face, where cut edges are integrated with a 1D quadrature formula. This method of integrating a cut cell also automatically creates a quadrature formula for integrating on the boundary of the domain $\partial\Omega_{micro}$. Due to this hierarchical structure the implementation of this method is not easy and was therefore not further considered in this thesis.

The approach used in this theses is the subdivision of the cell into hexahedra aligning the domain Ω_{micro} . Let's consider a cut cell K . In the implementation of deal.II quadrature formulas are defined on the unit cell and integration on the real cell is done by a transformation of the integral. The goal is now to define a quadrature rule on the unit cell, such that the transformed integral to this quadrature rule integrates only on the domain Ω_{micro} . In order to do so, the level-set function is first transformed to the unit cell. The unit cell is then subdivided into two parts by the zero isocontour $\hat{\Gamma}_K$ of the transformed level-set function. The part of the unit cell corresponding to the domain Ω_{micro} is then further subdivided into hexahedra \hat{S}_i . The integration on these hexahedra is

then done by transforming the standard integration on a unit cell \hat{K} for every hexahedron. This approach is depicted in figure 3.2 for a two-dimensional case.

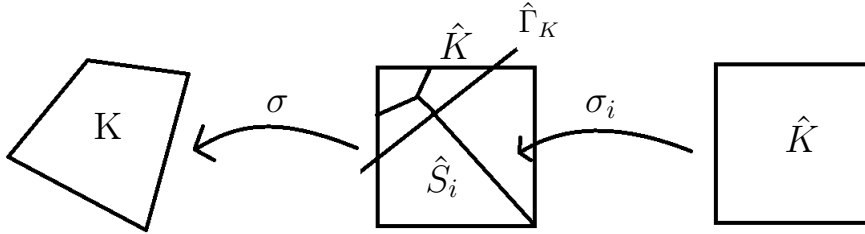


Figure 3.2: Transformations to create the quadrature formula.

The two crucial steps in this approach are the definition of the subdivision into hexahedra and the definition of the transformation between the unit cell and the hexahedron of the subdivision. It is not trivial to fulfill these two steps in such a way that the integration is restricted to Ω_{micro} for a general zero isocontour of the transformed level-set function. Therefore, the isocontour is approximated by a piecewise trilinear function. This approximation does not influence the approximation quality of the CutCell method, since it will be shown later that this linearization error behaves in the same power of h as the discretization error. Since this approximation is used, the transformation between the unit cell and the hexahedra is given by a trilinear mapping. To calculate the subdivision of the unit cell into hexahedra, a trilinear approximation of the level-set function is considered. The subdivision of the unit cell will then be calculated with respect to the isocontour of the trilinear approximation. This seemingly simple case can already create very complicated subdivisions. Neglecting rotation and symmetry, there are 17 different cases, how this isocontour can intersect with the unit cell in three dimensions. The most complicated subdivision is depicted in figure 3.3, where the union of the colored subcells describes the part of the unit cell corresponding to the domain Ω_h .

The subdivision is here based on the intersection points between the isocontour and the edges of the unit cell. Since these intersection points in general are not on a plane, the intersection points are moved along the edges to match the isocontour. If this is not possible due to a too strong curvature of the isocontour, the whole unit cell is first refined once and then the refined subcells are subdivided further.

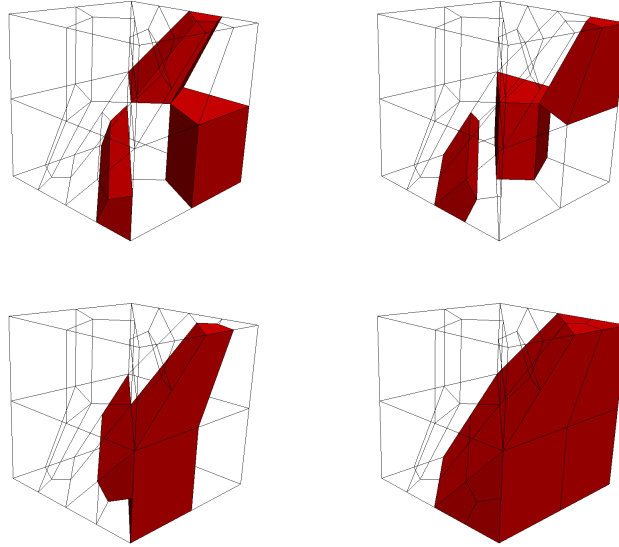


Figure 3.3: Most complicated subdivision for quadrature purposes. For visualization purposes different subcells in the integration domain are highlighted.

3.3 A priori error estimates

3.3.1 Linearization error

As described before the computations are not done on the exact domain Ω_{micro} , but on a domain Ω_h , which has a piecewise trilinear boundary. In order to show that this linearization of the domain does not influence the computation significantly, an error estimate between the exact solution u , solved on Ω_{micro} and the computed solution u_h , solved on Ω_h , is shown. This error estimate will be shown in the exact domain Ω_{micro} and thus includes the linearization error, besides other error contributions. Therefore, this estimate is also an upper bound for the linearization error.

As the solutions u and u_h are defined in different domains Ω_{micro} and Ω_h , extension operators need to be defined for both functions. For these definitions, an additional domain

$$\tilde{\Omega} := \bigcup_{\substack{K \in \mathcal{T}_h, K \subset \Omega_{micro} \\ \text{or} \\ K \cap \partial\Omega_{micro} \neq \emptyset}} K$$

is introduced. Due to this definition, $\Omega_{micro}, \Omega_h \subset \tilde{\Omega}$ is evident. Now the contin-

uous extension operators

$$\begin{aligned} E &: H^2(\Omega_{micro}) \rightarrow H^2(\tilde{\Omega}), \\ E_h &: H^1(\Omega_h) \rightarrow H^1(\Omega_{micro}) \end{aligned}$$

can be defined. The existence of such continuous extensions is proven for example in [53].

Definition 3.3.1. *The differences between the domains Ω_{micro} and Ω_h are defined by the stripes*

$$S := \Omega_{micro} \setminus \Omega_h \tag{3.27}$$

$$S_h := \Omega_h \setminus \Omega_{micro}. \tag{3.28}$$

For the proof of the linearization error, the following two lemmas will be used:

Lemma 3.3.2. *For a function $\varphi \in H^1(\Omega_{micro})$ and the extension operator E defined above, the estimate*

$$\|E\varphi\|_{SUS_h} \leq ch\|\varphi\|_{H^1(\Omega_{micro})}$$

holds true.

Proof. First lemma 2 of the paper of Bramble and King, [9], is used, which produces the inequality

$$\|E\varphi\|_{SUS_h}^2 \leq c(h^2\|\varphi\|_{\partial\Omega_{micro}}^2 + h^4\|\varphi\|_{H^1(\Omega_{micro})}^2).$$

Using trace inequality for the first term concludes the proof. \square

Lemma 3.3.3. *For functions in the space \tilde{U}_h modulo constant functions both mappings $\|\nabla \cdot\|_{\Omega_{micro}}$ and $\|\nabla \cdot\|_{\Omega_h}$ are norms. The space \tilde{U}_h is the space of piecewise trilinear functions on the mesh \mathcal{T}_h , restricted to the domain $\Omega_{micro} \cup \Omega_h$. Therefore, equivalence of norms can be used, since \tilde{U}_h is finite dimensional.*

Proof. The fact that both mappings are norms is indeed not trivial, since they integrate only in a part of the definition space of functions in \tilde{U}_h . It is evident that the only problem is the positive definiteness of these objects, since it might be possible that a function in \tilde{U}_h is constant in Ω_h , but not constant in Ω_{micro} , which means it is non constant only in S , or vice versa. In this case these two objects would not be norms and therefore norm equivalence could not be used. But this is a case that cannot occur.

The difference between Ω_h and Ω_{micro} is the linearization of the boundary. Since the CutCell method is used, every cell that contains the stripe S also contains a subset of $\Omega_{micro} \cap \Omega_h$. If this would not be fulfilled, the boundary $\partial\Omega_{micro}$ would intersect only one face of the cell K and the cell K would have been refined locally. In this cell the function is defined by the same basis functions, just restricted onto different domains. Therefore, if a function is non constant in the stripe S , it would also be non constant in $\Omega_{micro} \cap \Omega_h$. This shows that the above mappings are both norms and therefore norm equivalence can be used here. \square

With these extension operators and lemmas, the discretization error, which includes the linearization error, can be derived.

Theorem 3.3.4 (Discretization error). *Let $u \in H^2(\Omega_{micro})$ and $u_h \in U_h$ be the solutions of problems 3.1.2 and 3.2.1, then the error estimate*

$$\|\nabla(u - E_h u_h)\|_{\Omega_{micro}} \leq ch \|u\|_{H^2(\Omega_{micro})}$$

holds true.

Proof. First triangle inequality is used:

$$\|\nabla(u - E_h u_h)\|_{\Omega_{micro}} \leq \|\nabla(u - I_h E u)\|_{\Omega_{micro}} + \|\nabla(I_h E u - E_h u_h)\|_{\Omega_{micro}}, \quad (3.29)$$

where I_h describes the standard nodal interpolation operator on $\tilde{\Omega}$. The domain $\tilde{\Omega}$ is used instead of Ω_{micro} here, since otherwise the standard nodal interpolation operator could not be used. For the standard nodal interpolation operator, the function u needs to be evaluated at specific points, which might not be contained in Ω_{micro} . But these points will definitely be contained in $\tilde{\Omega}$. The first term in the above estimate can be further estimated in a standard way using the fact that the extension operator is continuous:

$$\begin{aligned} \|\nabla(u - I_h E u)\|_{\Omega_{micro}} &\leq \|\nabla(E u - I_h E u)\|_{\tilde{\Omega}} \\ &\leq ch \|E u\|_{H^2(\tilde{\Omega})} \\ &\leq ch \|u\|_{H^2(\Omega_{micro})}. \end{aligned}$$

Thus the second term of the above estimate is now considered.

To estimate this term, some kind of perturbed Galerkin orthogonality will be used. Therefore, equation (3.1.2) is tested with the extension of a test function $\varphi_h \in U_h$ to the domain Ω_{micro} . As this extension is still in $H^1(\Omega_{micro})$, equation (3.1.2) is still true.

Taking the difference of this equation with equation (3.2.1), the identity

$$0 = (\nabla u, \nabla E_h \varphi_h)_{\Omega_{micro}} - (\nabla u_h, \nabla \varphi_h)_{\Omega_h} \quad (3.30)$$

$$= (\nabla u, \nabla \varphi_h)_{\Omega_{micro} \cap \Omega_h} + (\nabla u, \nabla E_h \varphi_h)_S - (\nabla u_h, \nabla \varphi_h)_{\Omega_h} \quad (3.31)$$

$$= (\nabla E u, \nabla \varphi_h)_{\Omega_h} - (\nabla E u, \nabla \varphi)_{S_h} + (\nabla u, \nabla E_h \varphi_h)_S - (\nabla u_h, \nabla \varphi_h)_{\Omega_h} \quad (3.32)$$

$$= (\nabla (E u - u_h), \nabla \varphi_h)_{\Omega_h} - (\nabla E u, \nabla \varphi_h)_{S_h} + (\nabla u, \nabla E_h \varphi_h)_S \quad (3.33)$$

is shown.

Now the estimation of the error in the energy norm can be continued. Using the extension operator, the second term of (3.29) can be estimated by starting with lemma 3.3.3

$$\|\nabla(I_h E u - E_h u_h)\|_{\Omega_{micro}} \leq c \|\nabla(I_h E u - u_h)\|_{\Omega_h} \quad (3.34)$$

$$\leq c \sup_{\varphi \in U_h} \frac{(\nabla(I_h E u - u_h), \nabla \varphi_h)_{\Omega_h}}{\|\nabla \varphi_h\|_{\Omega_h}} \quad (3.35)$$

$$= c \sup_{\varphi_h \in U_h} \frac{(\nabla(I_h E u - E u), \nabla \varphi_h)_{\Omega_h} - (\nabla(E u - u_h), \nabla \varphi_h)_{\Omega_h}}{\|\nabla \varphi_h\|_{\Omega_h}} \quad (3.36)$$

$$\stackrel{(3.30)}{=} c \sup_{\varphi_h \in U_h} \left[\frac{(\nabla(I_h E u - E u), \nabla \varphi_h)_{\Omega_h}}{\|\nabla \varphi_h\|_{\Omega_h}} \right. \quad (3.37)$$

$$\left. - \frac{(\nabla E u, \nabla \varphi_h)_{S_h} - (\nabla u, \nabla E_h \varphi_h)_S}{\|\nabla \varphi_h\|_{\Omega_h}} \right] \quad (3.38)$$

$$\leq c(\|\nabla(I_h E u - E u)\|_{\Omega_h} + \|\nabla E u\|_{S_h} + \|\nabla u\|_S). \quad (3.39)$$

The first term can be estimated in a standard way as above. The second term can be estimated by using lemma 3.3.2

$$\|\nabla E u\|_{S_h} + \|\nabla u\|_S \leq ch \|u\|_{H^2(\Omega_{micro})}.$$

In summary the following estimation is shown.

$$\|\nabla(u - u_h)\|_{\Omega_{micro}} \leq ch \|u\|_{H^2(\Omega_{micro})},$$

which includes an upper bound for the linearization error. \square

3.4 Condition number of CutCells

In the following the behavior of the condition number of the stiffness matrix, when $\partial\Omega_{micro}$ approaches the boundary of cells, is proven. The idea of the proof is to first show the condition number of a cell-wise mass matrix. From there the

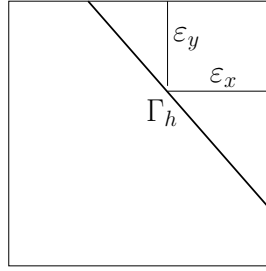


Figure 3.4: Sketch of an axis parallel cuboid included in the integration domain.

conditioning of the global mass matrix is derived and with the help of an inverse estimate the conditioning of the stiffness matrix is established.

To derive the condition number of the mass matrix M , a standard approach is used to estimate the largest and smallest eigenvalues by the largest and smallest eigenvalue of a cell-wise mass matrix M_K .

$$\lambda_{\min}(M) \geq c \min_{K \in \mathbb{T}_h} \lambda_{\min}(M_K)$$

$$\lambda_{\max}(M) \leq c \max_{K \in \mathbb{T}_h} \lambda_{\max}(M_K).$$

If there is at least one cell K , which is not cut, it is well known that $\lambda_{\max}(M_K) = \mathcal{O}(h^d)$ holds true. By a transformation of the integration on a cut cell, it can be easily shown that the largest eigenvalue of this cell-wise mass matrix is smaller than the largest eigenvalue of the local matrix of an uncut cell.

For the smallest eigenvalue of the cell-wise mass matrix, the following theorem will be shown. For the proof of this theorem, the largest cuboid is considered, which can be contained in the part of the unit cell \hat{K} that belongs to the integration domain and is parallel to the cell boundaries, as depicted in figure 3.4. The edge lengths of this cuboid are defined as ε_x , ε_y and ε_z .

Theorem 3.4.1. *For the smallest eigenvalue of the local mass matrix the estimate*

$$\lambda_{\min}(M_K) \geq ch^d(\varepsilon_x\varepsilon_y\varepsilon_z)^3$$

holds true.

Proof. The first step of the proof is to transform the integrals of the local mass matrix to integrals on the unit cell \hat{K} . This transformation also directly provides the claimed h -dependency, thus this dependency won't be mentioned anymore. In cells not included in the domain Ω_{micro} completely, integration is only done on a part of the cell \hat{K} .

In the following, the notation \hat{M}_ε is used for the local mass matrix in the domain $K \cap \Omega_{micro}$, M_r for the mass matrix integrated only in the cuboid. For the smallest eigenvalue of \hat{M}_ε the following holds true:

$$\lambda_{min}(\hat{M}_\varepsilon) = \min_{x \in \mathbb{R}^d} \frac{(x, \hat{M}_\varepsilon x)}{\|x\|_2} \geq \min_{x \in \mathbb{R}^d} \frac{(x, M_r x)}{\|x\|_2} = \lambda_{min}(M_r).$$

The inequalities hold true as the difference between the mass matrices is described by a symmetric positive definite mass matrix integrating the domain difference.

To determine the eigenvalues of the matrix M_r , this matrix is written in terms of the full local mass matrix. This is possible, because for the cuboid the integration can be done separately in every direction, i.e. it suffices to look at the one-dimensional case.

In the 1D case the mass matrix is a 2x2 matrix, with entries:

$$\hat{M}_{ij} = \int_{\hat{K}} \varphi_i \varphi_j dx,$$

where the basis functions are given by: $\varphi_1(x) = (1 - x)$ and $\varphi_2(x) = x$. The entries of the matrix are compared for the cases of the full unit cell $\hat{K} = (0, 1)$ and for a cut unit cell $\hat{K} = (0, \varepsilon)$.

$$\begin{aligned} \int_0^\varepsilon x^2 dx &= \int_0^1 \varepsilon^2 \hat{x}^2 \varepsilon d\hat{x} \\ &= \varepsilon^3 \int_0^1 \hat{x}^2 d\hat{x}, \\ \int_0^\varepsilon (1-x)x dx &= \int_0^1 \varepsilon \hat{x} (1 - \varepsilon \hat{x}) \varepsilon d\hat{x} \\ &= \varepsilon^2 \int_0^1 \hat{x} (1 - \hat{x} + \hat{x} - \varepsilon \hat{x}) d\hat{x} \\ &= \varepsilon^2 \int_0^1 \hat{x} (1 - \hat{x}) d\hat{x} + \varepsilon^2 (1 - \varepsilon) \int_0^1 \hat{x}^2 d\hat{x}, \\ \int_0^\varepsilon (1-x)^2 dx &= \varepsilon \int_0^1 (1 - \varepsilon \hat{x})^2 d\hat{x} \\ &= \varepsilon \int_0^1 (1 - \hat{x} + \hat{x} - \varepsilon \hat{x})^2 d\hat{x} \\ &= \varepsilon \int_0^1 (1 - \hat{x})^2 + 2\varepsilon \int_0^1 (1 - \hat{x}) \hat{x} (1 - \varepsilon) d\hat{x} + \varepsilon \int_0^1 \hat{x}^2 (1 - \varepsilon)^2 d\hat{x}. \end{aligned}$$

Using the notation

$$\mathcal{E} = \begin{pmatrix} 1 & (1 - \varepsilon) \\ 0 & \varepsilon \end{pmatrix}$$

the matrix \hat{M}_r is written in terms of the matrix \hat{M} :

$$\varepsilon \mathcal{E} \hat{M} \mathcal{E}^T = \hat{M}_r.$$

Now the smallest eigenvalue of M_r can be estimated with the help of the singular values of \mathcal{E} :

$$\lambda_{\min}(M_s)^{-1} \leq \varepsilon^{-1} \sigma_{\min}(\mathcal{E})^{-2} \lambda_{\min}(M_s)^{-1} = \mathcal{O}(\varepsilon^{-3}).$$

The behavior of the singular values can be shown by explicitly computing them. This concludes the proof. \square

3.4.1 Stiffness matrix

Theorem 3.4.2. *For the condition number κ of the stiffness matrix, the estimate*

$$\kappa(A) \leq c \varepsilon_x^{-2} \varepsilon_y^{-3} \varepsilon_z^{-3} h^{-2}$$

holds true.

Proof. To proof this estimate, first the largest eigenvalue of the stiffness matrix and in the second step the smallest eigenvalue is considered, where the hard part of the proof is again the estimation of the smallest eigenvalue.

One standard way to proof the behavior of the largest eigenvalue, is to use an inverse estimate. To use the same approach for CutCells, the full cells and the cut cells are considered separately. The solution in the cut cells is extended to the whole cell, before applying the inverse estimate.

$$\begin{aligned} a(\varphi_h, \varphi_h) &\leq \sum_{K \in \mathcal{T}_h, K \subset \Omega_{\text{micro}}} \|\nabla \varphi_h\|_{L^2(K)} + \sum_{K \in \mathcal{T}_h, K \setminus \Omega_{\text{micro}} \neq \emptyset} \|\nabla \varphi_h\|_{L^2(K_\varepsilon)} \\ &\leq \sum_{K \in \mathcal{T}_h, K \subset \Omega_{\text{micro}}} \|\nabla \varphi_h\|_{L^2(K)} + \sum_{K \in \mathcal{T}_h, K \setminus \Omega_{\text{micro}} \neq \emptyset} \|\nabla \varphi_h\|_{L^2(K)} \\ &\leq \max_{K \in \mathcal{T}_h} h_K^{-2} \sum_{K \in \mathcal{T}_h, K \subset \Omega_{\text{micro}}} \|\varphi_h\|_{L^2(K)} + \sum_{K \in \mathcal{T}_h, K \setminus \Omega_{\text{micro}} \neq \emptyset} \|\varphi_h\|_{L^2(K)} \\ &\leq c \max_{K \in \mathcal{T}_h} h_K^{-2+d} \sum_{K \in \mathcal{T}_h, K \subset \Omega_{\text{micro}}} \|\varphi_h\|_{L^\infty(K)} + \sum_{K \in \mathcal{T}_h, K \setminus \Omega_{\text{micro}} \neq \emptyset} \|\varphi_h\|_{L^\infty(K)} \\ &\leq c \max_{K \in \mathcal{T}_h} h_K^{-2+d} \sum_{K \in \mathcal{T}_h, K \subset \Omega_{\text{micro}}} |x_K| + \sum_{K \in \mathcal{T}_h, K \setminus \Omega_{\text{micro}} \neq \emptyset} |x_K| \\ &\leq c \max_{K \in \mathcal{T}_h} h_K^{-2+d} |x|. \end{aligned}$$

In the above equations the notation $K_\varepsilon = K \cap \Omega_{\text{micro}}$ was used.

For the smallest eigenvalue, an arbitrary vector $x \in \mathbb{R}^n$ with $n = \dim(V_h)$ is considered, defining an arbitrary function $\varphi_h \in V_h$ by linear combination with a given basis. This vector is separated into cut cells and full cells

$$|x|^2 \leq \sum_{K \in \mathbb{T}_h, K \subset \Omega_{micro}} |x_K|^2 + \sum_{K \in \mathbb{T}_h, K \setminus \Omega_{micro} \neq \emptyset} |x_K|^2.$$

First the local vector x_k corresponding to cut cells is considered. In the proof of theorem 3.4.1 the following inequality was already proven.

$$|x_K|^2 \leq ch^{-d} \varepsilon_x^{-3} \varepsilon_y^{-3} \varepsilon_z^{-3} \|\varphi_h\|_{L^2(K_\varepsilon)}^2. \quad (3.40)$$

For the next steps, the linearised boundary Γ_h in the cell K is considered. For an arbitrary $x \in \Gamma_h$, the following equation holds true.

$$\varphi_h(x + tn_{\Gamma_h}(x)) = \varphi_h(x) + \int_0^t \partial_r \varphi_h(x + rn_{\Gamma_h}(x)) dr,$$

where n_{Γ_h} describes the normal on Γ_h and $t \in (0, \delta(x))$. $\delta(x)$ describes the distance between the point $x \in \Gamma_h$ and the boundary of the cell K in direction of n_{Γ_h} . It is evident to show that for the maximal distance $\varepsilon h := \max_{x \in \Gamma_h} \delta(x)$ the inequality

$$\varepsilon \leq c \min\{\varepsilon_x, \varepsilon_y, \varepsilon_z\} \quad (3.41)$$

holds true.

Taking absolute values and the square of equation (3.40), Young's, Hölder's and triangle inequality provide:

$$|\varphi_h(x + tn_{\Gamma_h}(x))|^2 \leq 2|\varphi_h(x)|^2 + 2c\varepsilon h \int_0^{\delta(x)} |\partial_r \varphi_h(x + rn_{\Gamma_h}(x))|^2 dr.$$

The next step is to integrate this inequality over $t \in (0, \delta(x))$ and $x \in \Gamma_h$:

$$\|\varphi_h\|_{L^2(K_\varepsilon)}^2 \leq 2c\varepsilon h \int_{\Gamma_h} |\varphi_h(x)|^2 dx + 2c\varepsilon^2 h^2 \|\nabla \varphi_h\|_{L^2(K_\varepsilon)}^2.$$

By summation over all cut cells and using the trace inequality and a Poincaré inequality to estimate the middle term, it follows:

$$\begin{aligned} \sum_{k \in \mathbb{T}_h, K \setminus \Omega_{micro} \neq \emptyset} \|\varphi_h\|_{L^2(K_\varepsilon)}^2 &\leq c\varepsilon h \|\varphi_h(x)\|_{H^1(\Omega_{micro})}^2 + 2\varepsilon^2 h^2 \|\nabla \varphi_h\|_{L^2(\Omega_{micro})}^2 \\ &\leq c\varepsilon h \|\nabla \varphi_h(x)\|_{L^2(\Omega_{micro})}^2. \end{aligned}$$

The estimate for the degrees of freedom corresponding to full cells uses a transformation to the unit cell \hat{K} and equivalency of the L^∞ and L^2 norms. With the help of a Poincaré estimate the following inequality is produced:

$$\begin{aligned} \sum_{K \in \mathcal{T}_h, K \subset \Omega_{micro}} |x_K| &\leq ch^{-d} \|\varphi_h\|_{L^2(\Omega_{micro})} \\ &\leq ch^{-d} \|\nabla \varphi\|_{L^2(\Omega_{micro})}. \end{aligned}$$

Assuming without loss of generality that the minimum in equation (3.41) is given by ε_x , the overall estimate therefore has the following form

$$\begin{aligned} |x|^2 &\leq ch^{-d} \left(\|\nabla \varphi\|_{L^2(\Omega_{micro})} + \varepsilon_x^{-3} \varepsilon_y^{-3} \varepsilon_z^{-3} \sum_{K \in \mathbb{T}_h, K \setminus \Omega_{micro} \neq \emptyset} \|\varphi_h\|_{L^2(K_\varepsilon)}^2 \right) \\ &\leq ch^{-d} \left(1 + h\varepsilon_x^{-2} \varepsilon_y^{-3} \varepsilon_z^{-3} \right) \|\nabla \varphi\|_{L^2(\Omega_{micro})} \\ &\leq ch^{-d} \left(1 + h\varepsilon_x^{-2} \varepsilon_y^{-3} \varepsilon_z^{-3} \right) a(\varphi_h, \varphi_h), \end{aligned}$$

which concludes the proof of theorem 3.4.2. □

Remark 3.4.3. *The numerical examples suggest that the above estimate for the stiffness matrix is not sharp. In a comparison between mass matrix and the stiffness matrix, a reduction in the powers of ε can be observed. In the theoretical result, the power is only reduced by 1, while in the numerical examples the power is reduced by 2.*

In the numerical examples, three different cases are considered:

- $\varepsilon_x \rightarrow 0$, $\varepsilon_y, \varepsilon_z$ constant,
- $\varepsilon_x, \varepsilon_y \rightarrow 0$, ε_z constant,
- $\varepsilon_x, \varepsilon_y, \varepsilon_z \rightarrow 0$.

In the cases 2 and 3 the different ε_i , $i = x, y, z$ tend to zero in the same manner, therefore the different directions can be replaced by a single ε .

For the numerical examples, a domain $\Omega = (-50, 50)^2 \times (-10, 10)$ is considered. Ω_{micro} is defined by the domain with positive value for the level-set function

$$\phi(x) = \begin{cases} x + \varepsilon & \text{in case 1,} \\ x + y + \varepsilon & \text{in case 2,} \\ x + y + z + \varepsilon & \text{in case 3.} \end{cases}$$

To create the mesh \mathcal{T}_h , the domain Ω is globally refined 3 times.

ε	$\lambda_{max}(M)$	$\lambda_{min}(M)$	$\kappa(M)$	$\lambda_{max}(A)$	$\lambda_{min}(A)$	$\kappa(A)$
2^{-2}	1.42e-03	-2.90	-2.90	1.37e-03	-1.42	-1.42
2^{-3}	6.78e-04	-2.94	-2.94	6.56e-04	-1.14	-1.14
2^{-4}	3.31e-04	-2.97	-2.97	3.20e-04	-1.04	-1.04
2^{-5}	1.64e-04	-2.98	-2.98	1.58e-04	-1.01	-1.01
2^{-6}	8.13e-05	-2.99	-2.99	7.85e-05	-1.00	-1.00

Table 3.1: Numerical convergence rates for test case 1.

ε	$\lambda_{max}(M)$	$\lambda_{min}(M)$	$\kappa(M)$	$\lambda_{max}(A)$	$\lambda_{min}(A)$	$\kappa(A)$
2^{-2}	1.21e-03	-5.99	-5.98	1.19e-03	-4.06	-4.06
2^{-3}	6.10e-04	-6.00	-6.00	6.01e-04	-4.01	-4.01
2^{-4}	3.06e-04	-6.00	-6.00	3.02e-04	-4.00	-4.00
2^{-5}	1.53e-04	-6.00	-6.00	1.51e-04	-4.00	-4.00
2^{-6}	7.68e-05	-6.00	-6.00	7.57e-05	-4.00	-4.00

Table 3.2: Numerical convergence rates for test case 2.

On this mesh, problem 3.2.1 is used to create the stiffness matrix and the corresponding problem to create the mass matrix. To calculate the largest and smallest eigenvalue, the method of power iteration is used.

Tables 3.1, 3.2 and 3.3 show the numerical convergence rates for the largest and smallest eigenvalue and the condition number of the mass matrix and the stiffness matrix.

The results for the mass matrix M shows the expected behavior in terms of ε , while the results of the stiffness matrix A suggest that the estimates shown above are not sharp.

Table 3.4 shows the proven and the numerical results for these three different cases. The smallest eigenvalues of the stiffness matrix A show a smaller convergence rate in term of ε than it was theoretically proven.

ε	$\lambda_{max}(M)$	$\lambda_{min}(M)$	$\kappa(M)$	$\lambda_{max}(A)$	$\lambda_{min}(A)$	$\kappa(A)$
2^{-2}	1.22e-03	-9.00	-9.00	1.21e-03	-6.99	-6.99
2^{-3}	6.14e-04	-9.00	-9.00	6.10e-04	-7.00	-7.00
2^{-4}	3.08e-04	-9.00	-9.00	3.06e-04	-7.00	-7.00
2^{-5}	1.55e-04	-9.00	-9.00	1.54e-04	-7.00	-7.00
2^{-6}	7.74e-05	-9.00	-9.00	7.70e-05	-7.00	-7.00

Table 3.3: Numerical convergence rates for test case 3.

case	$\lambda_{max}(M)$	$\lambda_{min}(M)$	$\kappa(M)$	$\lambda_{max}(A)$	$\lambda_{min}(A)$	$\kappa(A)$
1	$\varepsilon^0(\varepsilon^0)$	$\varepsilon^{-3}(\varepsilon^{-3})$	$\varepsilon^{-3}(\varepsilon^{-3})$	$\varepsilon^0(\varepsilon^0)$	$\varepsilon^{-1}(\varepsilon^{-2})$	$\varepsilon^{-1}(\varepsilon^{-2})$
2	$\varepsilon^0(\varepsilon^0)$	$\varepsilon^{-6}(\varepsilon^{-6})$	$\varepsilon^{-6}(\varepsilon^{-6})$	$\varepsilon^0(\varepsilon^0)$	$\varepsilon^{-4}(\varepsilon^{-5})$	$\varepsilon^{-4}(\varepsilon^{-5})$
3	$\varepsilon^0(\varepsilon^0)$	$\varepsilon^{-9}(\varepsilon^{-9})$	$\varepsilon^{-9}(\varepsilon^{-9})$	$\varepsilon^0(\varepsilon^0)$	$\varepsilon^{-7}(\varepsilon^{-8})$	$\varepsilon^{-7}(\varepsilon^{-8})$

Table 3.4: Numerical (and theoretical) results for the convergence of the eigenvalues and the condition number for the mass matrix and stiffness matrix for the CutCell method.

ε	$\lambda_{max}(M)$	$\lambda_{min}(M)$	$\kappa(M)$	$\lambda_{max}(A)$	$\lambda_{min}(A)$	$\kappa(A)$
2^{-2}	1.91e-02	6.18e-02	8.09e-02	-2.72e-03	-3.72e-03	-6.44e-03
2^{-3}	8.96e-03	2.78e-02	3.68e-02	-2.33e-03	-1.93e-03	-4.26e-03
2^{-4}	4.09e-03	1.25e-02	1.66e-02	-1.42e-03	-9.19e-04	-2.34e-03
2^{-5}	1.93e-03	5.83e-03	7.76e-03	-7.69e-04	-4.37e-04	-1.20e-03
2^{-6}	9.34e-04	2.81e-03	3.74e-03	-3.99e-04	-2.11e-04	-6.10e-04

Table 3.5: Numerical convergence rates for test case 1 with diagonal preconditioning.

3.4.2 Preconditioning

In this section it will be shown numerically, that a simple preconditioner can get rid of the ε dependency of the condition of the stiffness matrix. One of the simplest preconditioner is a diagonal scaling of the rows and columns of the matrix A . In order to do that the diagonal matrix D is defined

$$D = \text{diag}(A)$$

with the diagonal entries of A . Note that due to the positive definiteness of the matrix, all entries of D are positive. Therefore, the matrix $D^{-0.5}$ can be defined by taking the square root and the inverse of the entries of D . With the help of this diagonal matrix the preconditioned system can be defined.

$$\begin{aligned} D^{-\frac{1}{2}}AD^{-\frac{1}{2}}y &= D^{-\frac{1}{2}}b, \\ x &= D^{-\frac{1}{2}}y, \end{aligned}$$

which is obviously equivalent to $Ax = b$. In tables 3.5, 3.6 and 3.7 the convergence rates of the condition number of the stiffness and the mass matrix are shown as before.

From the tables it is evident that this simple preconditioning is enough to make the condition number of the stiffness matrix independent of the distance between the boundary of Ω_{micro} and the boundary of the cells K .

ε	$\lambda_{max}(M)$	$\lambda_{min}(M)$	$\kappa(M)$	$\lambda_{max}(A)$	$\lambda_{min}(A)$	$\kappa(A)$
2^{-2}	-4.10e-03	1.47e-02	1.06e-02	-1.34e-03	1.73e-04	-1.17e-03
2^{-3}	-2.59e-03	3.07e-03	4.85e-04	-8.14e-04	-4.93e-04	-1.31e-03
2^{-4}	-1.46e-03	8.77e-05	-1.37e-03	-4.59e-04	-4.27e-04	-8.86e-04
2^{-5}	-7.79e-04	-3.83e-04	-1.16e-03	-2.46e-04	-2.65e-04	-5.10e-04
2^{-6}	-4.03e-04	-3.08e-04	-7.11e-04	-1.27e-04	-1.46e-04	-2.73e-04

Table 3.6: Numerical convergence rates for test case 2 with diagonal preconditioning.

ε	$\lambda_{max}(M)$	$\lambda_{min}(M)$	$\kappa(M)$	$\lambda_{max}(A)$	$\lambda_{min}(A)$	$\kappa(A)$
2^{-2}	-2.75e-03	-2.20e-03	-4.95e-03	-2.14e-04	2.90e-03	2.69e-03
2^{-3}	-1.35e-03	-1.49e-03	-2.84e-03	-8.07e-05	8.68e-04	7.87e-04
2^{-4}	-6.66e-04	-8.51e-04	-1.52e-03	-3.33e-05	2.89e-04	2.55e-04
2^{-5}	-3.30e-04	-4.49e-04	-7.79e-04	-1.49e-05	1.08e-04	9.36e-05
2^{-6}	-1.64e-04	-2.29e-04	-3.94e-04	-6.96e-06	4.53e-05	3.84e-05

Table 3.7: Numerical convergence rates for test case 3 with diagonal preconditioning.

Remark 3.4.4. *It should be mentioned that this result holds true only for the case of trilinear finite elements. In the case of triquadratic finite element this simple preconditioning improves the condition number, but does not make it independent of ε .*

3.5 Error estimation and adaptivity

The computational costs of the CutCell method, like for every other method, highly depends on the mesh, to be more precise on the number of cells in the mesh. The approximation quality also highly depends on the number of cells in the mesh. Therefore, it is crucial to keep as few cells as possible, while still maintaining a specific approximation quality.

In this section, it will be discussed, how cell-wise error estimators can be derived in order to refine the mesh adaptively to reduce the error of the calculation of the effective parameter, while using as few degrees of freedom as possible. This is done by using the dual weighted residual method (DWR), described in [4].

Before connecting the DWR method with the CutCell method, the idea of the DWR method for linear problems will be discussed briefly.

For a given linear functional $J : U \rightarrow \mathcal{R}$, in which the error is measured, the so called dual problem is defined:

Problem 3.5.1. (*Dual problem*) Find $z \in V$, such that

$$(\nabla\varphi, \nabla z)_\Omega = J(\varphi) \quad \forall \varphi \in V$$

holds true.

In this problem z is called the dual solution.

Now if the solution u of the continuous primal problem 3.1.2, and the solution u_h of the discrete primal problem 3.2.1 were both in the space U , i.e. $U_h \subset U$, the difference could be applied to the dual problem and the error identity

$$\begin{aligned} J(u - u_h) &= (\nabla(u - u_h), \nabla z)_{\Omega_{micro}} \\ &= (f, z) - (\nabla u_h, \nabla z) \end{aligned}$$

could be established.

In fact due to the linearization of the boundary of the domain Ω_{micro} , the discrete problem and the continuous problem are solved on different domains, $\Omega_h \neq \Omega_{micro}$, therefore $U_h \not\subset U$ and the error estimators need to be derived in a different way. As explained in section 3.1 for the calculation of effective parameter the flux of the solution u of problem 3.1.2 on the boundary Γ_d is needed. Therefore, the obvious choice for the goal functional J would be this flux. The problem there is that the flux

$$J(\varphi) = \int_{\Gamma_d} \partial_n \varphi dx$$

is only well defined if the functions φ has at least an $H^2(\Omega_{micro})$ regularity. But the functions in the space V , which is the test space in problem 3.5.1, only have H^1 regularity. Therefore, problem 3.5.1 is not well defined for this goal functional. The Babuška Miller trick, [2], is used to rewrite the flux functional. A function is defined, which is linear in z direction

$$\begin{aligned} \psi : \Omega &\rightarrow \mathcal{R}, \\ \psi &= 1 && \text{on } \Gamma_d, \\ \psi &= 0 && \text{on } \Gamma_u, \end{aligned}$$

and rewrite the goal functional

$$\begin{aligned} J(u) &= \int_{\Gamma_d} \partial_n u dx \\ &= \int_{\Gamma_d} \partial_n u \psi dx \\ &= (\nabla u, \nabla \psi) - \underbrace{(\Delta u, \psi)}_{=0}. \end{aligned}$$

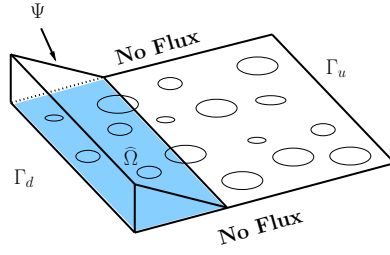


Figure 3.5: 2d scheme of Babuška Miller trick.

The second term vanishes, if u is assumed to be the solution of problem 3.1.1. Now this functional is well defined for all test functions $\varphi \in U$ and therefore this functional can be used as error functional.

For the derivation of the error estimators, the extension operators that were already used in the proof of the linearization error 3.3.4 are used again, without actually stating them. Furthermore, the difference between the domains Ω_{micro} and Ω_h is defined by the stripes S and S_h as defined in definition 3.3.1

Theorem 3.5.2 (Error estimators). *Let u and u_h be the solutions of problem 3.1.2 and 3.2.1 and z the solution of the dual problem 3.5.1, then the error identity*

$$J(u - u_h) = -(\nabla u_h, \nabla z)_{\Omega_h} - (\nabla u_h, \nabla z)_S + (\nabla u_h, \nabla z)_{S_h}$$

holds true.

Proof. Applying $u - u_h$ to the functional J , and using first the dual problem 3.5.1 and then the primal problem 3.1.2, the identity

$$\begin{aligned} J(u - u_h) &= (\nabla(u - u_h), \nabla \psi)_{\Omega_{micro}} \\ &= (\nabla(u - u_h), \nabla z)_{\Omega_{micro}} \\ &= -(\nabla u_h, \nabla z)_{\Omega_{micro}} \\ &= -(\nabla u_h, \nabla z)_{\Omega_h} - (\nabla u_h, \nabla z)_S + (\nabla u_h, \nabla z)_{S_h} \end{aligned}$$

is derived. □

In a similar way, an a priori estimate for the functional J can be proven with the help of the discrete dual problem

Problem 3.5.3. (Discrete dual problem) Find $z_h \in V_h$, such that

$$(\nabla \varphi_h, \nabla z_h)_{\Omega_h} = (\nabla \varphi_h, \nabla \psi)_{\Omega_h} \quad \forall \varphi_h \in V_h$$

holds true.

Theorem 3.5.4 (A priori error estimate). *Let u and u_h be the solutions of problem 3.1.2 and 3.2.1, then the error estimate*

$$J(u - u_h) \leq ch^2 \|u\|_{H^2(\Omega_{micro})} \|z\|_{H^2(\Omega_{micro})}$$

holds true.

Proof. Let z be the solution of the dual problem 3.5.1.

$$\begin{aligned} J(u - u_h) &= (\nabla(u - u_h), \nabla\psi)_{\Omega_{micro}} \\ &= (\nabla(u - u_h), \nabla z)_{\Omega_{micro}}. \end{aligned}$$

The next step is to add and subtract the solution z_h of the discrete dual problem 3.5.3.

$$\begin{aligned} J(u - u_h) &= (\nabla(u - u_h), \nabla(z - z_h))_{\Omega_{micro}} + (\nabla(u - u_h), \nabla z_h)_{\Omega_{micro}} \\ &\leq \|\nabla(u - u_h)\|_{\Omega_{micro}} \|\nabla(z - z_h)\|_{\Omega_{micro}} - (\nabla u_h, \nabla z_h)_{\Omega_{micro}}. \end{aligned}$$

Both factors in the first term can be estimated with the a priori estimate 3.3.4. Therefore, only the second term is considered. The discrete primal problem 3.2.1 is used. It should be mentioned that the integration domain there has to be Ω_h . The remainder terms are therefore given by

$$\begin{aligned} (\nabla u_h, \nabla z_h)_{\Omega_{micro}} &= (\nabla u_h, \nabla z_h)_S - (\nabla u_h, \nabla z_h)_{S_h} \\ &\leq c \|\nabla u_h\|_{S_h \cup S} \|\nabla z_h\|_{S_h \cup S}. \end{aligned}$$

Both terms can be treated in the same way, therefore only the details for one term using again the a priori estimate 3.3.4 and lemma 3.3.2 are given.

$$\begin{aligned} \|\nabla u_h\|_{S_h \cup S} &\leq \|\nabla(u - u_h)\|_{S_h \cup S} + \|\nabla u\|_{S_h \cup S} \\ &\leq ch \|u\|_{H^2(\Omega_{micro})}. \end{aligned}$$

This finishes the proof. □

With the proof of this a priori estimate for J in mind, the error estimators are considered again.

$$J(u - u_h) = \underbrace{-(\nabla u_h, \nabla z)_{\Omega_h}}_{(1)} - \underbrace{(\nabla u_h, \nabla z)_S + (\nabla u_h, \nabla z)_{S_h}}_{(2)}. \quad (3.42)$$

The terms marked with (2) can be estimated in the same way as the corresponding terms in the proof of the a priori estimate, and therefore it can be show that $(2) \leq ch^2 \|u\|_{H^2(\Omega_{micro})} \|z\|_{H^2(\Omega_{micro})}$. But having a look in the proof of lemma

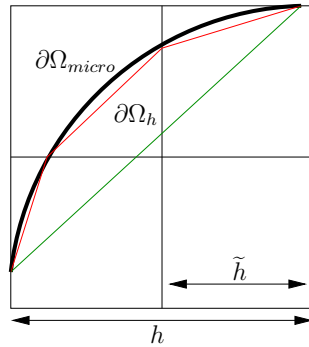


Figure 3.6: Scheme of quadrature refinement for better boundary approximation. The green approximation is done w.r.t. the whole cell, the red approximation for the subcells.

3.3.2, especially at the proof of lemma 2 in [9], one can easily see that one of the h in this estimate corresponds to the area of the stripe $S_h = \Omega_h \setminus \Omega_{micro}$ or $S = \Omega_{micro} \setminus \Omega_h$ cell-wise. Due to the way, the CutCell method was defined, the linearization error can be reduced, and therefore the stripe S , which leads to a \tilde{h} , which is smaller than h . With this notation, it can be shown that the term (2) can be estimated by

$$(2) \leq ch\tilde{h}\|u\|_{H^{\frac{3}{2}}(\Omega_{micro})}\|z\|_{H^2(\Omega_{micro})}.$$

In this way, it can be argued that the term (1) on its own might be a good enough estimator for the error of the functional J .

In cells K cut by the boundary $\partial\Omega_{micro}$, the basis functions are restricted to the domain Ω_{micro} by adjusting the quadrature formula to only integrate in $K \cap \Omega_{micro}$. The adjustment of the quadrature formula leads here to the linearization error. If the cell K was virtually refined globally once or even several times and then a quadrature formula was defined and restricted on every subcell, a piecewise linear approximation of the boundary $\partial\Omega_{micro}$ would be achieved, therefore reducing the area of the stripe S . This virtual refinement is depicted in figure 3.6, in which also the difference between h and \tilde{h} is shown.

Since this refinement is done on a mesh used only to define a suitable quadrature formula, the mesh \mathcal{T}_h and therefore the number of degrees of freedom does not change by this procedure. But this would still lead to an increase in computational cost to calculate and use the quadrature formula. It will be later investigated in the numerical examples, whether the term (1) alone is a good enough estimator, and how often one needs to refine the cell K for the quadrature formula to neglect the terms (2).

3.5.1 Reconstruction of the dual solution

The problem in this approach is that the exact dual solution z is needed in order to calculate the error. Since the dual solution in general is not known, it needs to be replaced with an approximation, which is still good enough to not dominate the discretization error, which is the property of interest. Three ideas how to replace the exact dual solution with an approximation will be briefly discussed. Let \tilde{z} be an approximation of z :

$$J(u - u_h) = \underbrace{(f, z - \tilde{z}) - (\nabla u_h, \nabla(z - \tilde{z}))}_{(1)} + \underbrace{(f, \tilde{z}) - (\nabla u_h, \nabla \tilde{z})}_{(2)}.$$

The goal is now to choose a \tilde{z} , which can easily be calculated, such that in the above equation the terms marked with (2) dominate the terms marked with (1). Choosing \tilde{z} as a finite element solution of the same order as u_h does not work, since terms (2) would vanish in this case. Higher order finite elements can be used, for which it can be shown that the term (1) converges with a higher power of h , [4]. But the high computational costs of this method are the disadvantage. Another method to define a function \tilde{z} is described in [4], which is a higher order interpolation of the solution z_h . For example, if trilinear finite element were used for the solution of z_h , a patch-wise triquadratic interpolation could be used to reconstruct a triquadratic solution $z_h^{(2)}$. Since interpolation is very cheap, this approach saves quite some computational costs in comparison to higher order solutions.

For further information on this topic the work of Bangerth and Rannacher [4] is referred.

An often used way to do that is to calculate a higher order reconstruction based on the discrete solution z_h . Therefore, an interpolation operator I_{2h} is defined as follows:

$$I_{2h} : V_h \rightarrow V_{2h}^{(2)}.$$

In this notation $V_{2h}^{(2)}$ defines the space of triquadratic functions defined on a patch consisting of 2^{dim} cells. This means that the cell-wise trilinear function z_h is interpreted as a piecewise trilinear function on this patch. On the patches the function is interpolated with triquadratic elements. This is one of the standard approaches in the DWR and is explained in more details in [4]. In the case of the CutCell method, numerical tests, which will be presented later on, show that this method does not work properly. Remember that the solution was extended with a zero solution to the electrolyte domain in order to avoid complicated

generation of a fitted mesh. Due to that extension there are strong discontinuities in the CutCell solution, which introduce big interpolation errors, if interpolated with continuous functions. Therefore, a changed version of this interpolation approach is used. The problems mentioned above only occur in patches which are intersected by the interface between material and electrolyte phase. This means in patches not intersected, this method can still be used.

Another possibility to reconstruct the dual solution z is by using a higher order method, which of course is more expensive in computation affords. Therefore, using a higher order method in all cells is too expensive, and a mixture of both methods is used in this case.

It should be mentioned at this point that in general the mesh is constructed in a hierarchic way, meaning that the whole domain Ω is chosen as a first mesh, which then consists of only one cell. This mesh will be refined globally several times. Therefore, the mesh refined one time less in comparison to the actual mesh can be chosen as the mesh of patches \mathcal{P}_h . Like this, every cell of the mesh corresponds to a patch uniquely.

Now to reconstruct the dual solution for the error estimators, the patches are divided into two parts, the patches cut by the interface \mathcal{P}_{cut} and the patches not cut by the interface \mathcal{P}_{uncut} . In a first step triquadratic interpolation like described above is used on the uncut patches and therefore create the interpolated solution $z_{h,uncut}^2$. In a second step cell-wise models are solved with triquadratic finite elements to reconstruct the dual solution in the cells coupled to cut patches. The same problem as the original dual problem 3.5.1 is solved with a Dirichlet condition on the whole cell, such that the problem actually only has one degree of freedom. As Dirichlet boundary either the triquadratic interpolated solution $z_{h,uncut}^2$, if the corresponding boundary of the cell is a common boundary with a uncut patch, or the trilinear solution z_h is used as boundary condition. To describe this procedure in more detail, for a specific cell $K \in \mathcal{P}_{cut}$ the cell boundary $\Gamma_{quadratic}$, which is common with a cell of \mathcal{P}_{uncut} , and the rest of the cell boundaries Γ_{linear} are distinguished. With this notation the local quadratic model on the cell K can be defined:

Problem 3.5.5. *For the spaces*

$$\begin{aligned} U_K &= \{v \in C(K \cap \Omega_h) : v = \psi|_{\Omega_h}, \psi \circ T_K \in Q_2, \\ &\quad v = z_{h,uncut}^{(2)} \text{ on } \Gamma_{quadratic}, \\ &\quad v = z_h \text{ on } \Gamma_{linear}\}, \\ V_K &= \{v \in C(K \cap \Omega_h) : v = \psi|_{\Omega_h}, \psi \circ T_K \in Q_2, v = 0 \text{ on } \partial K\}. \end{aligned}$$

find the solution $z_{h,cut}^{(2)}|_K \in U_K$ such that the equation

$$\left(\nabla z_{h,cut}^{(2)}|_K, \nabla \varphi \right)_K = (\nabla \psi, \nabla \varphi)_K \quad \forall \varphi \in V_K$$

holds true.

Since Lagrange finite elements are used, it is evident that for the above problem only one degree of freedom remains.

3.5.2 Refinement strategy

As mentioned already, the goal is to use the error estimators as indicators for local mesh refinement. The idea here is to evaluate the error estimators cell-wise and refine those cells, which have a big error. The exact method will be briefly described in this section.

An easy idea to refine the mesh would be to refine a fixed number of mesh cells or refine a fixed fraction of mesh cells. In these cases, the cell-wise error estimators could be ordered decreasingly and the cells corresponding to the biggest error estimators would be refined. This could be used iteratively until either the total error is smaller than a tolerance or the error in the cells are equilibrated and all cells would be refined, i.e. until global mesh refinement would be used. For this refinement method, the reader is referred to the works of Becker, Braack and Rannacher, [6], and Bangerth and Rannacher, [4].

Another strategy for the mesh refinement, which was introduced by Richter, [45] is used. This strategy uses the assumption that the error η_K in a cell K is reduced by a specific order, if the mesh is refined. From the a priori estimate it is known that the error reduces by an order of $\alpha = 2$, if H^2 regularity of the solution is assumed.

For a good local mesh refinement, the resulting error is reduced, while still keeping as few cells as possible. Therefore, in the work of Richter the functional

$$J_{ref}(m) = N(m)^{\frac{\alpha}{d}} \eta(m)$$

is minimized, where m corresponds to the number of refined mesh cells, $N(m)$ the total number of mesh cells after refinement and $\eta(m)$ the error after refinement. Both $N(m)$ and $\eta(m)$ can both be calculated directly

$$\begin{aligned} N(m) &= N_0 - m + 2^d m, \\ \eta(m) &= \sum_{K \text{ not refined}} \eta_K + \sum_{K \text{ refined}} 2^{-\alpha} \eta_K. \end{aligned}$$

Here the assumption was used that in a refined a cell, the error reduces by a factor of $2^{-\alpha}$, if the cell is refined.

By applying these two properties to the functional J_{ref} and minimizing this functional, the number m of mesh cells to refine is computed.

3.6 Numerical examples

In this section, the CutCell method is used to calculate the effective parameter as described in section 3.1. While calculating the effective parameter, the quality of the error estimators is checked as derived in section 3.5. Since some terms in the error estimators are neglected and the exact dual solution z is replaced by an approximation, the error estimators are compared with the exact error, in order to get an idea of the quality of this approximation. This section is therefore divided into two parts. First some simple microstructures are considered, where an exact solution can be defined by applying a right hand side f of problem 3.1.2 and by adjusting the Dirichlet condition. Since an exact solution is given there, the quality of the error estimators can be tested. In the second part, this method will be applied to real microstructures, which are extracted from real lithium ion battery cathodes.

For all simulations shown in this section the computation cluster BWForCluster MLS&WISO provided by the state of Baden-Württemberg through bwHPC and the German Research Foundation (DFG) through grant INST 35/1134–1 FUGG was used.

3.6.1 Manufactured solutions

First test case: Hyperboloid

For the first test case, a domain $\Omega = (-25, 25)^2 \times (-10, 15)$ is chosen. This domain is subdivided into two parts, by the level-set function

$$\phi(x) = x_1^2 + x_2^2 - (200 + x_3^2).$$

Problem 3.1.2 will be solved in the inner domain, corresponding to a negative value of the level-set function

$$\Omega_{micro} = \{x \in \Omega : \phi(x) < 0\}.$$

The exact solution for this problem is defined by:

$$u_{ex} = x_3^2(x_1^2 + x_2^2).$$

An easy calculation shows that this function has homogeneous Neumann conditions on the boundary $\Gamma = \{x \in \Omega : \phi(x) = 0\}$.

To formulate the continuous and discrete problem, the spaces

$$U = \{\varphi \in H^1(\Omega_{micro}) : \varphi = u_{ex} \text{ on } \Gamma_d \cup \Gamma_u\}, \quad (3.43)$$

$$V = \{\varphi \in H^1(\Omega_{micro}) : \varphi = 0 \text{ on } \Gamma_d \cup \Gamma_u\} \quad (3.44)$$

are defined.

With these spaces, the first test problem can now be formulated.

#cells	h	$J(u - u_h)$	conv. rate J	η	conv. rate η
32768	1.56	3273.25	-	165.567	-
262144	0.78	818.621	1.99	50.1829	1.722
2097152	0.39	204.546	2.00	17.503	1.52
16777216	0.195	51.1379	1.99	4.51	1.95

Table 3.8: Errors of J and error estimators η with corresponding convergence rates for the hyperboloid problem with global refinement.

Problem 3.6.1 (Hyperboloid test problem). *Find the solution $u \in U$, such that*

$$(\nabla u, \nabla \varphi)_{\Omega_{micro}} = (f, \varphi)_{\Omega_{micro}} \quad \forall \varphi \in H_0^1(\Omega_{micro})$$

with

$$f = -\Delta u_{ex} = -2(x_1^2 + x_2^2) - 4x_3^2$$

holds true.

The discrete spaces U_h and V_h are defined as in equation (3.21). The corresponding discrete problem then reads as

Problem 3.6.2 (Hyperboloid test problem discrete). *Find the solution $u_h \in U_h$, such that*

$$(\nabla u_h, \nabla \varphi_h)_{\Omega_h} = (f, \varphi_h)_{\Omega_h} \quad \forall \varphi_h \in V_h$$

holds true.

A representation of the exact solution and the solution domain is shown in figure 3.7. In this figure, the exact solution on the domain Ω_{micro} is shown. Furthermore, the transparent grey area is the part of the mesh \mathcal{T}_h , which does not participate in the solution process, since it is not included in Ω_{micro} .

For this test problem, several cases will be calculated now. Starting with a mesh, consisting of 32768 cells, i.e. a mesh created by globally refining the domain Ω five times, the exact error measured in the functional

$$J(\varphi) = (\nabla \varphi, \nabla \psi)_{\Omega_{micro}}$$

is considered.

In comparison to this exact error, the error estimators in equation (3.42) are considered. The first table 3.8 shows the errors for global refinement.

It is evident that the exact error converges quadratically, as predicted by the a priori estimate 3.5.4. The error estimator only has suboptimal convergence rate. There are two different explanations for the difference to the exact error:

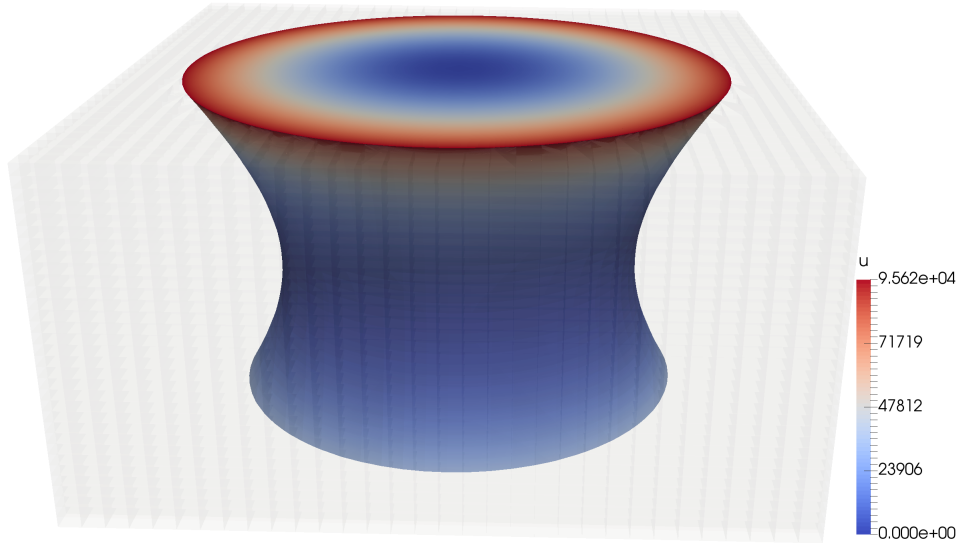


Figure 3.7: Exact solution of the hyperboloid test problem. The transparent grey area shows the part of the mesh that does not influence the solution process.

- The terms (2) of equation (3.42) cannot be neglected.
- The error introduced by replacing z with the reconstruction $z_h^{(2)}$ dominates the error estimator.

As already explained in the previous section, the error due to neglecting some terms of the error estimators can be reduced by simply using a better approximation of the boundary $\partial\Omega_{micro}$. Therefore, the quadrature rule on the cut cells will be created by first prrefining these cells 3 times and then adjust the quadrature formula on every single refined subcell. As mentioned before this procedure does not influence the number of degrees of freedom. The mesh won't be touched by this procedure, the prrefined subcells are only used to create a quadrature formula, and thus creating a better approximation of the boundary. The results for the same problem, with a prrefined quadrature formula are given in table 3.9. As it can be seen by comparing tables 3.8 and 3.9, the better boundary approximation influences the difference of the exact error and the error estimators in non relevant digits. Due to the better boundary approximation, the error introduced by neglecting the stripe terms of the error estimators should get much smaller. Since this is not the case, it seems that the convergence problems are not the result of the neglected terms, but the result of the reconstruction of the

#cells	h	$J(u - u_h)$	conv. rate J	η	conv. rate η
32768	1.56	3263.46	-	165.27	-
262144	0.78	817.04	1.998	50.16	1.72
2097152	0.39	204.40	1.999	17.82	1.493
16777216	0.195	51.12	2.00	4.57	1.963

Table 3.9: Errors of J and error estimators η with corresponding convergence rates for the hyperboloid problem with global refinement with a pre-refined quadrature formula on cut cells.

dual solution.

Second test case: two touching spheres

For the second test case, again a problem is defined such that an exact solution is known. The domain $\Omega = (-25, 25)^2 \times (-30, 35)$ will be defined.

The domain Ω_{micro} should consist of two spheres, which are touching in just one point, the origin. Since, two spheres should be used, two level-set functions are used instead of a single one

$$\begin{aligned}\phi_1(x) &= \|x - (0, 0, -20)^T\| - 20, \\ \phi_2(x) &= \|x - (0, 0, 20)^T\| - 20\end{aligned}$$

to define the domain

$$\Omega_{micro} = \{x \in \Omega : \phi_1(x) < 0 \vee \phi_2(x) < 0\}.$$

Since the domain Ω_{micro} is not connected in this setup, each sphere could just be solved separately. This problem is still considered on both spheres at the same time, because this setup will introduce an additional numerical problem that might also occur in the case of real microstructures. It does not matter how often the mesh is refined, for every mesh there might happen to be a cell K , in which the integration domain is defined by both level-set functions in a disjunct way, as depicted in figure 3.8. The CutCell method is defined in such a way that for every cell K the standard basis functions are integrated only on $K \cap \Omega_{micro}$. On the cell depicted in the figure, this integration domain consists of two disjunct domains, which should be integrated independently. To use the CutCell method correctly, there should be a set of degrees of freedom and corresponding basis functions for each of the integration domains. Due to our implementation of the CutCell method both domains are integrated for the same basis functions and therefore for the same degrees of freedom. This implementation results in a coupling of the integration domain that should not be there.

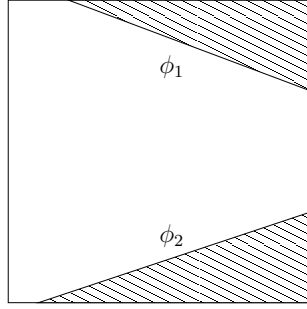


Figure 3.8: Scheme of cell K , in which two different integration domains, depicted by marked domains, are coupled although they shouldn't be.

The effect of these additional errors are discussed in this setup, since an exact solution for this setup can be defined

$$u_{ex} = \begin{cases} \cos(\|x - (0, 0, -20)^T\| \frac{\pi}{400}) & , \text{ if } x_3 < 0 \\ \cos(\|x - (0, 0, 20)^T\| \frac{\pi}{400}) & , \text{ if } x_3 \geq 0. \end{cases}$$

Just like before, the spaces

$$\begin{aligned} U &= \{\varphi \in H^1(\Omega_{micro}) : \varphi = u_{ex} \text{ on } \Gamma_d \cup \Gamma_u\}, \\ V &= \{\varphi \in H^1(\Omega_{micro}) : \varphi = 0 \text{ on } \Gamma_d \cup \Gamma_u\}, \end{aligned}$$

can be defined to formulate the problem setting.

Problem 3.6.3 (Two touching spheres test problem). *Find the solution $u \in U$, such that*

$$(\nabla u, \nabla \varphi)_{\Omega_{micro}} = (f, \varphi)_{\Omega_{micro}} \quad \forall \varphi \in H_0^1(\Omega_{micro})$$

with

$$f = -\Delta u_{ex}$$

holds true.

The corresponding discrete problem reads as

Problem 3.6.4 (Two touching spheres test problem discrete). *Find the solution $u_h \in U_h$, such that*

$$(\nabla u_h, \nabla \varphi_h)_{\Omega_h} = (f, \varphi_h)_{\Omega_h} \quad \forall \varphi \in V_h$$

holds true.

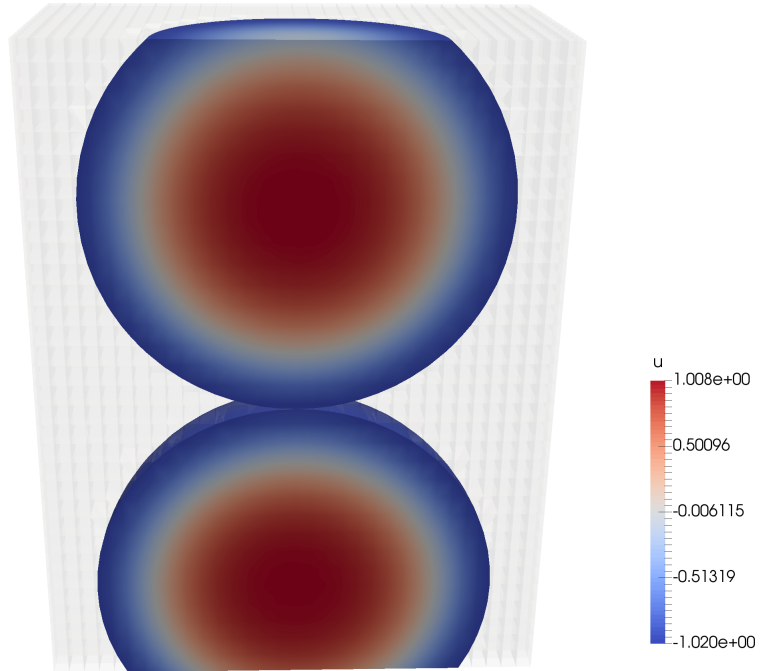


Figure 3.9: Exact solution of the two touching spheres test problem. The transparent grey area shows the part of the mesh that does not influence the solution process.

The exact solution is depicted in figure 3.9, where the visualisation is restricted to positive values in the x -direction to be able to view the solution inside of the spheres.

The starting mesh, is given by a 5 times global refinement, like in the hyperboloid case.

To test the influence of the wrong coupling described above, this case is tested once for global refinement and once for local refinement, where the refinement strategy is again given as described in section 3.5.2.

#cells	wrong coupl. cells	h	$J(u - u_h)$	conv. rate J	η
32768	28	1.56	0.105	-	0.0403
262144	116	0.78	0.011	3.21	-1.99e-5
2097152	48	0.39	0.00639	0.82	0.00131
16777216	152	0.195	0.00232	1.46	0.000267

Table 3.10: Errors of J and error estimators η with corresponding convergence rates for the two touching spheres problem with global refinement.

#cells	wrong coupled cells	$J(u - u_h)$	η
32768	28	0.105	0.0403
111728	116	0.02856	0.0116
687380	36	0.00149	0.00335
5065628	104	0.00116	0.000737
39178077	364	0.000633	9.62e-5

Table 3.11: Errors of J and error estimators η with corresponding convergence rates for the two touching spheres problem with local refinement.

Tables 3.10 and 3.11 show that the wrong coupling indeed influences the solution behavior, since now not even the exact error converges with the correct convergence order. But it can also be seen that error estimator is still suited as refinement indicators. In the case of global refinement, the exact error has a value of 0.00232 with over 16 million cells. With the help of local refinement, a smaller error can be established already with only using roughly 700 thousand cells. Therefore, a smaller error is achieved by using less than a tenth of the number of cells in comparison with global mesh refinement. This result confirms that even though the error estimators are not ideal to actually estimate the error, they still work just fine as refinement indicators for the local refinement of the mesh.

The number of wrongly coupled cells is more or less the same in both approaches. This behavior is meaningful, since the wrong coupling can only occur in an area around the touching point of the two spheres. Refinement of cells in this area leads to shrinking of this area if wrong coupling occurs. If the mesh cell depicted in figure 3.8 is refined, the wrong coupling would not occur anymore. In cells closer to the touching point refinement introduces a larger number of cells with wrong coupling. Therefore, in total the number of wrong coupled cells is expected to remain in a similar range during refinement. With an additional high implementation afford, the problem of this wrong coupling could be solved, by introducing additional degrees of freedom locally.

3.6.2 Real microstructures

After investigating the test cases with a known exact solution, now a real microstructure is considered. The real microstructures considered here were investigated within the project “HiKoMat - Werkstoffentwicklung hierarchisch strukturierter Kompositmaterialien für elektrochemische Energiespeicher”, funded by the federal ministry of economical affairs and energy.

Just like in the test cases, the domain of the real microstructure will be defined by several level-set functions. The microstructure domain will then be given

by the domain, in which at least one level-set function has negative value. The number of level-set functions to define the domain Ω_{micro} can get very large here, up to several thousand functions, where each function describes a single particle of the microstructure, which can intersect other particles.

To get a good representation of the single particles, spherical harmonics functions are used, as described in [52]. Therefore, a single level-set function in spherical coordinates is defined as

$$\phi(r, \theta, \varphi) = \sum_{l=0}^L \sum_{m=-l}^l \alpha_{lm} Y_{l,m}(\theta, \varphi) - r,$$

where $Y_{l,m}$ are the spherical harmonics basis functions, which are defined with the help of Legendre polynomials, [52]. For $l \in \mathbb{N}$, the Legendre polynomials $P_l : [-1, 1] \rightarrow \mathbb{R}$ are given by

$$P_l(x) = 2^{-l} \frac{1}{l!} \frac{d^l}{dx^l} (x^2 - 1)^l.$$

The next step is to define the associated Legendre functions $P_{l,m} : [-1, 1] \rightarrow \mathbb{R}$ for $l \in \mathbb{N}$, $m \in \{0, \dots, l\}$

$$P_{l,m}(x) = (-1)^m (1 - x^2)^{m/2} \frac{d^m}{dx^m} P_l(x).$$

Finally the spherical harmonic functions $Y_{l,m} : [0, \pi] \times [0, 2\pi] \rightarrow \mathbb{R}$ are then given by

$$Y_{l,m}(\theta, \varphi) = \sqrt{\frac{(2l+1)(l-m)!}{4\pi(l+m)!}} P_{l,m}(\cos(\theta)) \begin{cases} \cos(m\varphi) & , \text{ if } m \geq 0 \\ \sin(m\varphi) & , \text{ if } m < 0, \end{cases}$$

for $l \in \mathbb{N}$ and $m \in \{-l, \dots, l\}$.

The following real microstructure will be represented by 2822 particles defined in the domain $\Omega = (0, 499)^3$. Each particle is represented by a separate level-set function that will be a spherical harmonics function of degree $L = 10$. The domain Ω_{micro} will then be defined by

$$\Omega_{micro} = \{x \in (0, 499)^3 : \exists i = 1, \dots, 2822, \phi_i(x) < 0\}.$$

On this domain the same problem as above is defined.

Problem 3.6.5. Find $u \in H_d^1(\Omega_{micro})$, such that the equation

$$(\nabla u, \nabla \varphi)_{\Omega_{micro}} = 0 \quad \forall \varphi \in H_0^1(\Omega_{micro})$$

holds true.

The discrete spaces U_h and V_h are defined like in equation (3.21). Then the discrete problem reads as follows.

Problem 3.6.6. Find the solution $u_h \in U_h$, such that the equation

$$(\nabla u_h, \nabla \varphi_h)_{\Omega_h} = 0 \quad \forall \varphi_h \in V_h$$

holds true.

In figure 3.10 the real microstructure is shown.

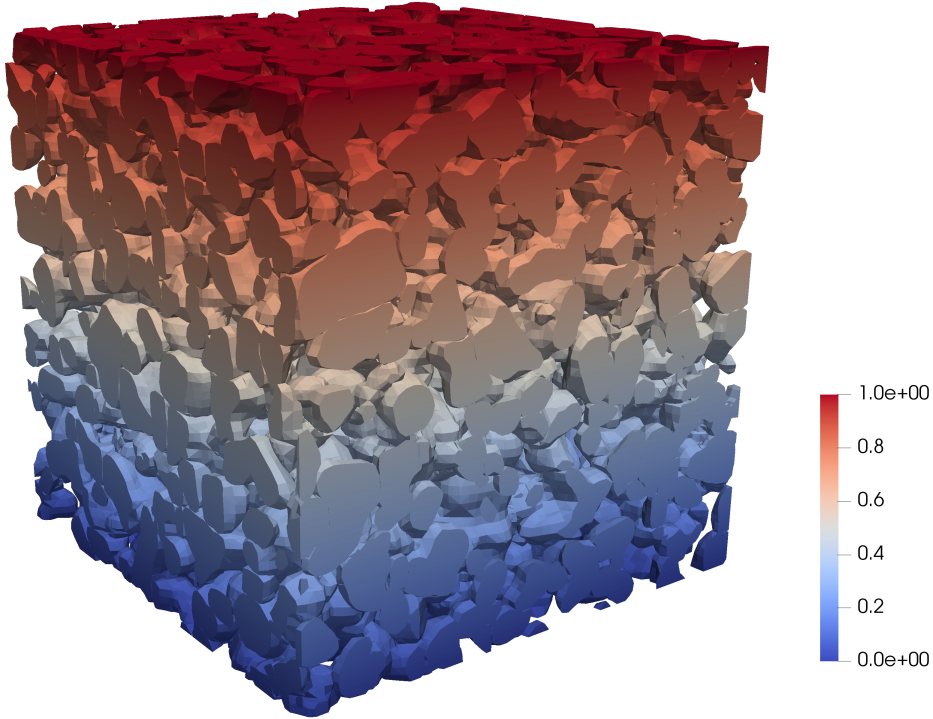


Figure 3.10: Real microstructure with 2822 particles.

In the following tables 3.12 and 3.13 a comparison of the values of the effective diffusion coefficients D_{eff} for $D_{bulk} = 1$ and the error estimators will be done between global and local refinement. The error estimators are calculated with respect to the flux over the boundary Γ_d , while the effective coefficients are calculated as a scaling of this flux (3.16). Therefore, the same scaling will be applied to the error estimators, such that they estimate the error of the effective coefficient \tilde{J} .

$$\tilde{J}(u) = \frac{L}{|\Gamma_D|} J(u) = \frac{1}{499} J(u). \quad (3.45)$$

#cells	#dofs	D_{eff}	scaled error estimators
262144	269705	0.4081	0.01039
2097152	1885192	0.3669	0.00458
16777216	12998871	0.3499	0.00182

Table 3.12: Effective diffusion coefficient and scaled error estimator for a real microstructure with global refinement.

#cells	#dofs	D_{eff}	scaled error estimators
262144	269705	0.4081	0.01039
1481593	1734030	0.3781	0.00554
9870372	11127087	0.35321	0.00246
12750109	14778933	0.34747	0.001701

Table 3.13: Effective diffusion coefficient and scaled error estimator for a real microstructure with local refinement.

This scaling won't add additional error distributions, since the scaling factors are defined by the domain Ω , which is known exactly.

In figure 3.11, the value of D_{eff} is shown depending on the number of used degrees of freedom. By a comparison of the results shown in figure 3.11 and in tables 3.12 and 3.13, it is evident that the local mesh refinement does not benefit the solution process of this problem. This real microstructure is defined by a union of many particles. The refinement used for the numerical examples might still be too coarse, such that each particle is reconstructed only by a small number of mesh cells. Therefore, a finer mesh might be needed in order to show the expected results. But a better reconstruction of the particles by further mesh refinement was not possible due to time and RAM restrictions on the used compute cluster.

3.6.3 Smaller real microstructure

The second real microstructure, is a smaller one, consisting of 100 particles. Furthermore, the structure of each particle is simpler by choosing a reconstruction of the microstructure with spheres.

A cutout of this microstructure is depicted in figure 3.12.

As before each particle defines a single level-set function ϕ_i . With these the domain of interest can be defined.

$$\Omega_{micro} = \{x \in (0, 5.22)^3 : \exists i = 1, \dots, 100, \phi_i(x) < 0\}.$$

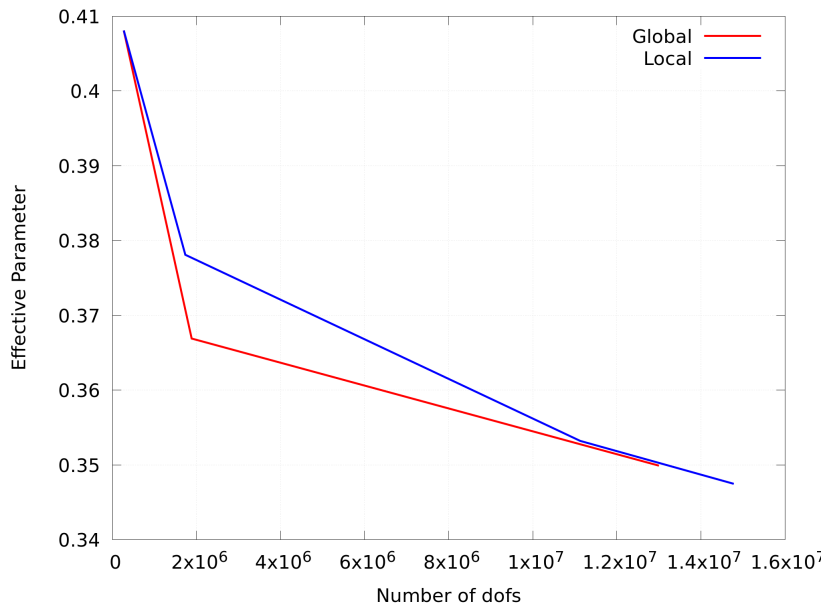


Figure 3.11: Comparison of results for real microstructure with global and local refinement.

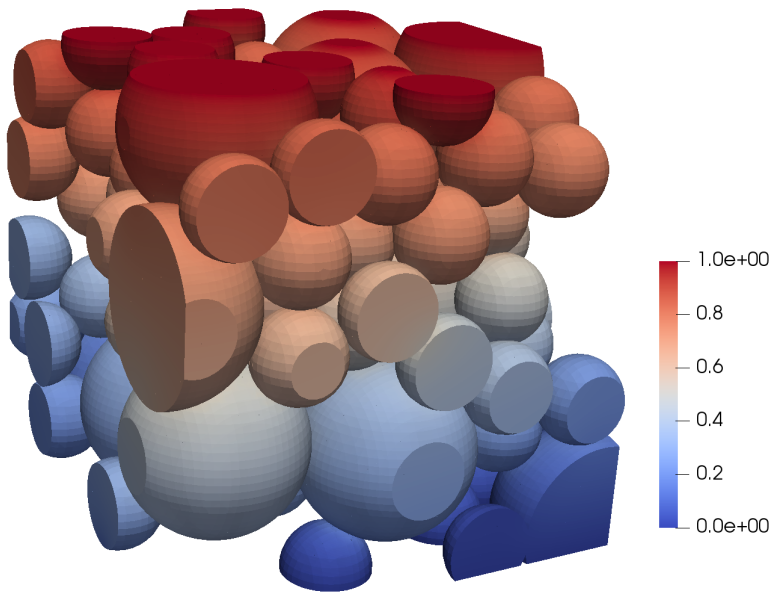


Figure 3.12: Visualization of the second real microstructure using spheres to reconstruct the material domain.

#cells	#dofs	D_{eff}
4096	4739	0.3492
32768	32321	0.3531
262144	225790	0.3350
2097152	1603322	0.3168
16777216	11801406	0.3058

Table 3.14: Effective diffusion coefficient and scaled error estimator for a smaller real microstructure with global refinement.

#cells	#dofs	D_{eff}	scaled error estimators
4096	4739	0.3492	0.0468
4495	5608	0.3493	0.0096
22226	29130	0.3585	0.00824
89839	124697	0.3432	0.0721
260310	364351	0.3168	0.00448
934396	1267090	0.3059	0.00240
1313537	1809301	0.2985	0.0020
4239040	5788829	0.2950	0.0011
6169507	8472473	0.2931	5.045e-04
8662032	12006981	0.2917	5.58e-04

Table 3.15: Effective diffusion coefficient and scaled error estimator for a smaller real microstructure with local refinement.

In this case each level-set function is defined as a spherical harmonics function of order $L = 0$.

Since the continuous and discrete problem setting is given in the same way as problems 3.6.5 and 3.6.6, this won't be repeated again.

The results for this microstructure are given in table 3.14 for global refinement and in table 3.15 for local refinement.

The results shown in these tables shows that the error estimator seems to underestimate the actual error again. The values of D_{eff} change in a larger range under refinement than the error estimator would suggest.

But in the same way as in the test cases, it can be observed here that the error estimators work as refinement indicators for local mesh refinement. Figure 3.13 shows that similar values for D_{eff} can be calculated for much fewer degrees of freedom. A comparison of the tables show that the global refinement used 11801406 degrees of freedom to calculate the parameter $D_{eff} = 0.3058$, while with local refinement only 1267090 degrees of freedom are used for the same result.

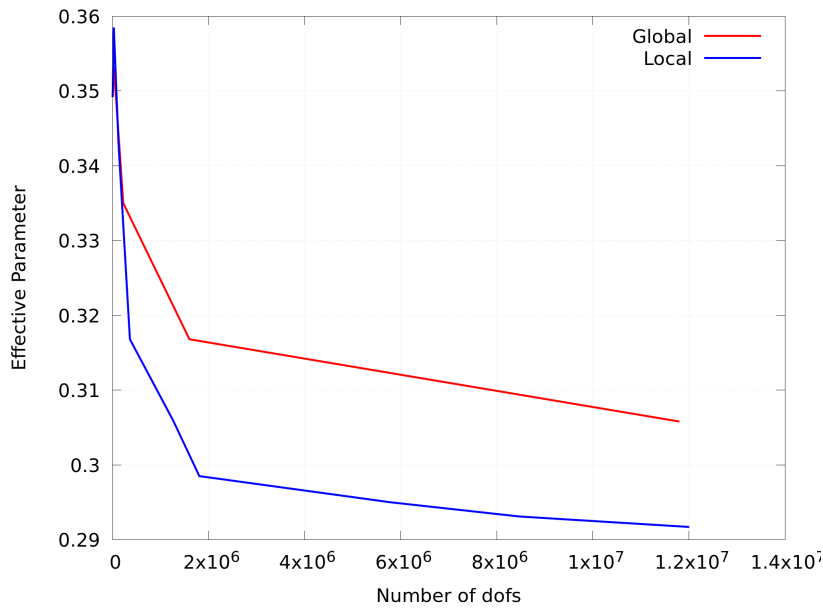


Figure 3.13: Comparison of results for small real microstructure with global and local refinement.

3.6.4 Comparison with voxel based solver

Using the CutCell method for the solution process of the cell problem is a new approach, the state of the art method is to use the standard finite element method. It was already discussed that the challenge in this approach is the definition of a mesh, which represents the microstructure properly. This challenge is simplified by using a voxel based reconstruction, [19], [26].

For this approach a cuboid is defined, which contains the microstructure. This cuboid is subdivided into uniform voxel. This process can be compared to the creation of a mesh, as described in section 3.1. Depending on the microstructure each voxel is either defined to be completely in the active material domain, or in the electrolyte domain. This procedure automatically produces a mesh that can also be used for the standard FEM.

In this section, a comparison between the voxel based solver and the CutCell based solver will be done. This comparison will be done for the real microstructures considered above.

Since no voxel data for these microstructures are available, this data is created based on the same mesh that was used for the CutCell method. For each mesh cell the center is considered in order to determine, in which domain this cell is contained. If the center of the cell is in the domain associated with a negative sign of at least one level-set function, the cell is defined as a part of the active

#cells	#dofs CutCell	D_{eff} CutCell	#dofs voxel	D_{eff} Voxel
262144	269705	0.4081	239698	0.3988
2097152	1885192	0.3669	1640354	0.3607
16777216	12998871	0.3499	11812689	0.3464

Table 3.16: Comparison of the effective diffusion parameter for a CutCell and a voxel based approach for the first real microstructure.

#cells	#dofs CutCell	D_{eff} CutCell	#dofs voxel	D_{eff} Voxel
262144	225790	0.3350	202789	0.3635
2097152	1603322	0.3168	1484178	0.3313
16777216	11801406	0.3058	11272336	0.3141

Table 3.17: Comparison of the effective diffusion parameter for a CutCell and a voxel based approach for the second real microstructure.

material domain.

Tables 3.16 and 3.17 show the result of the voxel based solution approach in comparison to the CutCell based approach for several global refinement steps. These results are also shown graphically in figures 3.14 and 3.15.

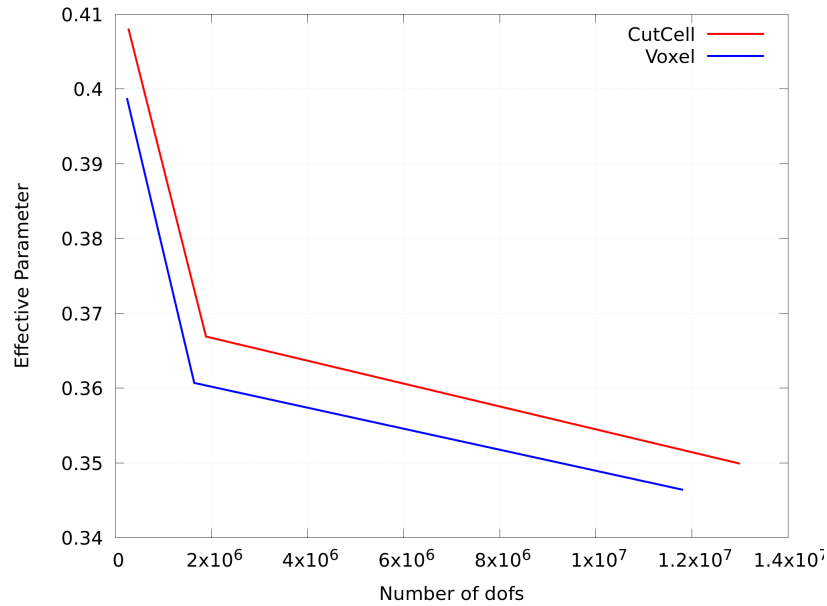


Figure 3.14: Comparison of results for first microstructure between CutCell and voxel based approach.

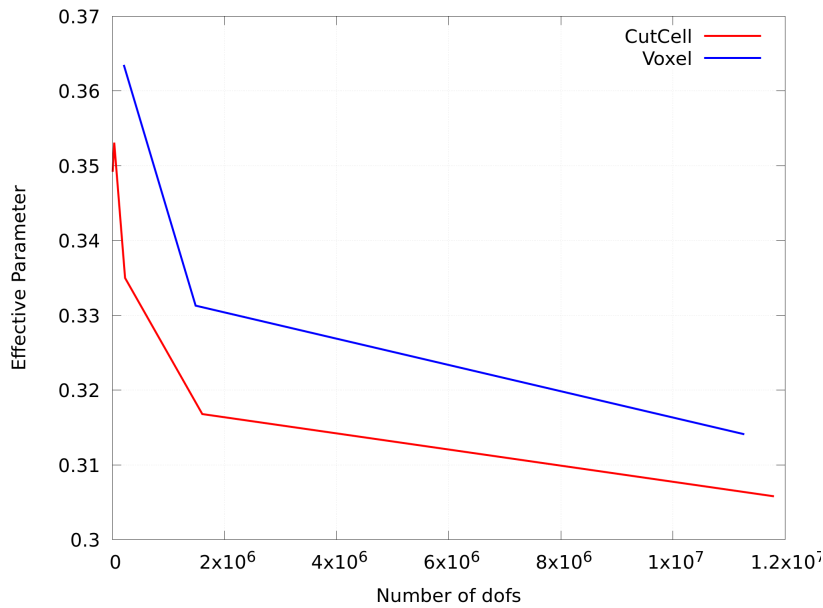


Figure 3.15: Comparison of results for second microstructure between CutCell and voxel based approach.

These results show a difference between the calculation of the effective diffusion parameter D_{eff} based on a CutCell approach and a voxel approach. For the first real microstructure the voxel based approach shows smaller values in comparison to the CutCell approach, while the second real microstructure shows that the CutCell results are smaller.

The difference in the results can be explained by the reconstruction properties of the microstructure. Figure 3.16 shows the microstructure reconstruction for a voxel based approach.

It is evident that this approach leads to a worse approximation of the boundary of the microstructure. Even with mesh refinement the boundary won't converge to the correct boundary, but the voxel based one will always show a larger surface. Since on this boundary a homogeneous Neumann condition is prescribed, the approximation of the boundary influences the approximation of the solution and therefore the flux.

This suggests that the calculation of effective parameter with the CutCell approach converges faster in comparison with the state of the art voxel based approach.

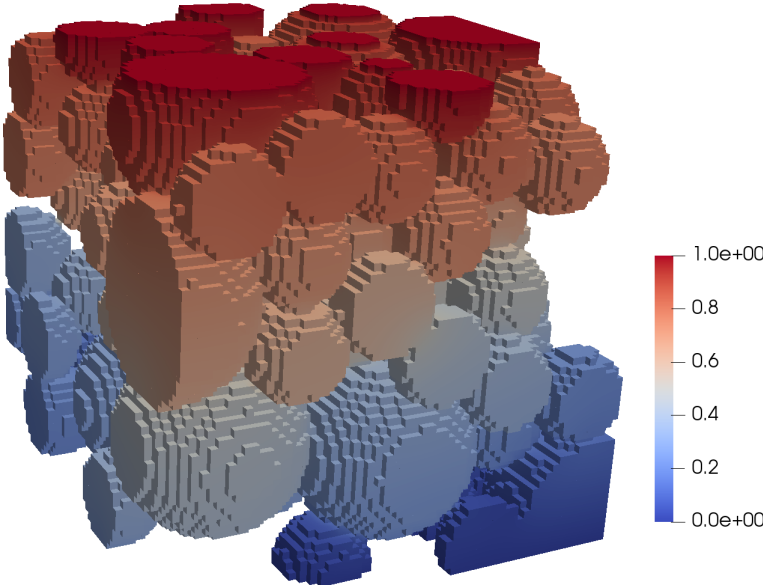


Figure 3.16: Visualization of the voxel based solution for the second real microstructure.

4 Solution process of LIB model

After the cell problem was solved in the previous chapter, this chapter considers the solution process of the extended P2D LIB model. First, a theoretical result is recapitulated to show existence and uniqueness of the solution of this problem. Then the discretization of this model is derived, which is complicated by the pseudo two-dimensional structure. In every time step a non linear problem needs to be solved, which is done with the help of Newton's method. Therefore, the condition number of the Jacobian matrix for this problem is considered, before an a posteriori error estimators as refinement indicators for local mesh refinement is derived and its quality is tested. The last sections show the behavior of this model, where a special emphasis is in the behavior due to the reconstruction of the active material with spheres of different radii.

4.1 Newman Model

In this section, the model of Ender [25] will first be presented in strong formulation, before stating the model in weak formulation. Furthermore, the well posedness of the model will be investigated. A summary of the results for existence and uniqueness published by Díaz, Gómez-Castro and Ramoz is recapitulated here, [21]. Their results substantiate the definition of the weak formulation that is used for the derivation of the error estimator in this section.

In chapter 2, the derivation of the Newman model was done with the help of a homogenization process of the full three-dimensional model. This was done exemplary only for one electrode. A real battery consists of two electrodes, anode and cathode, which are separated by a separator, which is in general filled with electrolyte. Due to the homogenization process, both electrodes will have a P2D structure, while the separator is a one-dimensional model. The investigation of the battery model is restricted to a half cell, which means that only one electrode (either cathode or anode) and half a separator are used, where the boundary conditions at the separator are given such that the half cell behaves similarly to a full cell. Nevertheless the model will be defined for the whole cell and adjusted to a half cell later.

To define the model equations in one part of the cell, the different domains will be defined first. Due to the homogenization process, the homogenized equations are

defined on both electrodes and the separator, therefore a one-dimensional domain $\Omega_{hom} = (0, L)$ is defined, describing the height of the full cell. This domain can be separated into different domains $\Omega_{hom} = (0, L_{anode}) \cup (L_{anode}, L_{separator}) \cup (L_{separator}, L_{cathode})$, where the domains corresponding to an electrode are given by the notation $\Omega_{el} = (0, L_{anode}) \cup (L_{separator}, L_{cathode})$. At every point $x \in \Omega_{el}$, a second one-dimensional domain is defined, which will always be the unit domain $\Omega_r = (0, 1)$ by a transformation of the domain $(0, R_i) \rightarrow \Omega_r$ for each radius R_i , $i = 1, \dots, N_R$. The domain Ω_r should actually be a three-dimensional domain in general, representing the active material particles. But since spherical particles are assumed and radial symmetry is used for this problem, the 3D domain can be represented by this 1D domain. Furthermore, the following space-time domains are considered, $Q_{hom} = \Omega_{hom} \times T$, $Q_{electrode} = \Omega_{el} \times T$ and $Q_r = (\Omega_{electrode} \times \Omega_r) \times T$, where $T = (0, t_{end})$ represents the time domain. The model equations then reads as follows in strong formulation:

Problem 4.1.1. *Find solutions*

$$\begin{aligned} c_l &\in \mathcal{C}^1(T, \mathcal{C}^2(\Omega_{hom})), \\ \phi_l &\in \mathcal{C}(T, \mathcal{C}^2(\Omega_{hom})), \\ \phi_s &\in \mathcal{C}(T, \mathcal{C}^2(\Omega_{el})), \\ c_{s,i} &\in \mathcal{C}^1(T, \mathcal{C}^2(\Omega_r) \times \mathcal{C}(\Omega_{el})), \end{aligned}$$

such that the equations

$$\varepsilon_l \partial_t c_l - \partial_x D_l \partial_x c_l - \frac{1-t_+}{F} q_{ct} = 0 \quad \text{in } Q_{hom}, \quad (4.1)$$

$$-\partial_x \sigma_l \partial_x \phi_l - \partial_x \kappa \partial_x \log c_l - q_{ct} = 0 \quad \text{in } Q_{hom}, \quad (4.2)$$

$$-\partial_x \sigma_s \partial_x \phi_s + q_{ct} = 0 \quad \text{in } Q_{electrode}, \quad (4.3)$$

with $\kappa := \frac{2RT}{F} \sigma_l (1-t_+) \left(1 + \frac{\partial \log f_{\pm}}{\partial x}\right)$ hold true.

For every $x \in \Omega_{el}$ and $i = 1, \dots, N_R$ the concentration equation in the effective particle for the i -th radius is given by:

$$\partial_t c_{s,i} - \frac{1}{r^2 R_i^2} \partial_r r^2 D_s \partial_r c_{s,i} = 0 \quad \text{in } Q_r. \quad (4.4)$$

The boundary conditions for the solutions (c_l, ϕ_l, ϕ_s) are given by:

$$\partial_n c_l(0) = 0 \quad \partial_n c_l(L) = 0, \quad (4.5)$$

$$\partial_n \phi_l(0) = 0 \quad \partial_n \phi_l(L) = 0, \quad (4.6)$$

$$\partial_n \phi_s(0) = -j_L \quad \sigma_s^{eff} \partial_n \phi_s(L_{anode}) = 0, \quad (4.7)$$

$$\partial_n \phi_s(L_{separator}) = 0 \quad \sigma_s^{eff} \partial_n \phi_s(L) = j_L. \quad (4.8)$$

For every $x \in \Omega_{el}$, the boundary condition of the solution $c_{s,i}$, $i = 1, \dots, N_R$, which are defined in spherical coordinates, is given by the coupling to the other solutions:

$$\partial_n c_{s,i}(0) = 0 \quad D_s \partial_n c_{s,i}(R_i) = -\frac{R_i^2}{3\varepsilon_s} \frac{a_{spec,i} j_{ct,i}}{F}. \quad (4.9)$$

Finally to define the model completely, only the coupling term between the different equations is missing. The coupling is defined by a Butler-Volmer type equation, describing an exchange current density between the material and the electrolyte phase.

$$q_{ct} = \begin{cases} \sum_{i=1}^{N_R} a_{spec,i} j_{ct,i}, & \text{in } \Omega_{el} \\ 0, & \text{else,} \end{cases} \quad (4.10)$$

$$j_{ct,i} = j_0 \cdot \left(\exp\left(\left(1 - \alpha\right) \frac{R_g T}{F} \eta\right) - \exp\left(-\alpha \frac{R_g T}{F} \eta\right) \right) \quad (4.11)$$

$$j_0 = F \cdot k \cdot c_l^\alpha \cdot c_s(R_i)^{1-\alpha} \cdot \left(1 - \frac{c_s(R_i)}{c_{s,max}}\right)^\alpha \quad (4.12)$$

$$\eta = \phi_s - \phi_l - \Phi_{OCV}(c_{s,i}(R_i)) - \frac{RT}{F} \log \frac{c_l}{c_{l,0}} \quad (4.13)$$

In comparison to chapter 2, there was a small change of notation, as mentioned in remark 2.2.1. The notation for the porosity of the microstructure was changed from δ to the more commonly used ε_l .

Remark 4.1.2. *It is easy to show that this problem cannot have a unique solution, since to the potentials $\phi_l + c$ and $\phi_s - c$ shifted by the same constant c still are a solution of the same problem. The standard way to solve this problem is to fix one potential, in literature generally ϕ_l is chosen, to a specific value. This is achieved by replacing one Neumann boundary condition of ϕ_l by a Dirichlet condition.*

Remark 4.1.3. *It was ready mentioned that our investigation is done only on a half cell. To achieve a half cell, the model is restricted to the cathode and a half separator. Furthermore, the boundary conditions are adjusted. The concentration of lithium ions in the electrolyte c_l is fixed at the midpoint of the separator. Another possibility is to define a suitable flux condition for c_l at the midpoint of the separator, which produces almost the same output as the Dirichlet condition. In this thesis the Dirichlet condition is chosen.*

Remark 4.1.4. *In this set of equations the transformation of the particle domains $(0, R_i)$ to the domain Ω_r is already contained, resulting in a scaling with factors of R_i at specific terms in the particle equations.*

In general, the well-posedness of the strong formulation cannot be shown. Therefore, this problem is rewritten in weak formulation. Then a result for existence and uniqueness by Díaz, Gómez-Castro and Ramos [21] is stated for a so called weak-mild solution, which implies the well-posedness of the weak solution.

According to the paper of Díaz the solution spaces are defined for a given time interval $T = (0, t_{end})$

$$\begin{aligned} U &:= \mathcal{C}(T, X) \\ X &:= H^1(\Omega_{hom}) \times H^1(\Omega_{hom}) \times H^1(\Omega_{el}), \\ V &:= \mathcal{C}(T, Y), \\ Y &:= L^2(\Omega_{el}, H_r^1(\Omega_r))^{N_R}. \end{aligned}$$

The notation H_r^1 denotes the space of H^1 functions that are integrated using spherical coordinates.

For simplicity, the homogenized solutions are combined to one vector-valued solution $u = (c_l, \phi_l, \phi_s)$. Furthermore, all considered radii of the particle solutions are combined to a vector valued solution $v = (c_{s,1}, \dots, c_{s,N_r})$.

The problem in weak formulation is then given by

Problem 4.1.5 (LIB weak formulation). *Find the solutions $u \in U$ and $v \in V$ such that the equations*

$$\int_T (\mathcal{E} \partial_t u, \varphi) + A(u, v)(\varphi) dt + (u(0) - u^0, \varphi(0)) = 0 \quad (4.14)$$

$$\int_{\Omega_{hom}} \int_T (\partial_t v, \psi)_r + B_x(u(x), v(x, \cdot))(\psi(x, \cdot)) dt + (v(0) - v^0, \psi(0))_r dx = 0. \quad (4.15)$$

hold true for all $\varphi \in U$ and $\psi \in V$.

Remark 4.1.6. *It needs to be mentioned here that for simplicity the term $(\mathcal{E} \partial_t u, \varphi)$ was used, where the time derivative only applies to the first component of the vector valued function u . This means the matrix \mathcal{E} is diagonal with entries $\mathcal{E} = \text{diag}(\varepsilon_l, 0, 0)$.*

In this notation the vector-valued semilinear form A is defined by:

$$\begin{aligned} A_1(u, v)(\varphi) &= (D_l^{eff} \partial_x c_l, \partial_x \varphi) - \left(\frac{1 - t_+}{F} q_{ct}, \varphi \right), \\ A_2(u, v)(\varphi) &= (\sigma_l^{eff} \partial_x \phi_l, \partial_x \varphi) + (\kappa \partial_x \log c_l, \partial_x \varphi) - (q_{ct}, \varphi), \\ A_3(u, v)(\varphi) &= (\sigma_s^{eff} \partial_x \phi_s, \partial_x \varphi) - j_L \varphi(L) + (q_{ct}, \varphi). \end{aligned}$$

and for $x \in \Omega_{el}$, B_x is given by:

$$\begin{aligned} B_x(u(x), v(x))(\psi(x)) &= (B_{x,i}(u(x), v_i(x))(\psi_i(x)))_{i=1}^{N_R}, \\ B_{x,i}(u(x), v_i(x))(\psi_i(x)) &= (\partial_t c_{s,i}(x), \psi(x))_r + (D_s \partial_r c_{s,i}(x), \partial_r \psi(x))_r \\ &\quad - \frac{R_i^3 a_{spec,i}}{3\varepsilon_s vol_i} j_{ct,i} \psi(x, R_i). \end{aligned}$$

Here the notation (\cdot, \cdot) was used for the L^2 inner product on Ω_{hom} and $(\cdot, \cdot)_r$ for the L^2_r inner product on Ω_r . The subscript of the form B_x corresponds to an evaluation of the functions u , v and ψ in a point $x \in \Omega_{el}$. Since this point is defined in the subscript of B_x , the argument x of these functions will be skipped from now on.

Remark 4.1.7. *In literature, [25], [30], the model is often defined directly for a discrete distribution of particle equations over the domain Ω_{el} . In a continuous setting, this would correspond to a distribution of an infinite number of equations for almost every points $x \in \Omega_{el}$. This other notation is equivalent to the model stated here, since enough regularity is assumed to allow integration of c_s over $x \in \Omega_{el}$. The vice versa direction can be shown, by choosing $\psi \in V$ as an approximation of the Delta Dirac function in the direction of $x \in \Omega_{el}$. The formulation with the integral is more intuitive, when defining the discrete problem.*

4.1.1 Existence and Uniqueness

As mentioned before the result for existence and uniqueness of the solution of the LIB model in weak formulation was proven in [21].

In this section, a theorem for existence and uniqueness for the LIB model is stated using different assumptions.

Remark 4.1.8. *In the paper, [21], the existence is shown for a weak mild solution of the model. Since a weak mild solution is also a weak solution, the result is directly given for weak solutions, which is the interesting one here. Furthermore, a constant temperature T is assumed in the model, while the authors of the paper have an additional equation in the model, regarding heat transport.*

Assumption 4.1.9. *For the initial solutions, the following regularity is assumed:*

$$\begin{aligned} c_{l,0} &\in H^1(\Omega_{hom}), & 0 &< c_{l,0} \\ c_{s,0} &\in \mathcal{C}(\Omega_{el} \times \Omega_r), & 0 &< c_{s,0} < c_{s,max}. \end{aligned}$$

Assumption 4.1.10. For the diffusion coefficients and the conductivities in the model equations, the following regularity

$$\begin{aligned} D_l &\in L^\infty(\Omega_{hom}), & D_l &\geq D_{l,0} > 0, \\ \sigma_l &\in \mathcal{C}((0, \infty)), & \sigma_l &\geq \sigma_{l,0} > 0, \\ \sigma_s &\in L^\infty(\Omega_{el}), & \sigma_s &\geq \sigma_{s,0} > 0 \end{aligned}$$

is assumed.

Assumption 4.1.11. For the exchange current density $j_{ct} = j_{ct}(c_l, c_s, \eta)$ and the open circuit voltage $\Phi_{OCV}(c_s)$

$$\begin{aligned} j_{ct} &\in \mathcal{C}^2((0, \infty), (0, c_{s,max}), \mathbb{R}), \\ \frac{\partial j_{ct}}{\partial \eta} &> 0, \\ \Phi_{OCV} &\in \mathcal{C}^2((0, c_{s,max})). \end{aligned}$$

is assumed.

Remark 4.1.12. The paper [21] shows the existence for a more general form of the LIB model and therefore needs more assumptions than stated here. Focusing on the model 4.1.5, unneeded assumptions are skipped. It is evident to show that the assumptions above are all fulfilled for the model 4.1.5.

With these assumptions, the theorem proving existence and uniqueness of problem 4.1.5 can now be stated.

Theorem 4.1.13. Under assumptions 4.1.9, 4.1.10 and 4.1.11, there exists a unique weak solution to problem 4.1.5 in the interval $[0, t_{end})$. For $t \rightarrow t_{end}$, one of the following properties holds true:

$$\begin{aligned} \min_{\Omega_{el} \times \Omega_r} c_s &\rightarrow 0, \\ \max_{\Omega_{el} \times \Omega_r} c_s &\rightarrow c_{s,max}, \\ \min_{\Omega_{hom}} c_l &\rightarrow 0, \\ \max_{\Omega_{hom}} c_l &\rightarrow \infty. \end{aligned}$$

Proof. This theorem is proven in [21] with the help of group theory and by using a Green operator. First existence for both elliptic equations is shown under the assumption that the solutions of the parabolic equations are given. In a second step existence of the parabolic equations is shown under the assumption

that the solutions of the elliptic equations are given. Finally the existence of the whole model for a small enough time interval is shown using Banach's fixed point theorem. This result can be extended to a larger time interval by a standard theorem in the theory of ordinary differential equations. \square

Remark 4.1.14. *This theorem shows existence of a solution, up until a point in time, when certain criteria are fulfilled. These abort criteria also are meaningful from a physical point of view. If the concentration of lithium in either electrolyte or active material tends to zero, intercalation or deintercalation of lithium cannot occur anymore. The same holds true, if the concentration of lithium in the active material tends to the maximal concentration. In this case no lithium can be intercalated anymore and therefore the charge/discharge process stops.*

4.1.2 Discretization

The model is a coupled system of two parabolic and two elliptic equations, therefore discretization in both time and space is needed. This discretization will be done using a Galerkin method in space and time, where the ansatz and test spaces for the time domain are chosen such that a one step method, the implicit Euler method, is used.

Time discretization

For the time discretization, therefore a time mesh \mathcal{T}_k of the interval $(0, t_{end})$ is defined, such that

$$0 = t_0 < t_1 < t_2 < \dots < t_N = t_{end},$$

with the time step size

$$k_m = t_m - t_{m-1}, m = 1, \dots, N_t.$$

For the solution at a specific time t_m , the notation

$$(u^m, v^m) = (u(t_m), v(t_m))$$

is used.

Using this time mesh and an implicit Euler scheme to discretize problem 4.1.5 in time, but not in space, a semi discrete problem is given.

Problem 4.1.15 (Semi discrete problem in time). *For given functions $u^0 \in L^2(\Omega_{hom})$ and $v^0 \in L^2(\Omega_{el}, L_r^2(\Omega_r))^{N_R}$, find solutions $u^m \in X$ and $v^m \in Y$ for*

$m = 1, \dots, N_t$, such that the equations

$$\begin{aligned} (u^m - u^{m-1}, \varphi^m) &= k_m A(u^m, v^m)(\varphi^m) & \forall \varphi^m \in X, \\ (v^m - v^{m-1}, \psi^m)_r &= k_m B(u^m, v^m)(\psi^m), & \forall \psi^m \in Y, \end{aligned}$$

hold true.

Remark 4.1.16. *It should be mentioned that the time discretization scheme was written as a one step method, the implicit Euler scheme. It is well known that the implicit Euler scheme is equivalent with a Galerkin method, to be more precise, the $dG(0)$ method, where integration is done with a right sided box rule. This equivalence will be important later, when dealing with the a posteriori error estimation in section 4.3.*

Discretization of the homogenized domain

In order to actually solve the problem 4.1.5 in space, the finite element method will be used. The big challenge in the discretization is that two different meshes are needed, one for the homogenized domain Ω_{hom} and one for the particle domain Ω_r .

The discretization of the domain Ω_{hom} will be done first. Therefore, a mesh $\mathcal{T}_{h,hom}$ is defined on this domain, which can be trivially done, since it is a 1D domain. The only small complication in defining the mesh is that it needs to be defined in such a way that the common point of an electrode and the separator is on the boundary of mesh cells. This needs to be done, since some coefficients of the model equations might be discontinuous between the electrode and separator and since the solution ϕ_s does not exist in the domain of the separator.

Remark 4.1.17. *In the actual implementation in deal.II this is achieved by considering two independent meshes, one for the separator and one for the electrode domain. This also has another advantage, since the coupling to the particle equations is defined only in the electrode domain.*

On this mesh, the finite dimensional subspaces of $H^1(\Omega_{hom})$ and $H^1(\Omega_{el})$ can be defined as

$$\begin{aligned} U_{h,hom} &= \{\varphi \in H^1(\Omega_{hom}) : \varphi \circ \lambda_K \in Q_1, \forall K \in \mathcal{T}_{h,hom}, \varphi = g_D \text{ on } \Gamma_D\}, \\ U_{h,el} &= \{\varphi \in H^1(\Omega_{el}) : \varphi \circ \lambda_K \in Q_1, \forall K \in \mathcal{T}_{h,hom} \text{ with } K \cap \Omega_{el} \neq \emptyset\}. \end{aligned}$$

In this notation λ_K describes the transformation between the unit cell $\widehat{K} = (0, 1)$ and the real cell K . With the help of these spaces, the vector valued space can be defined, in which the discrete solution and discrete test functions will be defined.

$$U_h = U_{h,hom} \times U_{h,hom} \times U_{h,el}.$$

Remark 4.1.18. For simplicity the Dirichlet boundary condition was defined as a function g_D on the boundary Γ_D . But it should be mentioned that, depending on which component of $u = (c_l, \phi_l, \phi_s)$ this space is used, both g_D and Γ_D might have a different definition. Even further, in this section the same notation for the test and solution space will be used, since the only difference is the Dirichlet condition, which is always homogeneous for the test space.

With this notation and definition, the discrete problem on the homogenized domain Ω_{hom} can be formulated.

Problem 4.1.19. Let's assume, the functions $v^m \in L^2(\Omega_{el}, H_r^1(\Omega_r))^{N_R}$ are given for $m = 1, \dots, N_t$. Find the solution $u_h^m \in U_h$ for $i = 1, \dots, N_t$, such that the equations

$$\begin{aligned} (u_h^m - u_h^{m-1}, \varphi) &= k_m A(u_h^m, v^m)(\varphi) & \forall \varphi_h \in U_h, \\ u_h^0 &= (c_{l,0}, 0, 0), \end{aligned}$$

hold true.

Discretization of the active material domain

At the current state, the model is discretized in time and in space only in the domain Ω_{hom} . The next and final step for the discretization is to discretize the domain Ω_r .

As was done several times now, a mesh $\mathcal{T}_{h,r}$ of the domain $\Omega_r = (0, 1)$ is defined. On this mesh the finite dimensional subspace of $V_h \subset H_r^1(\Omega_r)$

$$V_h = \{\psi \in H_r^1(\Omega_r) : \psi \circ \lambda_K \in Q_1, \forall K \in \mathcal{T}_{h,r}\}$$

are defined. Although the continuous function v is defined in both domains $\Omega_{el} \times \Omega_r$ and therefore can be interpreted as a function in two dimensions, the differential operator in the equation (4.15) only is defined in the direction of Ω_r . Therefore, only the direction Ω_r is discretized, but not the direction Ω_{el} . Now the discretized problem of the model in the particle domain can be defined.

Problem 4.1.20. Let's assume, the functions $u^m \in U$ are given for $m = 1, \dots, N_t$. Find the solution $v_h^m \in L^2(\Omega_{el}, V_h)$ for $m = 1, \dots, N_t$, such that the equations

$$\begin{aligned} \int_{\Omega_{el}} (v_h^m - v_h^{m-1}, \psi_h)_r dx &= \int_{\Omega_{el}} k_m B_x(u^m, v_h^m)(\psi_h) dx & \forall \psi_h \in L^2(\Omega_{el}, V_h), \\ v_h^0 &= c_{s,0}, \end{aligned}$$

hold true.

Then the partially discretized problem is given by combining problem 4.1.19 and problem 4.1.20.

Problem 4.1.21 (Partially discretized model). *For $m = 1, \dots, N_t$, find the solutions $u_h^m \in U_h$ and $v_h^m \in L^2(\Omega_{el}), V_h$, such that the equations*

$$(u_h^m - u_h^{m-1}, \varphi_h) = k_m A(u_h^m, v_h^m)(\varphi_h) \quad \forall \varphi_h \in U_h, \quad (4.16)$$

$$\int_{\Omega_{el}} (v_h^m - v_h^{m-1}, \psi_h)_r dx = \int_{\Omega_{el}} k_m B_x(u_h^m, v_h^m)(\psi_h) dx \quad \forall \psi_h \in L^2(\Omega_{el}, V_h), \quad (4.17)$$

$$(u_h^0 - (c_{l,0}, 0, 0), \varphi_h) = 0, \quad (4.18)$$

$$(v_h^0 - c_{s,0}, \psi_h)_r = 0, \quad (4.19)$$

hold true.

Remark 4.1.22. *In literature [25], [30], one often finds the discretized version of the LIB model written in a different form. The concentration equation in the particles are not defined with an integral over Ω_{el} , but point wise for a finite set of points $x \in \Omega_{el}$. This finite set is mostly defined as the vertices of the mesh cells in Ω_{el} . To define the coupling term q_{ct} the boundary values $c_s(x, r = 1)$ are interpolated linearly.*

This formulation can be achieved by approximation the integral over Ω_{el} in (4.17) by a trapezoidal rule and using a piecewise linear interpolation of v_h in x -direction. By doing this and choosing $\psi \in L^2(\Omega_{el}, V_h)$ appropriately, this equations can be subdivided in a finite number of equations. It should be mentioned that the weights w_q of the trapezoidal rule can be canceled out, since equation (4.17) has the form

$$w_q (v_h^m(x_q) - v_h^{m-1}(x_q), \psi_h(x_q))_r = w_q B_{x_q}(u_h^m(x_q), v_h^m(x_q))(\psi(x_q))$$

for $q = 1, \dots, N_{quad}$ by this procedure.

N_{quad} describes the number of quadrature points, which coincides with the number of vertices in the case of the trapezoidal rule. To simplify the notation, the subscript q will be used to indicate an evaluation in the quadrature point x_q , for example $v_{h,q}^m := v_h^m(x_q)$.

Problem 4.1.23 (Fully discretized model). *For $m = 1, \dots, N_t$, find the solutions $u_h^m \in U_h$ and $v_h^m \in L^2(\Omega_{el}), V_h$, such that the equations*

$$(u_h^m - u_h^{m-1}, \varphi_h) = k_m A(u_h^m, v_h^m)(\varphi_h) \quad \forall \varphi_h \in U_h, \quad (4.20)$$

$$(v_{h,q}^m - v_{h,q}^{m-1}, \psi_{h,q})_r = k_m B_{x_q}(u_{h,q}^m, v_{h,q}^m)(\psi_{h,q}) \quad \forall \psi_{h,q} \in V_h, \quad (4.21)$$

$$(u_h^0 - (c_{l,0}, 0, 0), \varphi_h) = 0, \quad (4.22)$$

$$(v_{h,q}^0 - c_{s,0}, \psi_{h,q})_r = 0, \quad (4.23)$$

hold true for all $q = 1, \dots, N_{quad}$.

Due to the non linearity of the equations, Newton's method is applied in every time step to calculate the next solution at the next discretization point in time. Newton's method is applied, since it has quadratic convergence properties, if it converges, in comparison to the slower linear convergence of for example a fixed point iteration. To formulate Newton's method, first the Gâteaux derivative is defined.

Definition 4.1.24 (Gâteaux derivative). *Let X, Y be normed spaces, for an operator*

$$T : X \rightarrow Y \quad (4.24)$$

the Gâteaux derivative is a linear forms $A \in \mathcal{L}(X, Y)$, such that the identity

$$\lim_{\varepsilon \rightarrow 0} \frac{T(x + \varepsilon \delta x) - T(x)}{\varepsilon} = A \delta x \quad (4.25)$$

holds true. For the Gâteaux derivative A , the notation $T'(x) := A$ will be used.

To formulate Newton's method for the LIB model 4.1.23, furthermore the simplified notation

$$\mathcal{A}(u_h^m, v_h^m)(\varphi_h) := (u_h^m - u_h^{m-1}, \varphi_h) - k_m A(u_h^m, v_h^m)(\varphi_h) \quad (4.26)$$

$$\mathcal{B}(u_h^m, v_h^m)(\psi_h) := \left((v_{h,q}^m - v_{h,q}^{m-1}, \psi_{h,q})_r - k_m B_{x_q}(u_{h,q}^m, v_{h,q}^m)(\psi_{h,q}) \right)_{q=1}^{N_{quad}}, \quad (4.27)$$

is used.

Therefore, the wanted solutions (u_h^m, v_h^m) in the time interval $I_m = (t_{m-1}, t_m]$ is given by the root of the semilinear forms \mathcal{A} and \mathcal{B} , which are calculated using Newton's method.

Problem 4.1.25. *For given functions (u_h^{m-1}, v_h^{m-1}) the root of the forms \mathcal{A} and \mathcal{B} can be iteratively calculated by the following scheme.*

(1) Set a guess solution $(U_0, V_0) = (u_h^{m-1}, v_h^{m-1})$.

(2) Set $i=0$.

(3) Solve the linear system

$$\begin{pmatrix} \mathcal{A}'_u(U_i, V_i) & \mathcal{A}'_v(U_i, V_i) \\ \mathcal{B}'_u(U_i, V_i) & \mathcal{B}'_v(U_i, V_i) \end{pmatrix} \begin{pmatrix} \delta U \\ \delta V \end{pmatrix} = \begin{pmatrix} -\mathcal{A}(U_i, V_i) \\ -\mathcal{B}(U_i, V_i) \end{pmatrix} \quad (4.28)$$

(4) Update the solutions

$$U_{i+1} = U_i + \delta U \quad (4.29)$$

$$V_{i+1} = V_i + \delta V \quad (4.30)$$

(5) Set $i = i + 1$.

(6) Go to step (3) until a specific tolerance

$$\|(\mathcal{A}(U_i, V_i), \mathcal{B}(U_i, V_i))\| \leq TOL$$

is fulfilled.

(7) Define the solution

$$(u_h^m, v_h^m) := (U_i, V_i).$$

Remark 4.1.26. *It should be mentioned, that the matrix in step (3) of problem 4.1.25 won't be very large in general. It will be shown later that a coarse refinement of the meshes $\mathcal{T}_{h,hom}$ and $\mathcal{T}_{h,r}$ is enough to get a small error in the wanted goal functional. Therefore, the number of degrees of freedom will be less than 2000 in most cases, resulting in a small matrix. For such a small matrix a direct solver for sparse matrices will be used.*

4.1.3 Cathode half cell

All numerical tests done in the following will be done for a specific half cell, consisting of a cathode and half a separator. The half cell has a total length of $\Omega_{hom} = (0, 125\mu m)$, where the cathode part has a length of $\Omega_{el} = (0, 75\mu m)$. In table 4.1 the parameter of this cathode are summarized, table 4.3 shows the used parameter set for the separator. The OCV curve of the cathode is depicted in figure 4.1, where the potential is fixed by measuring the potential against the lithium potential. The active material in the cathode is reconstructed by a distribution of spheres with $N_R = 10$ different radii as shown in table 4.2.

Furthermore, all tests will be done for a 1C and a 10C discharge rate. This notation means that the charge current density j_L is chosen such that the battery is fully discharged in 1 hour and 0.1 hours, respectively.

The charge current density is there calculated for a x C discharge rate by the formula

$$j_L = Fc_{s,max}(1 - \varepsilon_l)L\frac{x}{3600}, \quad (4.31)$$

Parameter	Value
D_l^{eff}	$1.584 \cdot 10^{-10} \frac{m^2}{s}$
D_s	$10^{-14} \frac{m^2}{s}$
σ_l^{eff}	$0.287 \frac{S}{m}$
σ_s^{eff}	$100 \frac{S}{m}$
$(1 + \frac{\log(f_{\pm})}{\log(c_l)})$	1
t_+	0.305
a_{spec}	$0.25 \cdot 10^6 m^{-1}$
ε_l	0.551
k	$4.26 \cdot 10^{-9}$
$c_{s,max}$	$49140 \frac{mol}{m^3}$
α	0.5
$c_{l,0}$	$1000 \frac{mol}{m^3}$
T	298K

Table 4.1: Cathode parameters.

which can be derived both from a physical point of view and based on the model equations of the P2D model.

To derive this formula from a physical point of view, the charge transfer inside the LIB has to be considered. The electrical charge Q flowing in a time period $(0, t)$ can be directly computed with the current density j_L

$$Q = j_L \cdot A \cdot t, \quad (4.32)$$

where A is the interface between the electrode and the current collector. Since for every electron entering the cathode a once positively charged lithium ion is intercalated in the active material, the same current can be calculated using the mean value of lithium concentration \hat{c}_s in the active material. Here it is assumed that at the beginning of the discharge cycle the mean value is zero.

$$Q = F \cdot \hat{c}_s \cdot V = F \hat{c}_s AL(1 - \varepsilon_l). \quad (4.33)$$

In this equation the Faraday constant was used to convert the number of lithium ions to an electrical charge. Furthermore, the volume $V = AL(1 - \varepsilon_l)$ of the active material was used, the volume $A \cdot L$ is the volume of the complete electrode, consisting of active material and electrolyte. Since ε_l is the porosity or volume fraction of the electrolyte, $(1 - \varepsilon_l)$ is the volume fraction of the active material. For a x C discharge rate, the mean value of the concentration reaches the maximal concentration $c_{s,max}$ after a time of $t = \frac{3600}{x}$ seconds, which then shows equation (4.31).

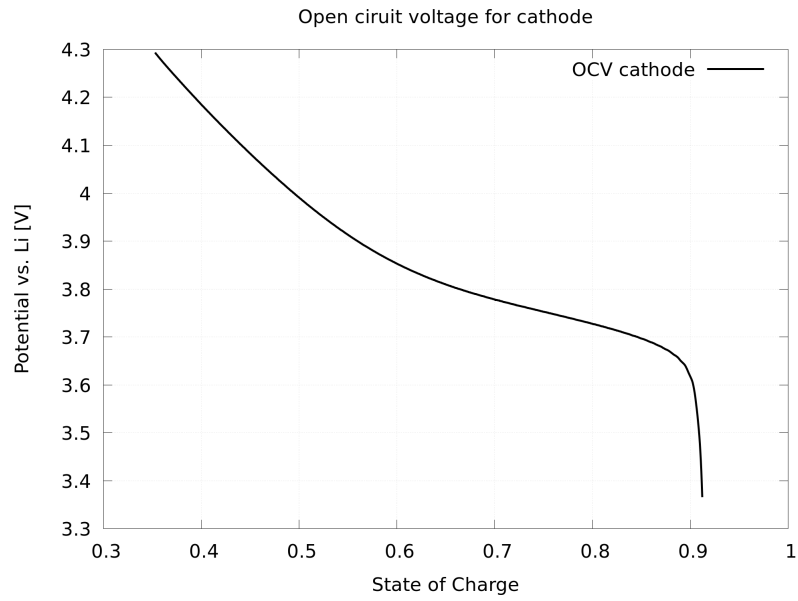


Figure 4.1: Open circuit voltage for the cathode.

Radius R_i [μm]	Volume fraction vol_i
0.5	$1.2629 \cdot 10^{-5}$
1.5	$1.0785 \cdot 10^{-2}$
2.5	0.10832
3.5	0.22374
4.5	0.25752
5.5	0.17132
6.5	0.11131
7.5	$6.0887 \cdot 10^{-2}$
8.5	$3.9307 \cdot 10^{-2}$
9.5	$1.6798 \cdot 10^{-2}$

Table 4.2: Distribution of spheres to reconstruct the active material in the cathode.

Parameter	Value
D_l^{eff}	$1.54 \cdot 10^{-10} \frac{m^2}{s}$
σ_l^{eff}	$0.279 \frac{S}{m}$
$(1 + \frac{\log(f_{\pm})}{\log(c_l)})$	1
t_+	0.305
ε_l	0.551
$c_{l,0}$	$1000 \frac{mol}{m^3}$

Table 4.3: Separator parameters.

To derive this formula from the model equations, a similar approach is used. The mean value of the lithium concentration in the active material is given by

$$\hat{c}_s = \frac{1}{|\Omega_{el}|} \int_{\Omega_{el}} \sum_{i=1}^{N_R} vol_i \frac{3}{R_i^3} \int_0^{R_i} c_{s,i} r^2 dr dx, \quad (4.34)$$

where the volume fraction vol_i takes into account the number of spheres with radius R_i . Using the model equation (4.4) and integrating the diffusion term with the boundary condition (4.9), the equation

$$\partial_t \hat{c}_s = \frac{1}{\varepsilon_s F} \sum_{i=1}^{N_R} \int_{\Omega_{el}} a_{spec,i} j_{ct,i} dx \quad (4.35)$$

$$= \frac{1}{\varepsilon_s F |\Omega_{el}|} \int_{\Omega_{el}} q_{ct} dx \quad (4.36)$$

is derived.

By integrating equation (4.3) with boundary conditions (4.8),

$$j_L = \int_{\Omega_{el}} q_{ct} dx \quad (4.37)$$

can be shown.

By merging both equations and since all used parameters are independent of time, it can directly be shown that

$$\hat{c}_s = \frac{1}{\varepsilon_s FL} j_L t \quad (4.38)$$

holds true, where $\hat{c}_s(0) = 0$ is assumed. With the same argument as in the physical consideration, formula (4.31) is shown.

4.1.4 Potential of a half cell

As described before in section 2.1.1, the performance of a battery is calculated by the potential difference between cathode and anode. For a half cell, this definition 2.1.1 cannot directly be used, since in this case only one electrode is simulated.

Therefore, for a half cell the potential of the battery will be defined by

Definition 4.1.27 (Potential of a half cell). *Let ϕ_s be electrical potential in the solution of problem 4.1.5 and $x_{cc} \in \partial\Omega_{hom}$ the boundary of the electrode corresponding to the current collector. Then the potential of a half cell is defined as a function*

$$\Phi : T \rightarrow \mathbb{R}, \tag{4.39}$$

$$t \mapsto \phi_s(x_{cc}, t). \tag{4.40}$$

4.2 Condition number of the Jacobian matrix

In this section, the condition number of the Jacobian matrix for the battery model is investigated numerically. Due to the fact that the model is time dependent and several newton steps will be necessary in every time step, many different Jacobi matrices are used during the simulation of the LIB. Therefore, in the following the Jacobi matrices at different points in time and in several newton steps are considered.

The condition number of the Jacobi matrix will be calculated for a half cell, as described in 4.1.3. The meshes are chosen to be 3 times globally refined each, therefore consisting of 8 mesh cells in both separator and cathode and 8 mesh cells in the particle mesh.

Due to this setup the number of degrees of freedom is rather small with only 853 degrees of freedom. Therefore, to investigate the condition number of the matrices, they are written into a file and elaborated with Matlab [40].

Table 4.4 contains the condition number of different points in time and different newton steps, the first and the last. The condition number is calculated with respect to the spectral norm

$$\text{cond}_2(A) = \|A\|_2 \|A^{-1}\|_2. \tag{4.41}$$

It is evident that solving matrices with such large condition number will lead to large errors in the solution process, therefore a preconditioning needs to be

time step m	Newton step	condition number
1	1	$4.49 \cdot 10^{17}$
1	3	$4.49 \cdot 10^{17}$
10	1	$4.49 \cdot 10^{17}$
10	3	$4.49 \cdot 10^{17}$
100	1	$4.49 \cdot 10^{17}$
100	3	$4.49 \cdot 10^{17}$

Table 4.4: Condition number of a half cell at different points in time and for different newton steps.

applied in order to reduce the errors. Considering the structure of the matrix, to be more precise, the structure of the model equations, it can be observed that the homogenized equations and the particle equations deal with integration domains of very different size. The homogenized equations are integrated on the domain Ω_{hom} , which has a size of $|\Omega_{hom}| = 125\mu m$. The particle equation is integrated on the domain $\Omega_{el} \times \Omega_r$ and therefore the integration domain is of size $|\Omega_{el} \times \Omega_r| \approx 75\mu m \cdot 10\mu m$. This means that the integration domain of the particles is about 5 – 6 orders of magnitude smaller than the homogenized domain.

This large difference in size can lead to a bad conditioning of the Jacobi matrix, but could be reduced by a very simple preconditioning, the left sided scaling of the matrix.

$$Ax = b \tag{4.42}$$

$$\iff D^{-1}Ax = D^{-1}b, \tag{4.43}$$

with the diagonal matrix $D = \text{diag}(A)$.

Remark 4.2.1. *Beside the left sided scaling of the matrix, also a both sided scaling and a right sided scaling is considered.*

$$\begin{aligned} Ax &= b \\ \iff D^{-0.5}AD^{-0.5}y &= D^{-0.5}b && \text{with } x = D^{-0.5}y \\ \iff AD^{-1}y &= b && \text{with } x = D^{-1}y \end{aligned}$$

This consideration are anticipatory, since in the next section 4.3, an a posteriori error estimation of the LIB model will be investigated. For this error estimation linear equation systems with the transposed matrix of the Jacobi matrix need to be solved for the dual problem. The both sided scaling and the right sided scaling are therefore investigated to also determine the best preconditioning for the dual problem.

m	Newton step	$\text{cond}(D^{-1}A)$	$\text{cond}(D^{-0.5}AD^{-0.5})$	$\text{cond}(AD^{-1})$
1	1	$5.84 \cdot 10^4$	$3.09 \cdot 10^{10}$	$5.51 \cdot 10^{23}$
1	3	$5.75 \cdot 10^4$	$3.39 \cdot 10^{10}$	$6.32 \cdot 10^{23}$
10	1	$5.79 \cdot 10^4$	$3.31 \cdot 10^{10}$	$5.93 \cdot 10^{23}$
10	3	$5.78 \cdot 10^4$	$3.11 \cdot 10^{10}$	$5.58 \cdot 10^{23}$
100	1	$5.78 \cdot 10^4$	$2.85 \cdot 10^{10}$	$4.94 \cdot 10^{23}$
100	3	$5.76 \cdot 10^4$	$2.63 \cdot 10^{10}$	$4.77 \cdot 10^{23}$

Table 4.5: Condition number of a half cell at different time steps m and for different newton steps.

In table 4.5 the condition number for all three scaling procedures are shown for the same cases as before.

It is evident that the left sided scaling of the Jacobian matrix is the way to go, since the condition number in this case is several orders of magnitude smaller than in the other cases.

It should also be mentioned that a right sided scaling of the Jacobian matrix worsens the condition number. This result will later be important in the section 4.3.

4.3 A posteriori error estimate and mesh adaptivity

Just like it was done in the case of the calculation of the effective parameter, error estimators for the battery model will be derived. The goal here is to use the error estimators as indicators to locally refine the mesh where needed, while still maintaining a reasonable error tolerance to reduce simulation time. The derivation of the error estimators will be more complicated in this case than in the case of the effective parameter, since the model is non linear.

As mentioned before, the derivations that will be done now are easier, if the time discretization is done with a Galerkin method. Therefore, the first step in this section is to reformulate problem 4.1.23 as a Galerkin method in space and time. Since the implicit Euler method is equivalent to a discontinuous Galerkin method (dG) of order 0, the reformulation will be done for a dG method of order r in time. The first step is to define the discrete function spaces

$$\begin{aligned}
 U_h^r &:= \{\varphi \in L^2(T, U_h) : \varphi|_{T_m} \in \mathcal{P}_r(T_m, U_h), \text{ for } T_m \in \mathcal{T}_k\}, \\
 V_h^r &:= \{\psi \in L^2(T, L^2(\Omega_{el}, V_h)) : \varphi|_{T_m} \in \mathcal{P}_r(T_m, L^2(\Omega_{el}, V_h)), \text{ for } T_m \in \mathcal{T}_k\},
 \end{aligned}$$

where \mathcal{P}_r is the space of polynomials with degree r .

With these spaces, the discrete problem can be reformulated.

Problem 4.3.1 (Discrete problem with space time Galerkin method). *Find the solutions $u_h \in U_h^r$ and $v_h \in V_h^r$, such that the equations*

$$\begin{aligned} & \sum_{m=1}^{N_t} \int_{T_m} (\partial_t u_h, \varphi_h) + A(u_h, v_h)(\varphi) dt \\ & + \sum_{m=0}^{N_t-1} \left([u_h]_m, \varphi_{h,m}^+ \right) + \left(u_{h,0}^-, \varphi_{h,0}^- \right) = \left(u^0, \varphi_{h,m}^- \right), \\ & \sum_{q=1}^{N_{quad}} w_q \left[\sum_{m=1}^{N_t} \int_{T_m} (\partial_t v_{h,q}, \psi_{h,q})_r + B_{x_q}(u_{h,q}, v_{h,q})(\psi_{h,q}) dt \right. \\ & \left. + \sum_{m=0}^{N_t-1} \left([v_{h,q}]_m, \psi_{h,q,m}^+ \right)_r + \left(v_{h,q,0}^-, \psi_{h,q,0}^- \right)_r \right] = \sum_{q=1}^{N_{quad}} w_q \left(v^0, \psi_{h,q,m}^- \right)_r \end{aligned}$$

hold true for all $\varphi \in U_h^r$ and $\psi \in V_h^r$.

Remark 4.3.2. *In this formulation the following notation was used:*

$$\begin{aligned} \varphi_{h,m}^\pm & := \lim_{\varepsilon \downarrow 0} \varphi_h(t_m \pm \varepsilon), \\ [\varphi_h]_m & := \varphi_{h,m}^+ - \varphi_{h,m}^-. \end{aligned}$$

Furthermore, if $r = 0$ is chosen and the time integration is done with a right sided box rule, it is obvious that this method is equivalent to the implicit Euler method.

To derive the error estimators basically the same approach as before is used. A dual problem for a specific goal functional will be defined and the error estimators will be derived with the help of this dual problem. For nonlinear problems the dual problem cannot be stated directly, but needs to be calculated with the help of a Lagrangian formalism. For further details on this topic again the book of Bangerth and Rannacher [4] and also the publication of Vexler and Schmich [46] is referred. But the derivation will be done in details here in a similar way.

To derive error estimators with the dual weighted residual (DWR) method, the standard approach with a Lagrangian formalism is used. Before defining the Lagrangian functional, the goal functional, for which the error should be estimated, needs to be defined. The goal of our model is to calculate potential curves, describing the charge and discharge behaviour of the LIB. Therefore, the natural choice is to measure the error in terms of this potential curve, like defined in definition 4.1.27.

Definition 4.3.3. *For a solution $(u, v) \in U \times V$, where $u = (c_l, \phi_l, \phi_s)$ of problem 4.1.5, the goal functional is defined as the potential ϕ_s measured at the*

intersection between cathode and current collector

$$J : U \times V \rightarrow \mathbb{R}, \quad (4.44)$$

$$J(u, v) = \int_T \phi_s(x_{cc}, t) dt, \quad (4.45)$$

where x_{cc} is defined like in definition 4.1.27.

Now the Lagrangian functional can be defined.

Definition 4.3.4 (Lagrangian functional).

$$\begin{aligned} \mathcal{L} : U \times V \times U \times V &\rightarrow \mathbb{R}, \\ \mathcal{L}(u, v, z_u, z_v) &= J(u, v) - \sum_{m=1}^{N_t} \int_{T_m} (\partial_t u, z_u) - A(u, v)(z_u) dt \\ &\quad - \sum_{m=0}^{N_t-1} \left([u]_m, z_{u,m}^+ \right) + \left(u_0^- - u^0, z_{u,0}^- \right) \\ &\quad - \sum_{m=1}^{N_t} \int_{T_m} \int_{\Omega_{el}} (\partial_t v, z_v)_r + B_x(u, v)(z_v) dx dt \\ &\quad - \sum_{m=0}^{N_t-1} \int_{\Omega_{el}} \left([v]_m, z_{v,m}^+ \right)_r + \left(v_0^- - v^0, z_{v,0}^- \right)_r dx. \end{aligned}$$

Remark 4.3.5. *The Lagrangian functional was here defined for functions in the space $U \times V \times U \times V$ and since these functions are continuous in time, the jump terms $[u]_m$ and $[v]_m$ vanish. Later in the derivation of the error estimators, the discrete functions will be applied to this functionals. In this case, the jump terms won't vanish, therefore the definition here was done with these terms.*

By standard means, therefore the dual problem can be defined, by calculating the derivative of the Lagrangian with respect to the primal variables u, v

Problem 4.3.6 (Dual problem). *For given functions $(u, v) \in U \times V$, find the solution $z_u \in U$ and $z_v \in V$, such that the equations*

$$\begin{aligned} \int_T -(\partial_t z_u, \varphi) + A'_u(u, v)(z_u, \varphi) + \int_{\Omega_{el}} B'_{x,u}(u, v)(z_v, \varphi) dx dt \\ + \left(z_{u, N_R}^+, \varphi_{N_R}^+ \right) &= J'_u(u, v)(\varphi), \\ \int_T \int_{\Omega_{el}} -(\partial_t z_v, \psi)_r + B'_{x,v}(u, v)(z_v, \psi) dx + A'_v(u, v)(z_u, \psi) dt \\ + \left(z_{v, N_R}^+, \psi_{N_R}^+ \right)_r &= J'_v(u, v)(\psi), \end{aligned}$$

hold true for all $\varphi \in U$ and $\psi \in V$.

The negative sign in the term with time derivatives is a result of a partial integration in time.

If the simplified notation with the forms A and B_x were not used, the dual equations would read like follows:

$$\begin{aligned}
 & \int_T -(\partial_t z_{c_l}, \varphi) + (D\partial_x z_{c_l}, \partial_x \varphi) - \frac{1-t_+}{F} (z_{c_l}, q'_{ct,c_l}(\varphi)) - (z_{\phi_l}, q'_{ct,c_l}(\varphi)) \\
 & + \left(\frac{2RT}{F} \sigma_s (1-t_+) \left(1 + \frac{\partial \log f_{\pm}}{\partial x} \right) \left(\frac{1}{c_l} \partial_x \varphi - \frac{\partial_x c_l}{c_l^2} \varphi \right), \partial_x z_{\phi_l} \right) \\
 & + (z_{\phi_s}, q'_{ct,c_l}(\varphi)) - \int_{\Omega_{el}} \sum_{i=1}^{N_R} \frac{R_i^3 a_{spec,i}}{3\varepsilon_s vol_i} j'_{ct,i,c_l}(\varphi) z_{c_s,i} dx dt \\
 & + (z_{c_l}(t_{end}), \varphi(t_{end})) = J'_{c_l}(u, v)(\varphi), \\
 & \int_T (\sigma_l \partial_x z_{\phi_l}, \partial_x \varphi) - \frac{1-t_+}{F} (z_{c_l}, q'_{ct,\phi_l}(\varphi)) - (z_{\phi_l}, q'_{ct,\phi_l}(\varphi)) + (z_{\phi_s}, q'_{ct,\phi_l}(\varphi)) \\
 & - \int_{\Omega_{el}} \sum_{i=1}^{N_R} \frac{R_i^3 a_{spec,i}}{3\varepsilon_s vol_i} j'_{ct,i,\phi_l}(\varphi) z_{c_s,i} dx dt = J'_{\phi_l}(u, v)(\varphi), \\
 & \int_T (\sigma_s \partial_x z_{\phi_s}, \partial_x \varphi) - \frac{1-t_+}{F} (z_{c_l}, q'_{ct,\phi_s}(\varphi)) - (z_{\phi_l}, q'_{ct,\phi_s}(\varphi)) + (z_{\phi_s}, q'_{ct,\phi_s}(\varphi)) \\
 & - \int_{\Omega_{el}} \sum_{i=1}^{N_R} \frac{R_i^3 a_{spec,i}}{3\varepsilon_s vol_i} j'_{ct,i,\phi_s}(\varphi) z_{c_s,i} dx dt = J'_{\phi_s}(u, v)(\varphi).
 \end{aligned}$$

The dual solution for the particle equations are defined for $i = 1, \dots, N_R$ by

$$\begin{aligned}
 & \int_T \int_{\Omega_{el}} -(\partial_t z_{c_s,i}, \psi)_r + (D_s \partial_r z_{c_s,i}, \partial_r \psi)_r - \frac{R_i^3 a_{spec,i}}{3\varepsilon_s vol_i} j'_{ct,i,c_s,i} z_{c_s,i} dx \\
 & - \frac{1-t_+}{F} (z_{c_l}, a_{spec,i} j'_{ct,i,c_s,i}(\psi)) - (z_{\phi_l}, a_{spec,i} j'_{ct,i,c_s,i}(\psi)) \\
 & + (z_{\phi_s}, a_{spec,i} j'_{ct,i,c_s,i}(\psi)) dt = J'_{c_s,i}(u, v)(\psi).
 \end{aligned}$$

As one can see, the time derivative has a negative sign and instead of a start solution at time $t = 0$, due to the equations, a final solution at time $t = t_{end}$ is given, which means that this problem needs to be solved backwards in time.

Remark 4.3.7. *The integration by parts in time is only allowed for the continuous solutions. In the derivation of the error estimators, the discrete solutions will be applied to the derivative \mathcal{L}'_u . In this case the integration by parts is not possible in the whole time domain T , but only piecewise in the time cells T_m . Therefore, the integration by parts was done here only to show that the solution process is done backwards in time. For the upcoming derivations, this step will not be done.*

Discretizing the dual problem with a $dG(0)$ method in time will therefore result in the following problem

Problem 4.3.8 (Semidiscrete dual problem). *For given functions $(u, v) \in U^r \times V^r$, find the solution $z_u \in U^r$ and $z_v \in V^r$, such that the equations*

$$\begin{aligned} & \sum_{m=1}^{N_t} \int_{T_m} A'_u(u^m, v^m)(z_u, \varphi^m) + \int_{\Omega_{el}} B'_{x,u}(u^m, v^m)(z_v, \varphi^m) dx dt \\ & + \sum_{m=0}^{N_t-1} \left([\varphi]_m, z_{u,m}^+ \right) + \left(\varphi_0^-, z_{u,0}^- \right) = J'_u(u, v)(\varphi), \\ & \sum_{m=1}^{N_t} \int_{T_m} A'_v(u^m, v^m)(z_u, \psi^m) + \int_{\Omega_{el}} B'_{x,v}(u^m, v^m)(z_v, \psi^m) dx dt \\ & + \sum_{m=0}^{N_t-1} \int_{\Omega_{el}} \left([\psi]_m, z_{v,m}^+ \right)_r + \left(\psi_0^-, z_{v,0}^- \right)_r dx = J'_v(u, v)(\psi), \end{aligned}$$

hold true for all $\varphi \in U^r$ and $\psi \in V^r$.

In this problem the semi discrete spaces

$$\begin{aligned} U^r & := \{ \varphi \in L^2(T, U) : \varphi|_{T_m} \in \mathcal{P}_r(T_m, U), \text{ for } T_m \in \mathcal{T}_k \}, \\ V^r & := \{ \psi \in L^2(T, L^2(\Omega_{el}, V)) : \psi|_{T_m} \in \mathcal{P}_r(T_m, L^2(\Omega_{el}, V)), \text{ for } T_m \in \mathcal{T}_k \}, \end{aligned}$$

are used.

Since the functions in the space U^r and V^r are discontinuous in time and using $r = 0$, test function φ and ψ can be chosen, such that it is nonzero only in the interval T_m for $m \neq 0$ and resulting in the equations

$$\begin{aligned} & \int_{T_m} A'_u(u^m, v^m)(z_u, \varphi^m) + \int_{\Omega_{el}} B'_{x,u}(u^m, v^m)(z_v, \varphi^m) dx dt \\ & + \left(\varphi_m^-, z_{u,m-1}^+ - z_{u,m}^+ \right) = J'_u(u, v)(\varphi), \\ & \int_{T_m} A'_v(u^m, v^m)(z_u, \psi^m) + \int_{\Omega_{el}} B'_{x,v}(u^m, v^m)(z_v, \psi^m) dx dt \\ & + \int_{\Omega_{el}} \left(\psi_m^-, z_{v,m-1}^+ - z_{v,m}^+ \right)_r dx = J'_v(u, v)(\psi), \end{aligned}$$

where $z_{u,N_t}^+ = 0$ and $z_{v,N_t}^+ = 0$. In the case $m = 0$ the equations have the form

$$\begin{aligned} & \left(\varphi_0^-, z_{u,0}^- - z_{u,0}^+ \right) = 0, \\ & \int_{\Omega_{el}} \left(\psi_0^-, z_{v,0}^- - z_{v,0}^+ \right)_r dx = 0. \end{aligned}$$

Due to the definition of U^r and V^r with $r = 0$, as sets of piecewise constant functions, the superscript \pm can be skipped with

$$\begin{aligned} u_m^+ &= u_{m+1}^- = u^{m+1}, \\ v_m^+ &= v_{m+1}^- = v^{m+1}, \\ z_{u,m+1}^- &= z_{u,m}^+ = z_u^m, \\ z_{v,m+1}^- &= z_{v,m}^+ = z_v^m. \end{aligned}$$

The equation for $m \neq 0$ show that the solution $z_{N_t} = 0$ is given in the end point $t = t_{end}$, and therefore the problem is solved backward in time.

Since a implicit method should be used for stability reasons, this means that in the case of the dual equation, the time integral is replaced by a left side box rule (in comparison to the primal solution, where a right side box rule was used).

The specifics of the discretization in space for the dual problem will not be given, since this discretization works in the same way as for the primal solution.

As it was mentioned before, the integration over Ω_{el} is not done exactly in the simulations, but approximated by a cell-wise trapezoidal rule. Now the discrete dual problem can be formulated

Problem 4.3.9 (Discrete dual problem). *For given functions $(u_h, v_h) \in U_h^0 \times V_h^0$, find the solution $z_{u,h} \in U_h^0$ and $z_{v,h} \in V_h^0$, such that the equations*

$$J'_u(u_h, v_h)(\varphi_h) = \left(\varphi_h^m, z_{u,h}^{m-1} - z_{u,h}^m \right) + k_m A'_u(u^m, v^m)(z_u^{m-1}, \varphi_h^m) \quad (4.46)$$

$$+ k_m \sum_{q=1}^{N_{quad}} w_q B'_{x_q, u}(u_{h,q}^m, v_{h,q}^m)(z_{v,h,q}^{m-1}, \varphi_{h,q}^m), \quad (4.47)$$

$$J'_v(u_h, v_h)(\psi_h) = \sum_{q=0}^{N_{quad}} w_q \left(\psi_{h,q}^m, z_{v,h,q}^{m-1} - z_{v,h,q}^m \right)_r \quad (4.48)$$

$$+ k_m A'_v(u^m, v^m)(z_u^{m-1}, \psi_h^m) \quad (4.49)$$

$$+ k_m \sum_{q=1}^{N_{quad}} w_q B'_{x_q, v}(u_{h,q}^m, v_{h,q}^m)(z_{v,h,q}^{m-1}, \psi_{h,q}^m), \quad (4.50)$$

hold true for all $\varphi \in U_h^0$, $\psi_h \in V_h^0$ and for $m = 1, \dots, N_t$.

Remark 4.3.10. *The discrete primal problem 4.1.23 is solved with the help of Newton's method, like described in problem 4.1.25, which needs the Jacobian matrix of the primal problem in step (3). A comparison of this step with the discrete dual problem 4.3.9 shows that the discrete Jacobian matrices for both problems are the same, but transposed. This is important due to the results on the condition number shown in table 4.5. For the primal problem this table shows*

that a left sided scaling of the primal Jacobian matrix improves the condition number significantly. A left sided scaling of the dual Jacobian matrix leads to the transpose of the right scaled primal Jacobian matrix, which is very badly conditioned, as shown in table 4.5.

Therefore, in order to improve the condition number of the dual Jacobian matrix, a right sided scaling needs to be applied, since this corresponds to the left sided scaling of the primal matrix.

The last definition, before deriving the error estimators, is the definition of a discrete Lagrangian functional. The only difference in this definition in comparison with 4.3.4 is that the integration on the domain Ω_{el} will here be done with the trapezoidal rule.

Definition 4.3.11 (Discrete Lagrangian functional).

$$\begin{aligned} \mathcal{L}_h : U_h^0 \times V_h^0 \times U_h^0 \times V_h^0 &\rightarrow \mathbb{R}, \\ \mathcal{L}_h(u_h, v_h, z_{u,h}, z_{v,h}) &= J(u_h, v_h) - \sum_{m=1}^{N_t} \int_{T_m} (\partial_t u_h, z_{u,h}) - A(u_h, v_h)(z_{u,h}) dt \\ &\quad - \sum_{m=0}^{N_t-1} \left([u_h]_m, z_{u,h,m}^+ \right) + \left(u_{h,0}^- - u^0, z_{u,h,0}^- \right) \\ &\quad - \sum_{m=1}^{N_t} \int_{T_m} \sum_{q=1}^{N_{quad}} w_q (\partial_t v_{h,q}, z_{v,h,q})_r + B_{x_q}(u_h, v_{h,q})(z_{v,h,q}) dt \\ &\quad - \sum_{m=0}^{N_t-1} \sum_{q=0}^{N_{quad}} w_q \left([v_{h,q}]_m, z_{v,h,q,m}^+ \right)_r + \left(v_{h,q,0}^- - v^0, z_{v,h,q,0}^- \right)_r. \end{aligned}$$

Theorem 4.3.12. For the solutions $(u, v) \in U \times V$, $(z_u, z_v) \in U \times V$ and $(u_h, v_h) \in U_h \times V_h$, $(z_{u,h}, z_{v,h}) \in U_h \times V_h$ of problems 4.1.5, 4.1.23, 4.3.6 and 4.3.9, the error identity is given by

$$J(u, v) - J(u_h, v_h) = \frac{1}{2}(\rho + \rho^*) + e_q + \mathcal{R}_h + \eta_k,$$

with a remainder term \mathcal{R}_h , a temporal error η_k , a quadrature error

$$\begin{aligned} e_q &= - \sum_{m=1}^{N_t} \int_{T_m} \int_{\Omega_{el}} B_x(u_h, v_h)(z_{v,h}) dx dt \\ &\quad - \sum_{m=0}^{N_t-1} \int_{\Omega_{el}} \left([v_h]_m, z_{2,h,m}^+ \right)_r + \left(v_{h,0}^- - v^0, z_{2,h,0}^- \right)_r dx, \end{aligned}$$

the weighted primal residual

$$\begin{aligned} \rho &= \sum_{m=1}^{N_t} \int_{T_m} A(u_h^m, v_h^m)(z_u^{m-1} - z_{u,h}^{m-1}) + \int_{\Omega_{el}} B_x(u_h^m, v_h^m)(z_v^{m-1} - z_{v,h}^{m-1}) dx dt \\ &+ \sum_{m=1}^{N_t} (u_h^m - u_h^{m-1}, z_u^{m-1} - z_{u,h}^{m-1}) + (u_h^0 - u^0, z_u^0 - z_{u,h}^0) \\ &+ \sum_{m=1}^{N_t} \int_{\Omega_{el}} (v_h^m - v_h^{m-1}, z_v^{m-1} - z_{v,h}^{m-1}) + (v_h^0 - v^0, z_v^0 - z_{v,h}^0) dx, \end{aligned}$$

and the weighted dual residual

$$\begin{aligned} \rho^* &= \sum_{m=1}^{N_t} \int_{T_m} A'_u(u_h^m, v_h^m)(z_{u,h}^{m-1}, u^m - u_h^m) dt \\ &+ \sum_{m=1}^{N_t} \int_{T_m} \int_{\Omega_{el}} B'_{x,u}(u_h^m, v_h^m)(z_{v,h}^{m-1}, u^m - u_h^m) dx dt \\ &+ \sum_{m=1}^{N_t} (u^m - u_h^m, z_{1,h}^m - z_{1,h}^{m-1}) + (u^0, z_{1,h}^0) \\ &+ \sum_{m=1}^{N_t} \int_{T_m} A'_v(u_h^m, v_h^m)(z_{u,h}^{m-1}, v^m - v_h^m) dt \\ &+ \sum_{m=1}^{N_t} \int_{T_m} \int_{\Omega_{el}} B'_{x,v}(u_h^m, v_h^m)(z_{v,h}^{m-1}, v^m - v_h^m) dx dt \\ &+ \sum_{m=1}^{N_t} \int_{\Omega_{el}} (v^m - v_h^m, z_{v,h}^m - z_{v,h}^{m-1})_r + (v^0, z_{v,h}^0)_r. \end{aligned}$$

Proof. In order to prove this identity, first the fact is used, that both the continuous and discrete Lagrangian functionals use the same goal functional J . In the next step the fundamental theorem of calculus is used, where the integration is done with the help of the trapezoidal rule.

But first, the temporal error will be separated, by adding and subtracting the semi discrete solutions u_k and v_k .

$$\begin{aligned} &J(u, v) - J(u_h, v_h) \\ &= J(u, v) - J(u_k, v_k) + J(u_k, v_k) - J(u_h, v_h) \\ &= \eta_k + J(u_k, v_k) - J(u_h, v_h). \end{aligned}$$

The temporal error η_k won't be considered further. For the derivation of error estimators in time the work of Vexler and Schmich, [46] is referred, which can be directly applied to this problem.

Since from this point, only the space error is considered, the subscript k will be skipped from now on and therefore $u = u_k$ and $v = v_k$.

$$J(u, v) - J(u_h, v_h) \quad (4.51)$$

$$= \mathcal{L}(u, v, z_u, z_v) - \mathcal{L}_h(u_h, v_h, z_{u,h}, z_{v,h}) \quad (4.52)$$

$$= \underbrace{\mathcal{L}(u, v, z_u, z_v) - \mathcal{L}(u_h, v_h, z_{u,h}, z_{v,h})}_{(1)} \quad (4.53)$$

$$+ \underbrace{\mathcal{L}(u_h, v_h, z_{u,h}, z_{v,h}) - \mathcal{L}_h(u_h, v_h, z_{u,h}, z_{v,h})}_{(2)} \quad (4.54)$$

First the term marked with (1) will be further investigated.

$$\mathcal{L}(u, v, z_u, z_v) - \mathcal{L}(u_h, v_h, z_{u,h}, z_{v,h}) \quad (4.55)$$

$$= \frac{1}{2} (\mathcal{L}'_u(u_h, v_h, z_{u,h}, z_{v,h})(u - u_h, v - v_h) \quad (4.56)$$

$$+ \mathcal{L}'_z(u_h, v_h, z_{u,h}, z_{v,h})(z_u - z_{u,h}, z_v - z_{v,h})) + \mathcal{R}_h. \quad (4.57)$$

In this step, first the fundamental theorem of calculus was used, and then the integration was done with the trapezoidal rule, which introduced a remainder term \mathcal{R}_h . This remainder term is cubic in the errors $u - u_h$, $v - v_h$, $z_u - z_{u,h}$ and $z_v - z_{v,h}$ and will thus be neglected from now on.

In this equation again, both terms will be further investigated separately.

$$\begin{aligned} & \mathcal{L}'_z(u_h, v_h, z_{u,h}, z_{v,h})(z_u - z_{u,h}, z_v - z_{v,h}) \\ &= \sum_{m=1}^{N_t} \int_{T_m} A(u_h, v_h)(z_u - z_{u,h}) + \int_{\Omega_{el}} B_x(u_h, v_h)(z_v - z_{v,h}) dx dt \\ &+ \sum_{m=0}^{N_t-1} \left([u_h]_m, z_u^m - z_{u,h,m}^+ \right) + \left(u_{h,0}^- - u^0, z_u^0 - z_{u,h,0}^- \right) \\ &+ \sum_{m=0}^{N_t-1} \int_{\Omega_{el}} \left([v_h]_m, z_v^m - z_{v,h,m}^- \right) + \left(v_{h,0}^- - v^0, z_v^0 - z_{v,h}^- \right) dx. \end{aligned}$$

Since a dG(0) method is used with the right side box rule for the primal and left side box rule for the dual equation, the notation can be simplified by using

$$\begin{aligned} u_{h,m}^+ &= u_{h,m+1}^- = u_h^{m+1}, \\ v_{h,m}^+ &= v_{h,m+1}^- = v_h^{m+1}, \\ z_{u,h,m+1}^- &= z_{u,h,m}^+ = z_{u,h}^m, \\ z_{v,h,m+1}^- &= z_{v,h,m}^+ = z_{v,h}^m, \end{aligned}$$

and therefore get

$$\begin{aligned}
& \mathcal{L}'_z(u_h, v_h, z_{u,h}, z_{v,h})(z_u - z_{u,h}, z_v - z_{v,h}) \\
&= \sum_{m=1}^{N_t} \int_{T_m} A(u_h^m, v_h^m)(z_u^{m-1} - z_{u,h}^{m-1}) + \int_{\Omega_{el}} B_x(u_h^m, v_h^m)(z_v^{m-1} - z_{v,h}^{m-1}) dx dt \\
&+ \sum_{m=1}^{N_t} (u_h^m - u_h^{m-1}, z_u^{m-1} - z_{u,h}^{m-1}) + (u_h^0 - u^0, z_u^0 - z_{u,h}^0) \\
&+ \sum_{m=1}^{N_t} \int_{\Omega_{el}} (v_h^m - v_h^{m-1}, z_v^{m-1} - z_{v,h}^{m-1}) + (v_h^0 - v^0, z_v^0 - z_{v,h}^0) dx.
\end{aligned}$$

In a similar fashion, the first term (4.56) is reformulated:

$$\begin{aligned}
& \mathcal{L}'_u(u_h, v_h, z_{u,h}, z_{v,h})(u - u_h, v - v_h) \\
&= \sum_{m=1}^{N_t} \int_{T_m} A'_u(u_h^m, v_h^m)(z_{u,h}^{m-1}, u^m - u_h^m) + \int_{\Omega_{el}} B'_{x,u}(u_h^m, v_h^m)(z_{v,h}^{m-1}, u^m - u_h^m) dx dt \\
&- \sum_{m=1}^{N_t} (u^m - u_h^m, z_{1,h}^m - z_{1,h}^{m-1}) + (u^0, z_{1,h}^0) \\
&+ \sum_{m=1}^{N_t} \int_{T_m} A'_v(u_h^m, v_h^m)(z_{u,h}^{m-1}, v^m - v_h^m) + \int_{\Omega_{el}} B'_{x,v}(u_h^m, v_h^m)(z_{v,h}^{m-1}, v^m - v_h^m) dx dt \\
&- \sum_{m=1}^{N_t} \int_{\Omega_{el}} (v^m - v_h^m, z_{2,h}^m - z_{2,h}^{m-1})_r + (v^0, z_{2,h}^0)_r
\end{aligned}$$

Now the next step is to have a closer look at the terms marked with (2) in (4.54). Comparing definitions 4.3.4 and 4.3.11, it can be seen that the only difference between the continuous and the discrete Lagrangian functional is the quadrature

error by replacing the integration on the domain Ω_{el} by a trapezoidal rule.

$$\begin{aligned}
 & \mathcal{L}(u_h, v_h, z_{u,h}, z_{v,h}) - \mathcal{L}_h(u_h, v_h, z_{u,h}, z_{v,h}) \\
 &= - \sum_{m=1}^{N_t} \int_{T_m} \int_{\Omega_{el}} B_x(u_h^m, v_h^m)(z_{v,h}^{m-1}) dx dt \\
 & \quad - \sum_{m=1}^{N_t} \int_{\Omega_{el}} \left(v_h^m - v_h^{m-1}, z_{v,h}^{m-1} \right)_r + \left(v_h^0 - v^0, z_{v,h}^0 \right)_r dx \\
 & \quad + \sum_{m=1}^{N_t} \int_{T_m} \sum_{q=1}^{N_{quad}} w_q B_{x_q}(u_{h,q}^m, v_{h,q}^m)(z_{v,h,q}^{m-1}) dt \\
 & \quad + \sum_{m=q}^{N_t} \sum_{q=0}^{N_{quad}} w_q \left[\left(v_{h,q}^m - v_{h,q}^{m-1}, z_{v,h,q}^{m-1} \right)_r + \left(v_{h,q}^0 - v^0, z_{v,h,q}^0 \right)_r \right] \\
 &= - \sum_{m=1}^{N_t} \int_{T_m} \int_{\Omega_{el}} B_x(u_h^m, v_h^m)(z_{v,h}^{m-1}) dx dt \\
 & \quad - \sum_{m=1}^{N_t} \int_{\Omega_{el}} \left(v_h^m - v_h^{m-1}, z_{v,h}^{m-1} \right)_r + \left(v_h^0 - v^0, z_{v,h}^0 \right)_r dx,
 \end{aligned}$$

where the time derivatives vanished again since the discrete solution u_h and v_h are piecewise constant in time and the discrete primal equation was used, since $z_{v,h} \in V_h$. This concludes the proof. \square

Remark 4.3.13. *It is also possible to derive error estimators for the time error η_k in parabolic differential equations, as shown in the paper of Vexler and Schmich, [46]. Therefore, this estimation is not further investigated.*

In the proof it can be seen that both residuals and the quadrature error are linear in the errors $u - u_h$, $v - v_h$, $z_u - z_{u,h}$ and $z_v - z_{v,h}$. Therefore, an additional term can be inserted in the residuals and the quadrature error in order to make the error estimator evaluateable. This is not yet the case, since the exact solutions u , v , z_u and z_v would be needed. This step will now be done only for the weighted primal residual, the other error contributions work in the same way.

$$\begin{aligned}
 & \rho(u_h, v_h)(z_u - z_{u,h}, z_v - z_{v,h}) \\
 &= \underbrace{\rho(u_h, v_h)(z_u - \tilde{z}_u, z_v - \tilde{z}_v)}_{(1)} + \underbrace{\rho(u_h, v_h)(\tilde{z}_u - z_{u,h}, \tilde{z}_v - z_{v,h})}_{(2)}.
 \end{aligned}$$

Just as discussed before in the corresponding section 3.5 of the effective parameter chapter, \tilde{z}_u and \tilde{z}_v should be chosen, such that the term marked with (2) dominates over the term (1). Then the term (1) can be neglected in comparison to (2) and the error estimators are evaluateable.

The standard way to define these functions is to derive a patch-wise quadratic interpolation of the linear solutions $z_{u,h}$ and $z_{v,h}$. For the reconstruction of the solution z_u the standard way as described in [4] can be used, but for $z_{v,h}$ some complications occur. The solution $z_{v,h} \in L^2(\Omega_{el}, V_h)$ is not discretized completely. It can be interpreted as a two-dimensional function in the domain $\Omega_{el} \times \Omega_r$, which is discretized only in the direction of Ω_r , but continuous in direction Ω_{el} . As mentioned before in remark 4.1.7 the solution $z_{v,h}$ is not calculated for every $x \in \Omega_{el}$, since this solution is only needed in the quadrature points of the used quadrature formula.

Remark 4.3.14. *In order to evaluate all error contributions, a higher order quadrature rule is used for the integration along Ω_{el} . For a proper reconstruction of the dual solution z_v the discrete solution $z_{v,h}$ would need to be calculated in these new quadrature points. In order to save computational time, these discrete solutions are also calculated with the help of a patch-wise higher order interpolation. Therefore, the dual solution z_v is reconstructed by a patch-wise quadratic interpolation in both direction Ω_{el} and Ω_r .*

4.3.1 Refinement strategy

Beside an estimation of the discretization errors, the error estimators have the purpose to serve as refinement indicators, i. e. the error estimators should determine which cells to refine in order to reduce the error in the most efficient way. Efficiency here means to keep the mesh as coarse as possible, resulting in as few degrees of freedom as possible and therefore a fast solution process.

As described before, the standard way to derive refinement indicators based on the error estimators, is to evaluate the estimators cell-wise and based on a specific strategy refine the cells with the largest error contributions. For the P2D LIB model, this standard way runs into some problems, since this model is not solved on a single mesh, but on different meshes, the mesh for the homogenized domain Ω_{hom} and for every $x \in \Omega_{el} \subset \Omega_{hom}$ and every radius $r = R_1, \dots, R_{N_R}$ a mesh for the particle domain Ω_r . In order to keep the implementation simple, the same mesh $T_{h,r}$ is used for all $x \in \Omega_{hom}$ and all radii. Therefore, the P2D model only has two different meshes.

The error estimators, derived in 4.3.12 consist of the weighted primal residual ρ , the weighted dual residual ρ^* and a quadrature error e_q . The quadrature error measures the error contribution introduced by replacing the integration over Ω_{el} in (4.17) by a trapezoidal rule, thus by replacing the infinite number of particle equations for almost all $x \in \Omega_{el}$, by a finite number of equations in the cell vertices of the mesh $\mathcal{T}_{hom,h}$. Therefore, the quadrature error indicates whether the homogenized mesh $\mathcal{T}_{hom,h}$ is refined enough or not. By evaluating the error

estimators of the residuals cell-wise, there still is no way of concluding, which cell to refine, in order to reduce the error, since particle equations are integrated over the domain Ω_{el} . Therefore, a large error contribution for these equations could indicate that either the particle mesh or the homogenized mesh needs more refinement.

In order to get a better assignment of the error indicators to a mesh, the error estimators will be reformulated.

Lemma 4.3.15. *The weighted primal and dual residuals defined in theorem 4.3.12 can be separated into the discrete weighted primal and dual residuals ρ_h and ρ_h^* and additional quadrature errors ρ_Q and ρ_Q^* .*

$$\begin{aligned}\rho &= \rho_h + \rho_Q, \\ \rho^* &= \rho_h^* + \rho_Q^*,\end{aligned}$$

with

$$\begin{aligned}\rho_h &= \sum_{m=1}^{N_t} \int_{T_m} A(u_h^m, v_h^m)(z_u^{m-1} - z_{u,h}^{m-1}) + \sum_{q=1}^{N_{quad}} w_q B_{x_q}(u_{h,q}^m, v_{h,q}^m)(z_{v,q}^{m-1} - z_{v,h,q}^{m-1}) dt \\ &+ \sum_{m=1}^{N_t} (u_h^m - u_h^{m-1}, z_u^{m-1} - z_{u,h}^{m-1}) + (u_h^0 - u^0, z_u^0 - z_{u,h}^0) \\ &+ \sum_{m=1}^{N_t} \sum_{q=1}^{N_{quad}} w_q \left[(v_{h,q}^m - v_{h,q}^{m-1}, z_{v,q}^{m-1} - z_{v,h,q}^{m-1})_r \right. \\ &\quad \left. + (v_{h,q}^0 - v^0(x_q), z_{v,q}^0 - z_{v,h,q}^0)_r \right],\end{aligned}$$

and

$$\begin{aligned}\rho_Q &= \sum_{m=1}^{N_t} \int_{T_m} \int_{\Omega_{el}} B_x(u_h^m, v_h^m)(z_v^{m-1} - z_{v,h}^{m-1}) dx dt \\ &- \sum_{m=1}^{N_t} \int_{T_m} \sum_{q=1}^{N_{quad}} w_q B_{x_q}(u_{h,q}^m, v_{h,q}^m)(z_{v,q}^{m-1} - z_{v,h,q}^{m-1}) dt \\ &+ \sum_{m=1}^{N_t} \int_{\Omega_{el}} (v_h^m - v_h^{m-1}, z_v^{m-1} - z_{v,h}^{m-1})_r + (v_h^0 - v^0, z_v^0 - z_{v,h}^0)_r dx, \\ &- \sum_{m=1}^{N_t} \sum_{q=1}^{N_{quad}} w_q \left[(v_{h,q}^m - v_{h,q}^{m-1}, z_{v,q}^{m-1} - z_{v,h,q}^{m-1})_r \right. \\ &\quad \left. + (v_{h,q}^0 - v^0(x_q), z_{v,q}^0 - z_{v,h,q}^0)_r \right],\end{aligned}$$

by replacing the integration in Ω_{el} with the trapezoidal rule. The discrete weighted dual residual ρ_h^* and the dual quadrature error ρ_Q^* are defined analogously.

Refinement	$J(u) - J(u_h)$	conv. rate	estimator	conv rate	efficiency
1	-1.713	-	-0.6475	-	0.378
2	-0.749	1.1936	-0.38	0.768	0.507
3	-0.2144	1.8048	-0.1766	1.106	0.824
4	-0.05336	2.0065	-0.05518	1.678	1.034
5	-0.01208	2.1417	-0.01436	1.942	1.188
6	-0.0019	2.667	-0.00364	1.98	1.913

Table 4.6: Behavior of exact error and error estimators for 1C discharge.

Due to this splitting every error contribution can now be uniquely assigned to the mesh $\mathcal{T}_{hom,h}$ or $\mathcal{T}_{r,h}$ respectively. The quadrature errors can be treated in the same way as the previous quadrature error e_q and therefore indicate a needed refinement on the mesh $\mathcal{T}_{hom,h}$.

By this procedure therefore error contributions for every cell on both meshes can be calculated. Based on these error contributions, the same refinement strategy as in section 3.5.2 is used on both meshes at the same time.

4.3.2 Efficiency of error estimator

To test the quality of the error estimators, they will be compared to the exact error in the following. This will be done for the example of the cathode half cell, as described in section 4.1.3. Since for this half cell no exact solution is known, the exact error is approximated using a reference solution, calculated on a very fine grid, with 7 global refinement steps for both domains Ω_{hom} and Ω_r . In order to get rid of the temporal error, the reference solution is calculated for the same time discretization as the actual simulation. For the time discretization, equidistant time intervals of length $k_m = k$ is used.

A comparison of the error estimator and the exact error (reference error) is done, by calculating the efficiency of the error estimator.

Definition 4.3.16 (Efficiency of error estimators). *The efficiency of an error estimator η_h is defined as the quotient between the error estimator and the exact error.*

Due to this definition, an efficiency of close to 1, would show an ideal estimation of the error.

In tables 4.6 and 4.7 the exact error $J(u) - J(u_h)$, the error estimators and the efficiency is shown for two different cases, once a 1C discharge rate with $k = 1$ and once a 10C discharge cycle with $k = 0.1$. Furthermore, the convergence rate with respect to the space error of both, the exact error and the error estimators

Refinement	$J(u) - J(u_h)$	conv. rate	estimator	conv rate	efficiency
1	-8.448	-	-4.349	-	0.515
2	-3.909	1.11	-2.041	1.09	0.522
3	-1.236	1.66	-0.9814	1.152	0.743
4	-0.3310	1.9	-0.3161	1.539	0.955
5	-0.08127	2.03	-0.0896	1.819	1.103
6	-0.0171	2.25	-0.0236	1.92	1.383

Table 4.7: Behavior of exact error and error estimators for 10C discharge.

is calculated. For these results, a simulation starting with a once global refined mesh in both directions is used, which is refined globally in every step.

Both tables show that the efficiency is close to 1, which means that the error estimators have an ideal efficiency. Furthermore, mentioning that the absolute value of the exact functional is $J(u) = 10742$ for the 1C case and $J(u) = 429.3$ for the 10C case, it can be observed that especially in the 1C case the relative error is very small, even on the coarsest mesh. The coarsest mesh consists of 4 cells in direction of the homogenized domain Ω_{hom} and 2 cells in the particle mesh Ω_r .

This means that for the chosen goal functional, there is no need for a fine mesh, if the discharge rates are small. This can be further shown by comparing the potential curves of the reference solution and the solution on the coarsest mesh, as depicted in figure 4.2.

4.3.3 Mesh adaptivity

As discussed before a very coarse mesh consisting of only 4 mesh cells in Ω_{hom} and 2 cells in Ω_r is good enough to get a relative error of smaller than 1%, for small discharge rates. For large discharge rates, like the 10C discharge, this does not hold true. Therefore, in this section, the quality of the error estimators as refinement indicators for mesh adaptivity is investigated. In order to do so, all contributions to the error estimators are assigned to a specific mesh. This assignment is evident in the case of the residuals ρ_h and ρ_h^* . The remaining error contributions e_Q , e_Q^* and e_q correspond to quadrature errors, introduced by replacing the integration over the domain Ω_{el} by a cell-wise trapezoidal rule. It is evident that this quadrature error should get smaller, if the homogenized mesh $\mathcal{T}_{h,hom}$ is refined, since cell-wise trapezoidal rule is defined with respect to this mesh. Therefore, these error contributions are also assigned to the homogenized mesh.

To define the local error indicators, all error contributions are calculated cell-

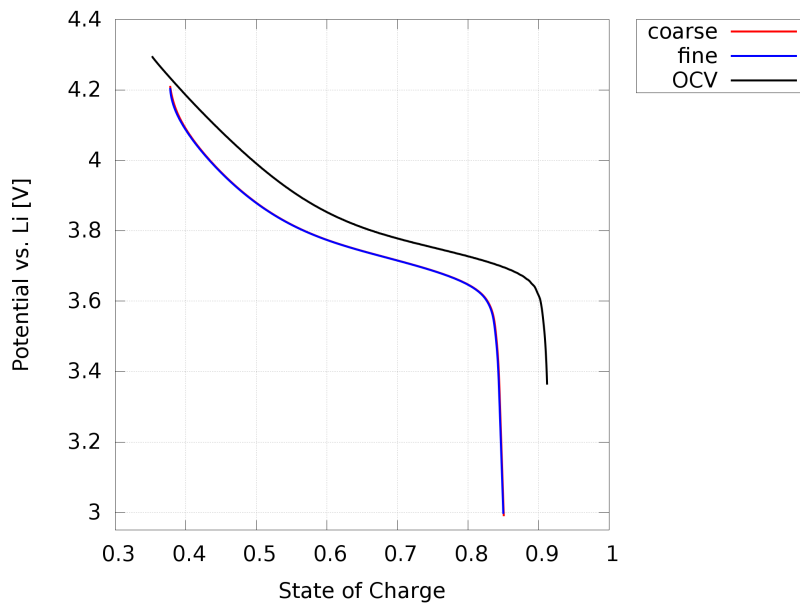


Figure 4.2: Comparison of the potential curve calculated on the coarsest mesh (103 dofs) and the reference mesh (167053 dofs).

wise on their respective meshes. The refinement strategy is chosen to be the same strategy as in the case of the calculation of effective parameters, described in section 3.5.2.

Since this simulation is done for a coupling of two one-dimensional meshes, the refinement over the refinement cycles can be explicitly shown. This is done for the same cases, as before starting with a coarse mesh of a single global refinement of each mesh. In figures 4.3 and 4.4, the refinement of the meshes are shown for the 1C discharge case. Table 4.8 shows the corresponding values of the exact error, calculated with the reference solution, as described in the previous section, and the values of the error estimators.

The table shows that the efficiency of the error estimator is similar to the case of global refinement. Therefore, it can be concluded that the above shown error estimators are suited to work as refinement indicators.

The figures show the refinement of the homogenized mesh and the particles mesh. In these figures, the x axis corresponds to the length of the domains Ω_{hom} and Ω_r respectively, while the y axis shows the different refinement steps. The transition between separator and cathode is given at $x = 50\mu m$.

The figures show that the particle mesh only needs refinement close to the surface of the sphere. The homogenized mesh is only refined in the cathode, but not in the separator.

#dofs	$J(u) - J(u_h)$	estimator	efficiency
103	-1.731	-0.648	0.378
133	-0.76	-0.458	0.603
269	-0.22	-0.216	0.979
369	-0.0625	-0.103	1.646
931	-0.0185	-0.0267	1.442
2945	-0.00373	-0.00734	1.967

Table 4.8: Behavior of exact error and error estimators for 1C discharge with local refinement.

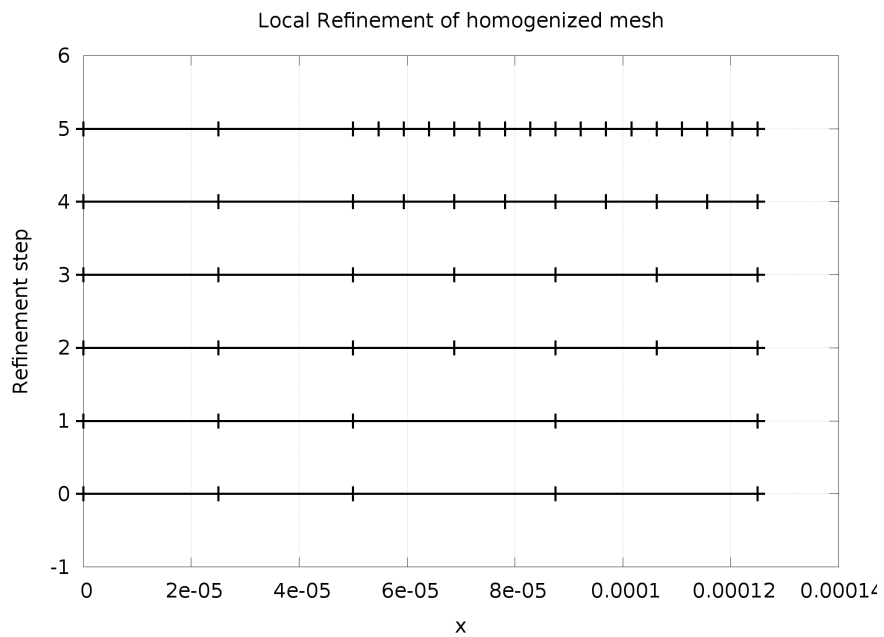


Figure 4.3: Local mesh refinement of the homogenized domain for a 1C discharge rate.

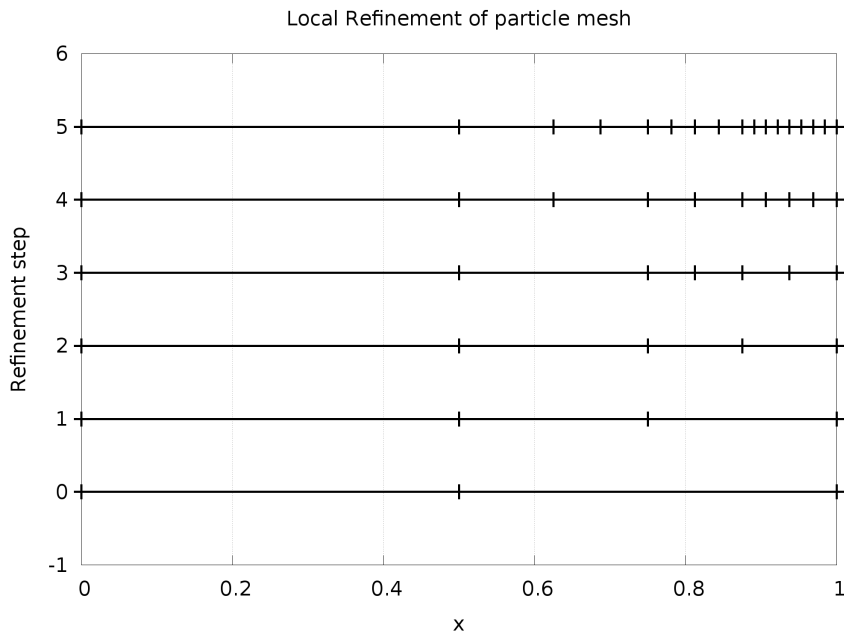


Figure 4.4: Local mesh refinement of the particle domain for a 1C discharge rate.

Figures 4.5 and 4.6 and table 4.9 show the corresponding results for the 10C discharge case.

#dofs	$J(u) - J(u_h)$	estimator	efficiency
103	-8.448	-4.349	0.515
219	-3.911	-2.049	0.524
269	-1.316	-1.388	1.055
661	-0.373	-0.492	1.321
931	-0.129	-0.249	1.938
2435	-0.0434	-0.079	1.822

Table 4.9: Behavior of exact error and error estimators for 10C discharge with local refinement.

The local mesh refinement for the 10C discharge case shows a similar behavior to the 1C discharge case. The homogenized mesh is again only refined in the cathode, but not at all in the separator, while the particle mesh is only refined at the boundary of the sphere.

Finally in figures 4.7 and 4.8 a comparison between the error behavior with global refinement and with local refinement is done. In these figures the absolute value of the exact errors $|J(u) - J(u_h)|$ are shown with respect to the number of used

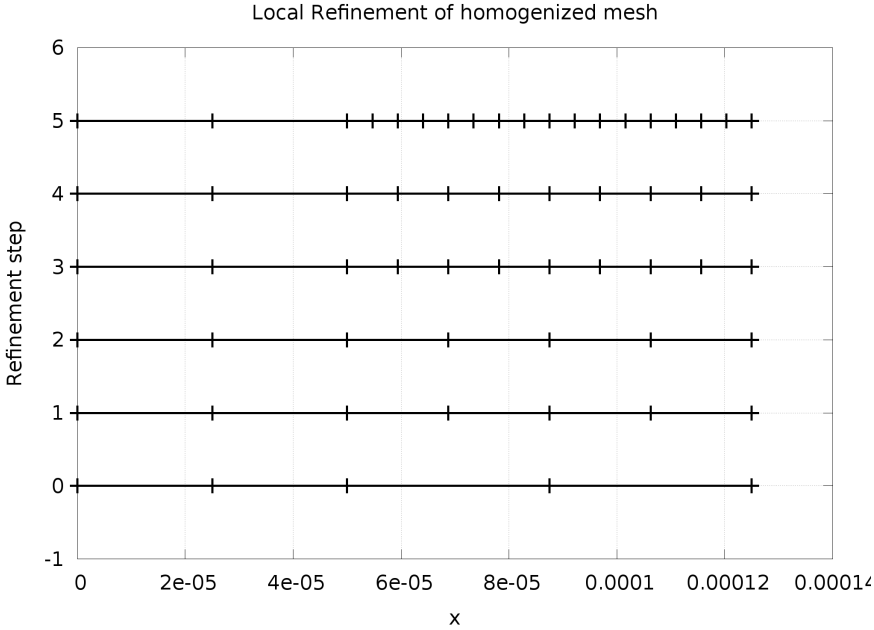


Figure 4.5: Local mesh refinement of the homogenized domain for a 10C discharge rate.

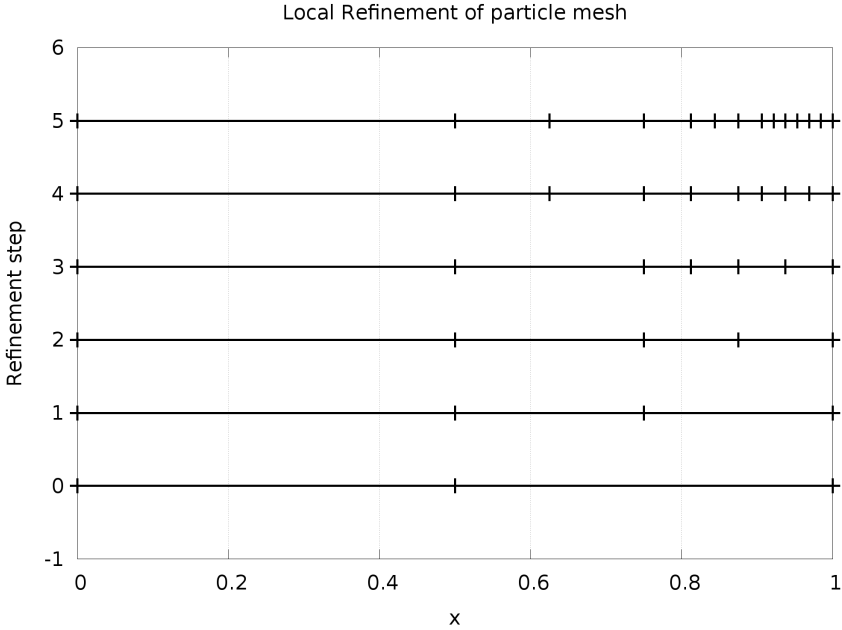


Figure 4.6: Local mesh refinement of the particle domain for a 10C discharge rate.

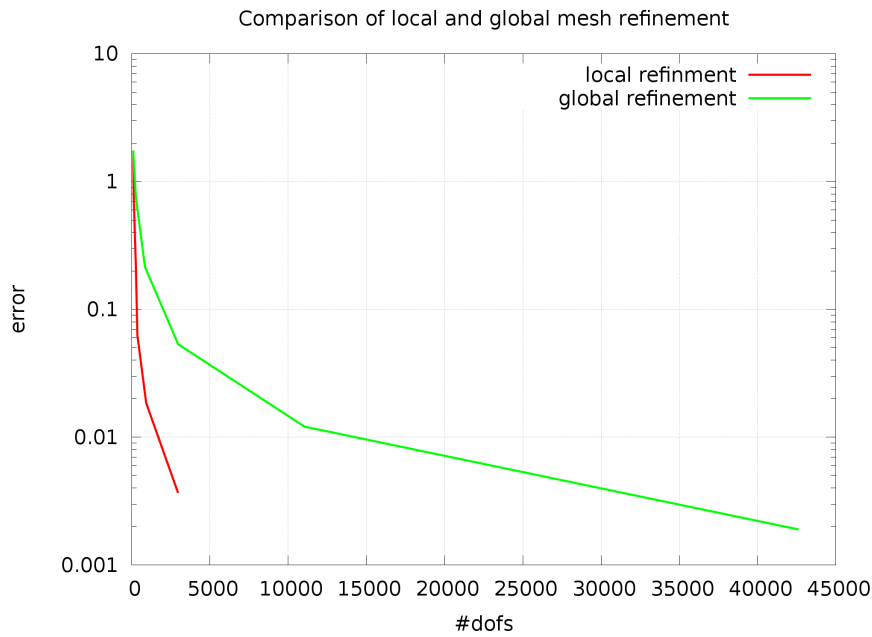


Figure 4.7: Comparison of the error $|J(u) - J(u_h)|$ for local and global mesh refinement for a 1C discharge cycle.

degrees of freedom.

In both figures it is shown that by this local refinement procedure the number of degrees of freedom can be reduced significantly for similar error values.

4.4 Behavior of LIB model

In this section the behavior of the half cell is investigated. As mentioned before the goal functional of the simulation is the potential of the half cell. Therefore, this potential will be shown here for a discharge cycle with different discharge rates between a 0.5C rate (theoretically fully discharged in 2 hours) and 10C rate (theoretically fully discharged in 6 minutes). Beside the potential curves, also the behavior of the concentration of lithium in the active material is investigated. This is done for both a cathode half cell, as described in section 4.1.3 and afterwards for an anode half cell to compare the differences between anode and cathode. According to the results of the previous section 4.3, the refinement was chosen to be 3 times global refinement for the homogenized domains in both separator and electrode and also 3 times global refinement for the particle mesh. With these coarse meshes the simulation time is still small, since there are only few degrees of freedom (~ 1000), but the error in the goal functional is negligible,

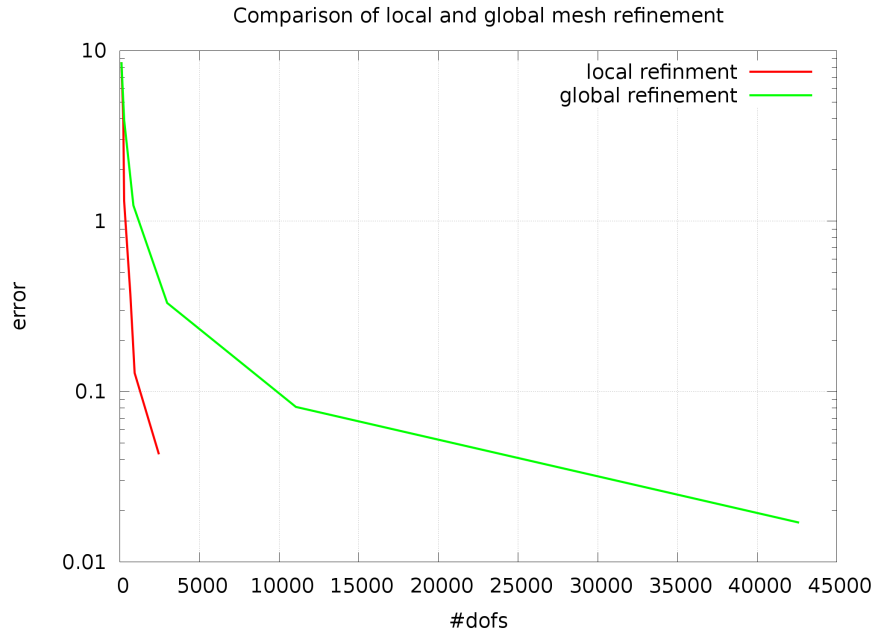


Figure 4.8: Comparison of the error $|J(u) - J(u_h)|$ for local and global mesh refinement for a 10C discharge cycle.

even for big discharge rates.

For the cathode half cell described in section 4.1.3 the potential curves are depicted in figure 4.9. Beside the potential curves in this figure the OCV curve is depicted as the black curve. The x axis for these figures describes the state of charge, which will be defined as the mean lithium concentration in the active material.

The maximal lithium concentration in the active material $c_{s,max}$ is a theoretical value, given by the manufacturer of the battery. During charging and discharging the structure of the active material changes in the first few cycles. Therefore, the theoretical maximal concentration cannot be reached anymore when discharging the battery. This results in the fact that after a few cycles the right limit of the OCV curve are at a maximum of less than 1. Furthermore, if too much lithium were deintercalated from the active material, the chemical structure would be destroyed irreversibly. This effect also influences the left limit of the OCV curve to the extend that the minimum value is larger than 0.

This figure shows that all potential curves reproduce the curvature of the OCV curve to some extend. The big difference is the fact that the simulation stops at different states of charge, where larger discharge rates lead to smaller states of charge. This means that the mean lithium concentration in the active material

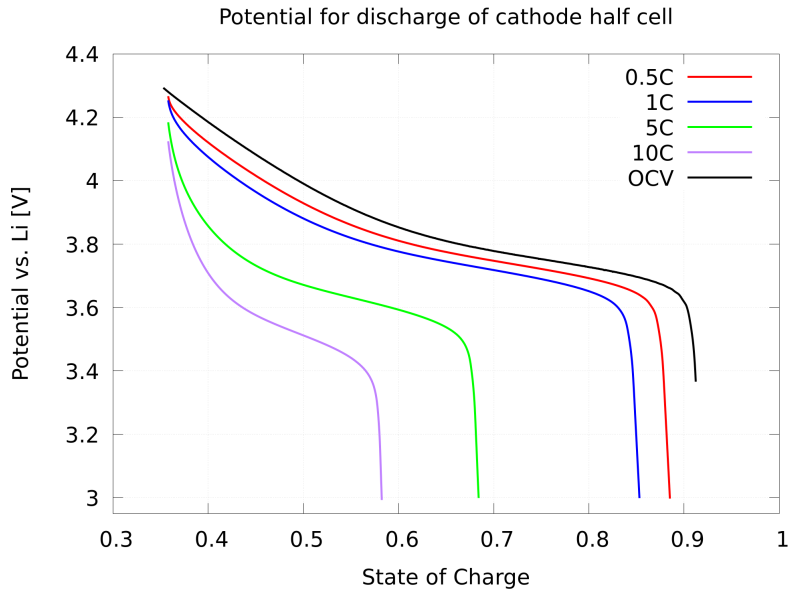


Figure 4.9: Potential curves for different discharge rates of a cathode half cell.

is lower at the end of the discharge cycle for bigger discharge rates.

In order to understand this behavior the lithium concentration in the active material is further investigated. As described in the section 2.3 the active material is reconstructed using spheres with different radii. In the following figures 4.10 and 4.11 the lithium concentration in the active material is shown for different radii and two different points in time. The solid lines show the concentration distribution at time point $t = 100s$ for 1C rate and $t = 10s$ for a 10C rate. The dashed lines show the concentration at time $t = 1500s$ for 1C and $t = 100s$ for a 10C rate. These points in time were chosen such that the behavior can be seen just after the beginning of the simulation and in the middle of the simulation.

The concentration is normalized with respect to the maximal concentration $c_{s,max}$. Furthermore, for the simulation all particle equations are transformed to a unit domain $(0, 1)$, since all particle equations use the same mesh, independent of the radius. These figures show that the concentration in the active material has a big gradient due to the small diffusion in this domain. The diffusion depends on the radius as one would intuitively assume, leading to the fact that for the smallest radius only a small gradient can be seen, while for the largest radius the concentration has a big gradient. For a large discharge rate (10C) the diffusion is even so small that the concentration in the midpoint of the domain keeps unchanged.

This gradient in the concentration leads to smaller states of charge in the poten-

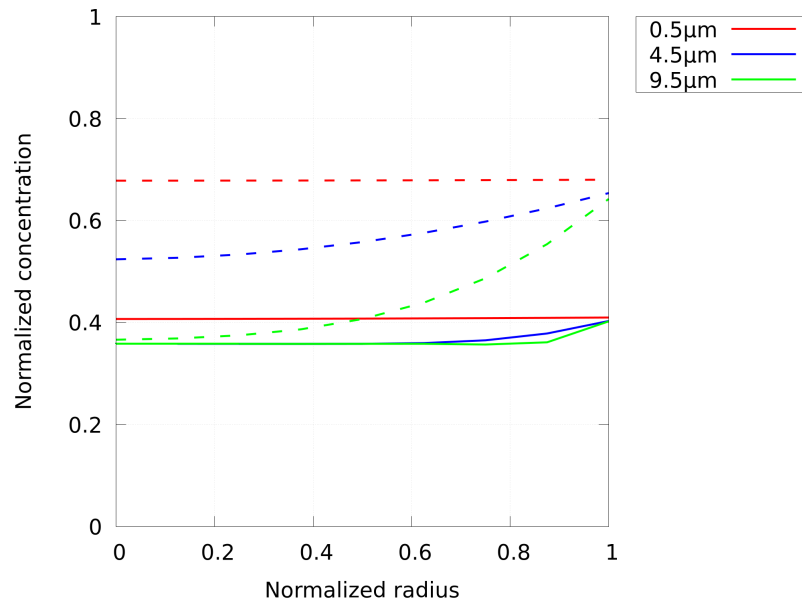


Figure 4.10: Distribution of lithium concentration in the active material in cathode for a 1C discharge cycle.

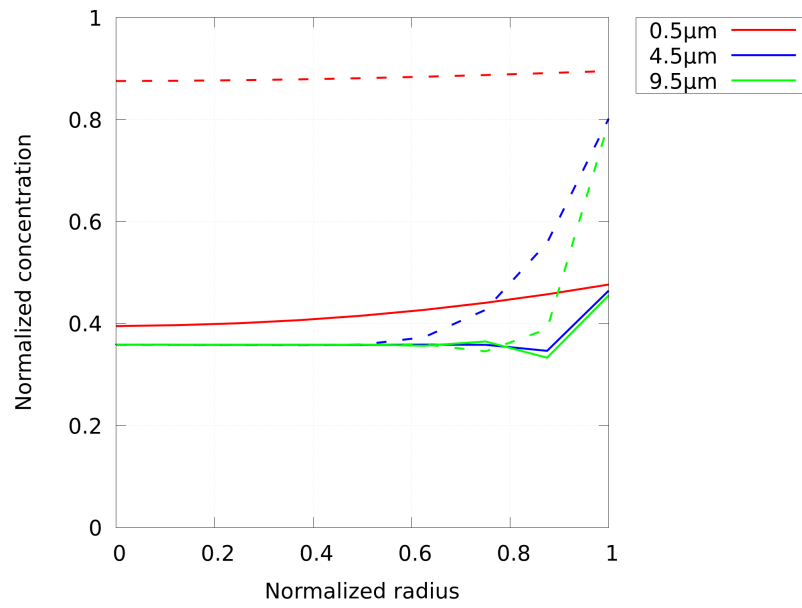


Figure 4.11: Distribution of lithium concentration in the active material in cathode for a 10C discharge cycle.

tial curves 4.9. The potential curves describe the behavior of the potential ϕ_s , which only couples explicitly with the concentration of the active material on the boundary of the spheres, as described before. This means that the concentration inside of the sphere does not influence the potential curves and thus the slow diffusion process inside the active material leads to a capacity loss of the battery.

4.4.1 Anode half cell

Beside a half cell consisting of cathode and a separator, also a half cell consisting of an anode and a separator is considered. The separator for this half cell is the same as for the cathode half cell, which was described in section 4.1.3.

The anode half cell is defined on the domain $\Omega_{hom} = (0, 97.7\mu m)$, where the anode part is defined on the domain $\Omega_{el} = (0, 47.7\mu m)$. The parameter describing the anode are summarized in table 4.10.

Parameter	Value
D_l^{eff}	$1.084 \cdot 10^{-10} \frac{m^2}{s}$
D_s	$10^{-12} \frac{m^2}{s}$
σ_l^{eff}	$0.196 \frac{S}{m}$
σ_s^{eff}	$1000 \frac{S}{m}$
$(1 + \frac{\log(f_{\pm})}{\log(c_l)})$	1
t_+	0.305
a_{spec}	$0.395 \cdot 10^6 m^{-1}$
ε_l	0.352
k	$1.035 \cdot 10^{-8}$
$c_{s,max}$	$35530 \frac{mol}{m^3}$
α	0.5
$c_{l,0}$	$1000 \frac{mol}{m^3}$
T	$298K$

Table 4.10: Anode parameters.

There are two important differences between the cathode and the anode. As seen in the cathode results, figures 4.10 and 4.11, the diffusion parameter in the active material is the most important factor for the capacity loss of the half cell. Comparing this diffusion parameter between anode and cathode, it can be seen that the diffusion is two orders of magnitude faster in the anode. Therefore, the capacity loss should be much smaller in the anode half cell.

Beside this the other difference between anode and cathode parameter is given by the OCV curve, depicted as the black curve in figure 4.12. In comparison to the cathode curve, this one has different limits and a different curvature. The

Radius R_i [μm]	Volume fraction vol_i
1.3	10^{-4}
2.6	$2.41 \cdot 10^{-2}$
3.88	0.2435
5.26	0.2666
6.74	0.1758
8.24	0.1146
9.69	$6.51 \cdot 10^{-2}$
11.22	$4.44 \cdot 10^{-2}$
12.65	$2.43 \cdot 10^{-2}$
14.17	$1.61 \cdot 10^{-2}$
15.68	$4.1 \cdot 10^{-3}$

Table 4.11: Distribution of spheres to reconstruct the active material in the anode.

anode OCV shows several plateaus, which cannot be observed in the cathode case. This behavior of the OCV depends on the used material.

To understand the potential curves correctly it needs to be mentioned that during a discharge cycle the active material of the anode is completely filled with lithium at the beginning of the simulation. Therefore, the state of charge is close to 1 at the beginning and gets smaller as the simulation proceeds, i.e. the potential curve of the anode needs to be read from right to left.

The potential results of the anode depicted in figure 4.12 shows similar behavior to the potential curves of the cathode 4.9. Like in the cathode case the potential curves reproduces the behavior of the OCV curve. The several plateaus of the OCV curve are not reproduces exactly, but are in some way smoothed. This behavior is due to the reconstruction of the active material with a radius distribution instead of a single radius, as was shown by Ender in his work [25].

The capacity loss can also be seen in this figure, but has a much smaller effect in comparison with the cathode. This is due to the fact that in the anode the diffusion in the active material is much faster, as shown in figures 4.13 and 4.14. In these figure the concentration of lithium in the active material is shown for a 1C and a 10C discharge rate. Just like in the case of the cathode, this is done for different radii and different points in time.

These figures show, that the concentration of lithium in the active material is almost constant. Only a small gradient can be seen, if a large discharge rate (10C) is used. This shows, like already assumed, that the reason for the capacity loss is in fact the diffusion inside the active material.

In the anode another effect shows up that could not be observed in the cathode

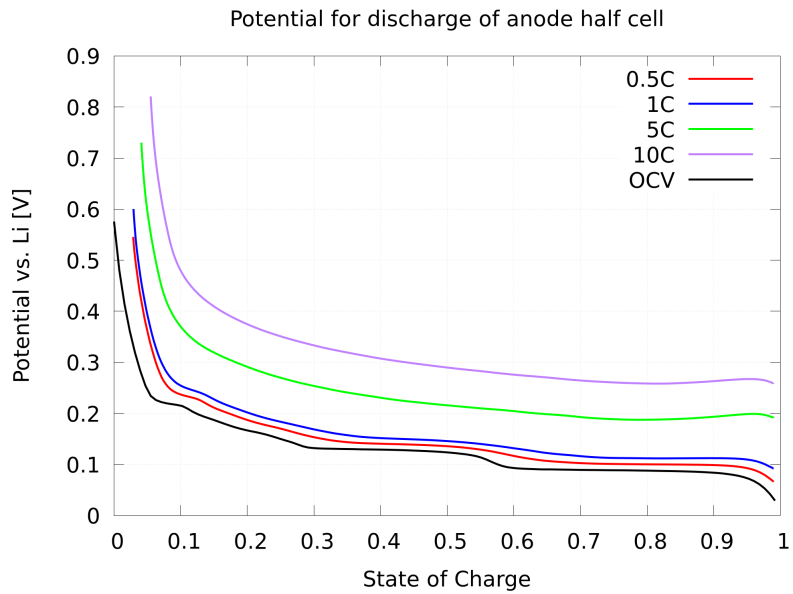


Figure 4.12: Discharge potential of an anode half cell.

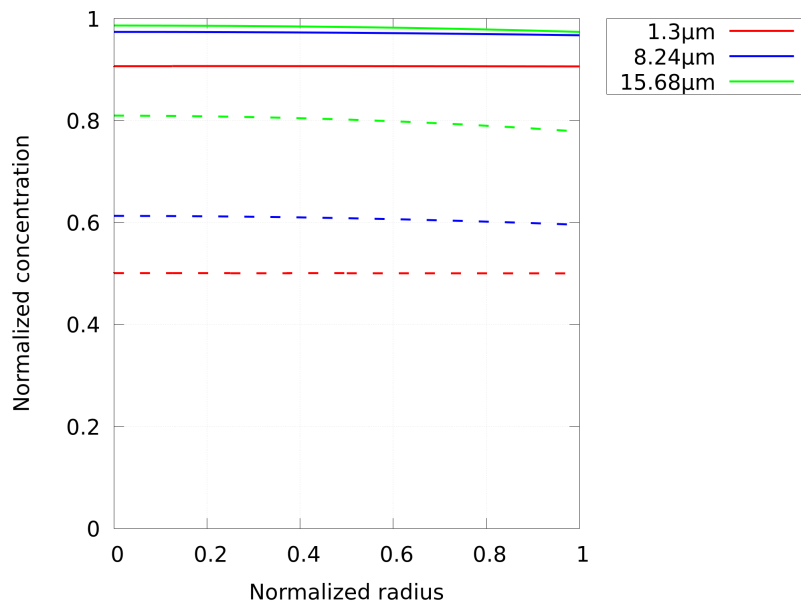


Figure 4.13: Distribution of lithium concentration in the active material in anode for a 1C discharge cycle.

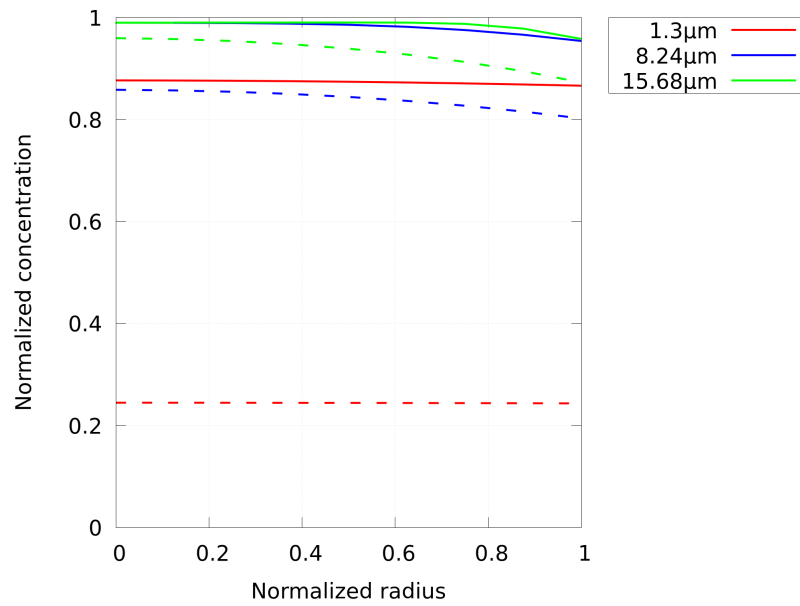


Figure 4.14: Distribution of lithium concentration in the active material in anode for a 10C discharge cycle.

half cell. In the cathode the concentration at the boundary of the active material was at every point more or less the same for every sphere, independent of the radius. Figures 4.13 and 4.14 show the concentration on the boundary has very different values at the same point in time.

In order to understand this behavior better, figures 4.15 and 4.16 show the concentration on the boundary of the spheres as a function over time, again for a 1C and a 10C discharge rate.

In these figures it can be observed that smaller particles are discharged much faster in the beginning of the simulation in comparison to larger spheres. For the 10C discharge rate this behavior continues until the small spheres are discharged almost completely and only then the discharge rate of this particles drops significantly. For the small discharge rate of 1C the behavior is completely different. The small spheres are discharged until a specific concentration is reached and then stop discharging until the concentration in larger spheres reach a similar level. Only then the small spheres continue to discharge. It could be said that the small spheres wait for the large spheres to catch up. Therefore, this behavior will be called “waiting behavior” in the following.

Comparing the concentration, at which this waiting behavior occurs, with the OCV curve it can be observed that there is a connection between the transition between the different plateaus of the OCV and the waiting behavior. The

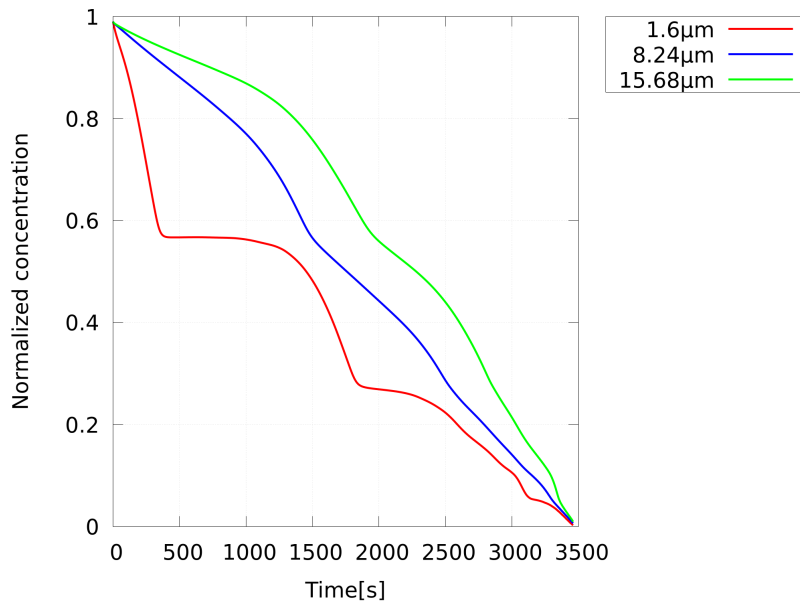


Figure 4.15: Distribution of lithium concentration in the active material over time in anode for a 1C discharge cycle.

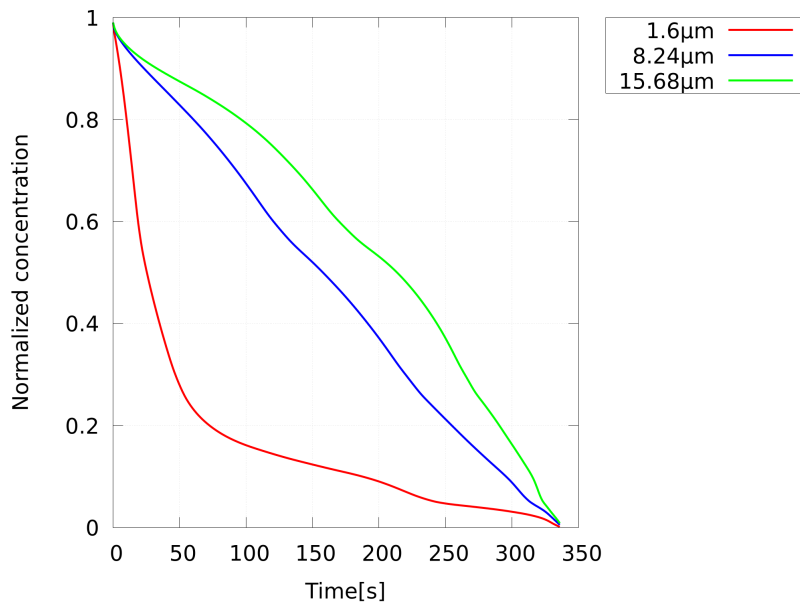


Figure 4.16: Distribution of lithium concentration in the active material over time in anode for a 10C discharge cycle.

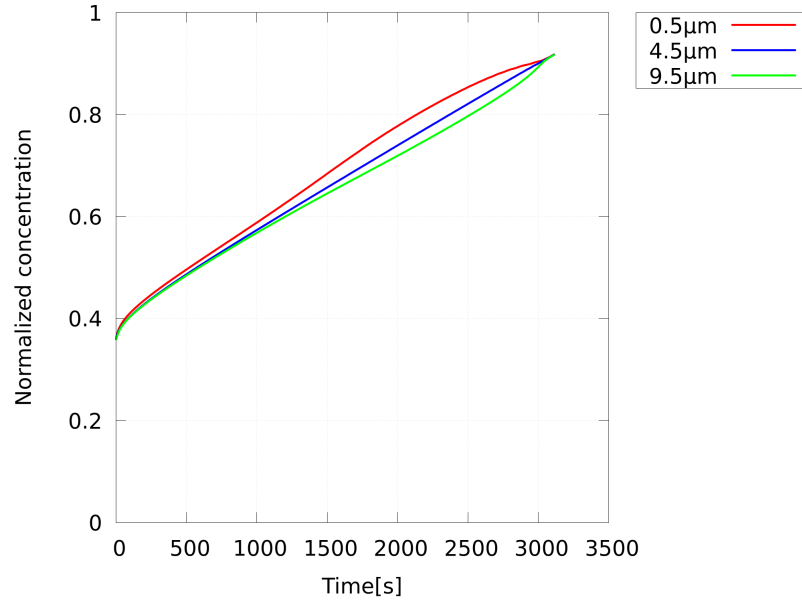


Figure 4.17: Distribution of lithium concentration in the active material over time in cathode for a 1C discharge cycle.

smaller spheres stop being discharged at the concentration corresponding to the transition between the different plateaus. As a comparison figures 4.17 and 4.18 show the corresponding behavior in the cathode, in which no waiting behavior can be observed, but also the OCV shows no plateaus.

In fact this waiting behavior can be explained with the help of the OCV.

Remembering the model equation of the concentration in the active material (4.4) with boundary condition (4.9), it can be observed that the sphere are discharged by the exchange current density j_{ct} at the boundary. The exchange current density is reconstructed by a Butler Volmer equation, where the coefficient only depends of the concentration and the double exponential term depends on the overpotential, which itself depends on the OCV and the potentials ϕ_l and ϕ_s .

The overpotential is described by the term

$$\eta = \phi_s - \phi_l - \phi_{OCV}(c_{s,i}(R_i)) - \frac{RT}{F} \log\left(\frac{c_l}{c_{l,0}}\right), \quad (4.58)$$

where the largest effect is given by the difference $\phi_s - \phi_{OCV}$.

Due to the homogenization process every sphere, independent of the radius, uses the same value for the potential ϕ_s . Since the OCV evaluation depends on the concentration at the boundary of the current sphere, this value can be different for the spheres with different radii.

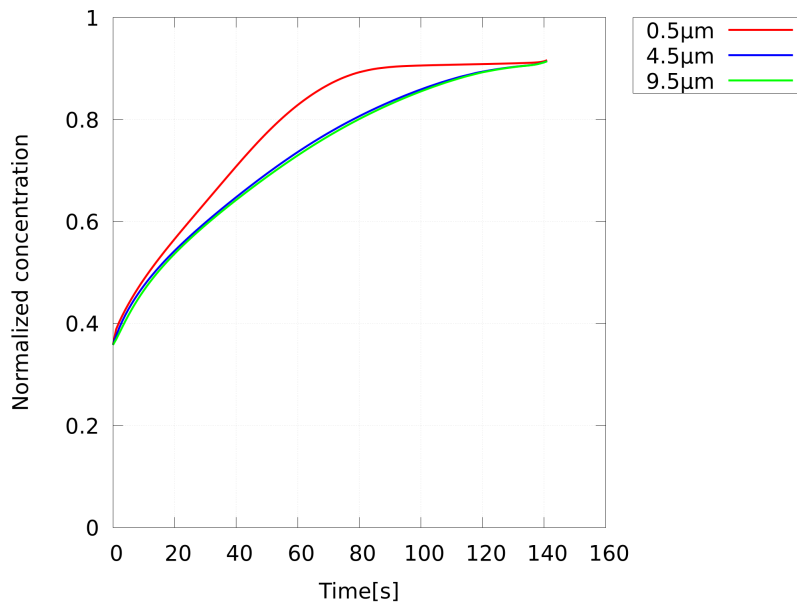


Figure 4.18: Distribution of lithium concentration in the active material over time in cathode for a 10C discharge cycle.

Assuming all spheres have a boundary concentration such that the corresponding values are in the same plateau of the OCV, the difference $\phi_s - \phi_{OCV}$ is roughly the same, since the plateaus are almost constant. Numerical simulations show that the small spheres are discharged faster than larger spheres. Therefore, the boundary concentration is reduced faster for small spheres. When the boundary concentration of small spheres reach the concentration corresponding to the transition between different plateaus ϕ_{OCV} suddenly get larger, and thus the difference $\phi_s - \phi_{OCV}$ suddenly get smaller, as depicted in figure 4.19. When this difference gets smaller and smaller, the overpotential η get smaller and smaller and therefore the exchange current density gets smaller and smaller.

Since the exchange current density is the driving force of discharge behavior of a sphere, the discharge of the sphere stops, if the exchange current density tends to zero. When the larger spheres are charged enough, such that their ϕ_{OCV} value also reaches the transition between the plateaus, the common potential ϕ_s can change appropriately and therefore allowing the difference $\phi_s - \phi_{OCV}$ to get larger for all spheres. Therefore, the small spheres start discharging again until they reach the next transition.

This effect only shows up, if the discharge rate is not too large. In the 10C discharge case, the difference $\phi_s - \phi_{OCV}$ is much bigger than the difference between the plateaus, as can be seen in figure 4.12. Therefore, a transition between

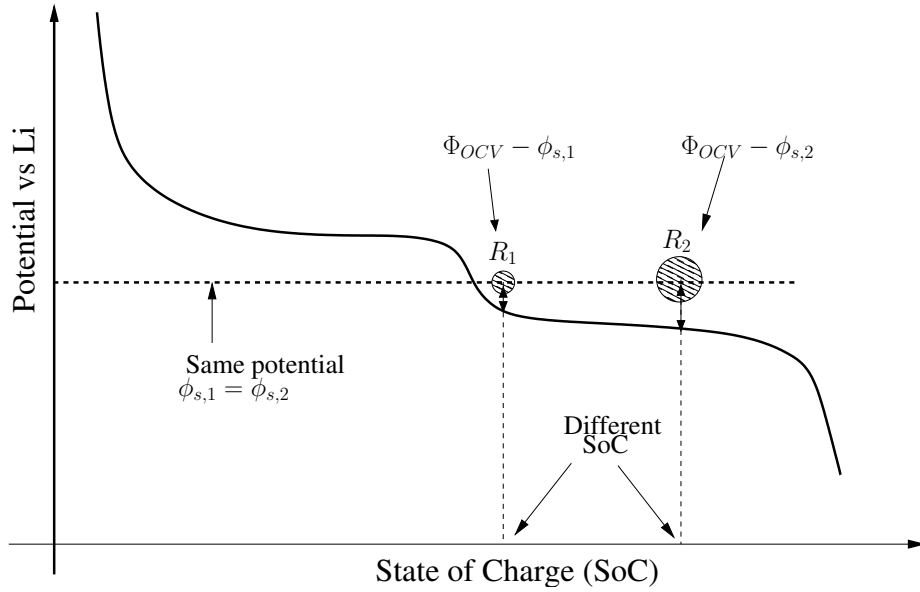


Figure 4.19: Scheme for the explanation of the waiting behavior for an anode OCV.

plateaus has almost no effect on the difference and thus the discharge behavior is not influenced and the waiting behavior does not show up.

The OCV curve of the cathode shows no plateaus, therefore the waiting behavior cannot occur in the cathode case. As depicted in figure 4.20 the difference $\phi_s - \phi_{OCV}$ is in general smaller for smaller spheres. Therefore, the differences balances such that all spheres are discharged steadily.

4.5 Simplified model for small charge/discharge rates

As can be seen from previous results, the concentration $c_{s,i}$ in the particles with the radius distribution R_1, \dots, R_{N_r} is almost constant in the domain Ω_r for small charge currents. Therefore, the influence of replacing the concentration $c_{s,i}$ with its mean value in Ω_r should be small. In this section a simplified model will be derived and by a comparison of this model with the complete model the boundaries of the simplifications will be investigated.

In order to derive the simplified model, the concentration equation of the particles (4.4) will be integrated over the domain Ω_r and a Gaussian theorem will be

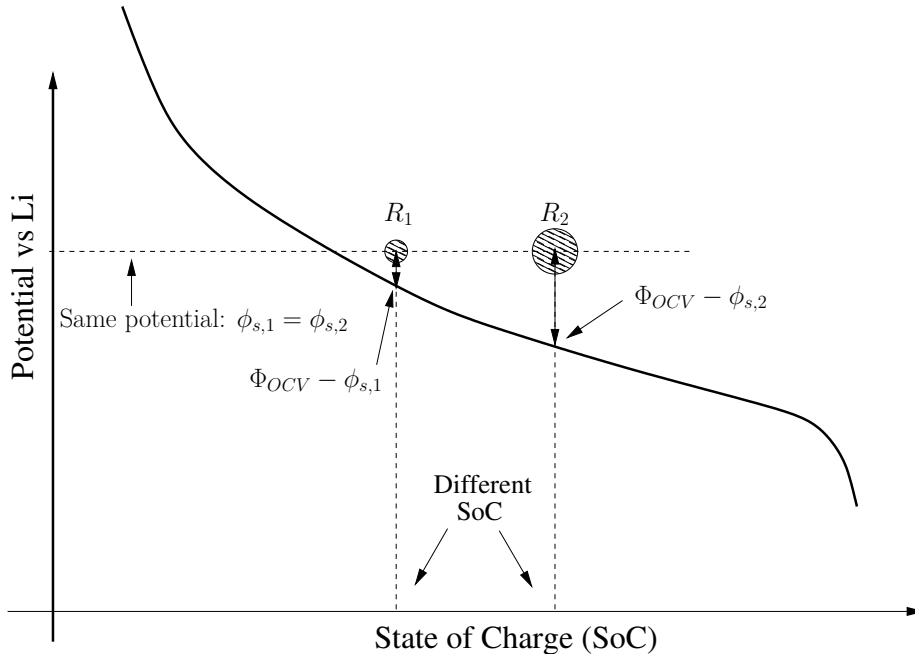


Figure 4.20: Scheme for the explanation of the waiting behavior for a cathode OCV.

used.

$$\begin{aligned}
 \int_{\Omega_r} \partial_t c_{s,i} r^2 dr &= \int_{\Omega_r} \partial_r r^2 D_s \partial_r c_{s,i} dr \\
 &= R_i^2 D_s \partial_r c_{s,i}(R_i) \\
 &= -\frac{R_i^3}{3\varepsilon_{s,i}} \frac{a_{spec,i} j_{ct,i}}{F}.
 \end{aligned}$$

Since the mean value $\overline{c_{s,i}}$ of the concentration $c_{s,i}$ is given by

$$\overline{c_{s,i}} = \frac{3}{R_i^3} \int_{\Omega_r} c_{s,i} r^2 dr,$$

the simplified model reads as follows.

Problem 4.5.1 (Simplified LIB model). *Find solutions*

$$\begin{aligned}
 c_l &\in \mathcal{C}^1(T, \mathcal{C}^2(\Omega_{hom})), \\
 \phi_l &\in \mathcal{C}(T, \mathcal{C}^2(\Omega_{hom})), \\
 \phi_s &\in \mathcal{C}(T, \mathcal{C}^2(\Omega_{el})), \\
 \overline{c_{s,i}} &\in \mathcal{C}^1(T, \mathcal{C}(\Omega_{el})),
 \end{aligned}$$

such that equations (4.1) - (4.3) with boundary conditions (4.5)-(4.8) and the following equation hold true.

$$\partial_t \overline{c_{s,i}} = -\frac{a_{spec,i} \dot{J}_{ct,i}}{F \varepsilon_{s,i}}.$$

This simplified model does not have the P2D character of the original Newman model. Instead this model is a coupled system of a parabolic, two elliptic equations and an ordinary differential equation on a one-dimensional space domain, and will thus be called PDE-ODE model.

The implementation of this simplified model was done during a student project supervised by the author. Instead of a finite element method, this simplified model was discretized using a finite difference scheme in space, [48]. The electrode and the separator were discretized with two equidistant meshes, such that the second derivative in a discretization point $x_i \in \Omega_{hom}$ was approximated by

$$\partial_x \partial_x u(x_i) \approx \frac{u(x_{i-1}) - 2u(x_i) + u(x_{i+1}))}{h^2}, \quad (4.59)$$

with the mesh size h . But the two meshes used different mesh sizes due to their different lengths. Therefore, at the intersection point, between the two meshes, an approximation for non equidistant meshes, as explained in [48], was used,

$$\partial_x \partial_x u(x_i) \approx \frac{2(u(x_{i+1}) - (1 + \frac{h_1}{h_2})u(x_i) + \frac{h_1}{h_2}u(x_{i-1})))}{h_1 h_2 (1 + \frac{h_1}{h_2})} \quad (4.60)$$

where h_1 and h_2 describe the mesh size of the separator and electrode mesh respectively.

The results of this model are shown in figure 4.21. In this figure the potential curves of the PDE-ODE model (dashed) are shown in comparison to the corresponding curve created with the P2D model (solid lines).

For slow discharge rates (0.5C and 1C) the PDE-ODE model and the P2D model produce almost the same potential curves with only minor discrepancy. The fast discharge rates (5C and 10C) show a bigger difference between the PDE-ODE and the P2D models. The main difference there is at the end of the simulation (in the vicinity of $SOC \sim 0$), where the capacity loss is larger for the P2D model. The idea to use the simpler PDE-ODE model instead of the P2D model is based on the observation that the concentration of lithium in the particles is almost constant. It was observed in figures 4.13 and 4.14 that this holds true in the case of slow discharge rates. Although there is a gradient observed for the 10C discharge rate 4.14, the gradient seems to be small enough to not influence the overall behavior of the potential curve. Only at the end of the simulation the influence of the gradient can then be observed due to the bigger capacity loss.

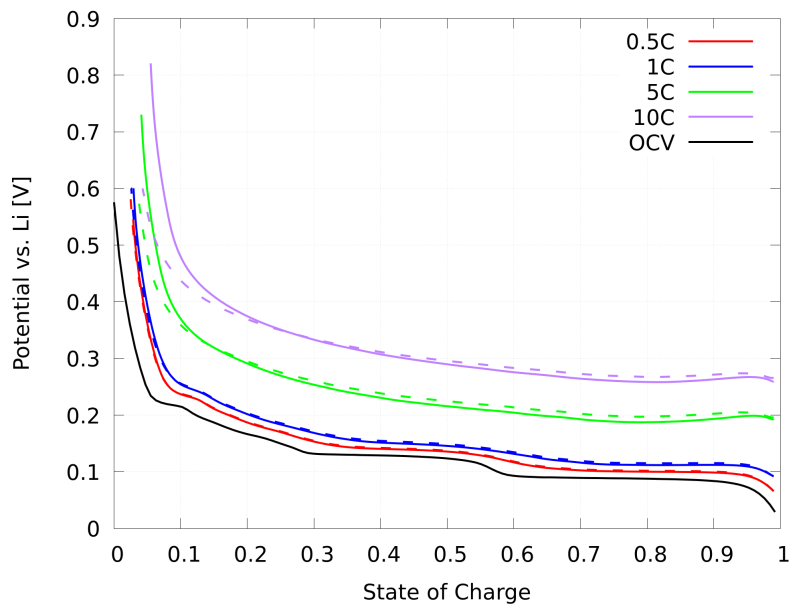


Figure 4.21: Comparison of PDE-ODE model (dashed) and P2D model for different discharge rates of an anode half cell.

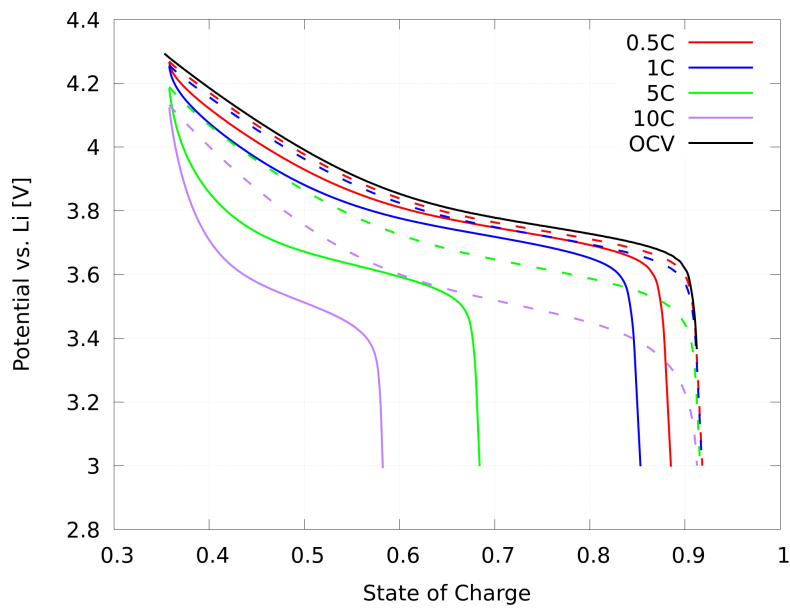


Figure 4.22: Comparison of PDE-ODE model (dashed) and P2D model for different discharge rates of a cathode half cell.

Figure 4.22 shows the difference between the PDE-ODE and the P2D model for a cathode half cell.

It is evident to see that the difference between the PDE-ODE and the P2D model is not negligible. This major difference originates from the fact that the diffusion in the active material is so small that for every discharge rate there is a large gradient in the concentration of the active material, as can be seen in figures 4.10 and 4.11.

Since the PDE-ODE model assumes a constant concentration in the active material, these results also show that the reason for the capacity loss is the diffusion of lithium in the active material.

4.6 Sensitivity of LIB model

In the LIB model there are several parameters that cannot be determined experimentally with a good precision. The reaction rate k , used in the Butler-Volmer equation (4.12), has many different values in literature, [25], [30]. Also the diffusion parameter D_s in the particle equation (4.4) is given in literature with very different values, [25], [30]. The values of the diffusion parameter is even distributed over several orders of magnitude.

Therefore, the sensitivities of the potential curve Φ , defined in definition 4.1.27, with respect to the above mentioned parameters is considered. The sensitivity describes the influence of small changes in a parameter on the potential curve, i.e. the derivative of Φ with respect to the parameter. This sensitivity analysis is a first step in the direction of a parameter estimation process that could not be done in this project.

Since the potential Φ is a function, $T \rightarrow \mathbb{R}$, the sensitivities of this potential will also be a function in time. Therefore, the goal functional is defined for every point in $t \in (0, t_{end})$.

Definition 4.6.1. *For every point in time $t \in (0, t_{end})$, the goal functional for the sensitivity analysis is defined as a mapping*

$$J_t : U \times V \rightarrow \mathbb{R}, \quad (4.61)$$

$$(u, v) \mapsto \Phi(t) = \phi_s(x_{cc}, t), \quad (4.62)$$

with $u = (c_l, \phi_l, \phi_s)$.

The subscript t will be skipped in the following.

In order to embed the calculation of the sensitivities in a mathematical framework, the parameter space $Q \subset \mathbb{R}^2$ is defined. This parameter space is chosen as a subset of \mathbb{R}^2 , since both parameters k and D_s have constant values.

Since the solution of problem 4.1.5 depends on the parameter $q \in Q$, the notation $u = u(q)$ and $v = v(q)$ will be used.

Definition 4.6.2 (Reduced goal functional). *The reduced goal functional is defined as the mapping*

$$j : Q \rightarrow \mathbb{R}, \quad (4.63)$$

$$q \mapsto J(u(q), v(q)). \quad (4.64)$$

With the help of the reduced goal functional, the sensitivity of the goal functional with respect to a parameter $q \in Q$ in direction of $\delta q \in Q$ can be defined.

$$j'_q(q)(\delta q) = \langle J'_u(u(q), v(q)), u'_q(q)(\delta q) \rangle_{U^*, U} \quad (4.65)$$

$$+ \langle J'_v(u(q), v(q)), v'_q(q)(\delta q) \rangle_{V^*, V}. \quad (4.66)$$

In this notation the dual space of U and V was used.

$$U^* := \{f : U \rightarrow \mathbb{R} : f \text{ linear}\}, \quad (4.67)$$

$$V^* := \{f : V \rightarrow \mathbb{R} : f \text{ linear}\}. \quad (4.68)$$

Furthermore, the dual pairing $\langle \cdot, \cdot \rangle_{U^*, U}$ was used.

Definition 4.6.3 (Dual pairing). *Let $u \in U$ be a given function and $u^* \in U^*$ a functional from the dual space, then the dual pairing is defined as*

$$\langle u^*, u \rangle_{U^*, U} = u^*(u). \quad (4.69)$$

The derivatives used here, are Gâteaux derivatives, as defined in definition 4.1.24. The derivatives $u'_q(q)(\delta q)$ and $v'_q(q)(\delta q)$ are the sensitivities of the states u and v . If these derivatives are known, equation (4.65) can directly be computed. Therefore, the goal of the following is the calculation of the sensitivities of the states. In order to keep the notation simple in the following the simplified notation (4.26) and (4.27) is used.

The sensitivities of the states $w_u := u'_q(q)(\delta q)$ and $w_v := v'_q(q)(\delta q)$ are the solution of the following problem.

Problem 4.6.4 (Sensitivities of the state). *Let $u \in U$ and $v \in V$ be given functions. For a given direction $\delta q \in Q$ find the solutions $w_u \in U$ and $w_v \in V$, such that*

$$\mathcal{A}'_u(u, v)(\varphi, w_u) + \mathcal{A}'_v(u, v)(\varphi, w_v) = -\mathcal{A}'_q(u, v)(\varphi, \delta q), \quad (4.70)$$

$$\mathcal{B}'_u(u, v)(\psi, w_u) + \mathcal{B}'_v(u, v)(\psi, w_v) = -\mathcal{B}'_q(u, v)(\psi, \delta q). \quad (4.71)$$

holds true for all $\varphi \in U$ and $\psi \in V$.

The discretization of this problem is done analogously to the discretization described in section 4.1.2 and will therefore not be repeated here.

Problem 4.6.5 (Discrete sensitivities of the state). *Let $u_h \in U_h$ and $v_h \in V_h$ be given functions. For a given direction $\delta q \in Q$ find the solutions $w_{u,h} \in U_h$ and $w_{v,h} \in V_h$, such that*

$$\mathcal{A}'_u(u_h, v_h)(\varphi_h, w_{u,h}) + \mathcal{A}'_v(u_h, v_h)(\varphi_h, w_{v,h}) = -\mathcal{A}'_q(u_h, v_h)(\varphi_h, \delta q), \quad (4.72)$$

$$\mathcal{B}'_u(u_h, v_h)(\psi_h, w_{u,h}) + \mathcal{B}'_v(u_h, v_h)(\psi_h, w_{v,h}) = -\mathcal{B}'_q(u_h, v_h)(\psi_h, \delta q). \quad (4.73)$$

holds true for all $\varphi_h \in U_h$ and $\psi_h \in V_h$.

For further information on the topic of sensitivity analysis the book of Hinze and others is referred, [33].

Remark 4.6.6. *By comparison of this problem with Newton's method shows that the Jacobian matrix used in step (3) of problem 4.1.25 is the same matrix, needed for the solution of problem 4.6.5. This fact can be used to simplify the implementation, since the matrix is already known and only the right hand side has to be adjusted.*

In the following the sensitivities of a cathode half cell and an anode half cell, will be considered. Just like before, both cases will be considered for two different discharge rates, 1C and 10C.

Cathode half cell

The cathode half cell considered here is described in section 4.1.3. The sensitivities of this cathode half cell are calculated in the point $q = (k, D_s) = (4.26 \cdot 10^{-9}, 10^{-14})$. Since the sensitivities for both parameter will be calculated separately, the direction $\delta q = (10^{-9}, 0)$ and $\delta q = (0, 10^{-14})$ are chosen. The absolute values of both directions are chosen such that the sensitivities in both direction are comparable. As before, a discharge cycle of the half cell is considered.

The results are shown in figure 4.23 and 4.24.

In figure 4.23 the results for 1C are shown by the solid curve, while the dashed curve shows the result for a 10C discharge rate. The sensitivities of D_s show in both cases that this diffusion parameter has the largest influence on the goal functional at the end of the solution, close to $SOC = 0.85$ for 1C and $SOC = 0.6$ for 10C. This result is not unexpected, since it has been observed in section 4.4 that diffusion parameter D_s is the reason for the capacity loss. The capacity loss is given by the different state of charges at which the potential curve and the OCV curve show a fast drop or increase. Since a change in the diffusion

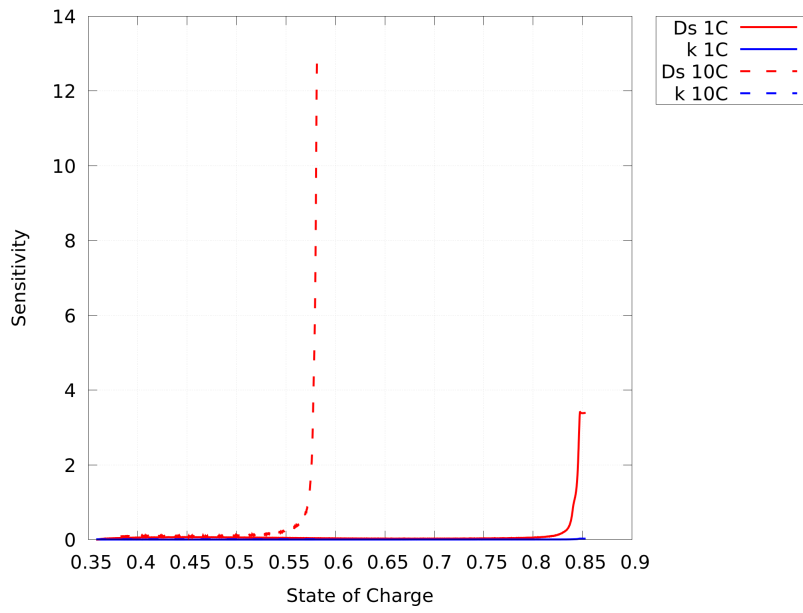


Figure 4.23: Sensitivity of cathode half cell with respect to k and D_s for 1C and 10C discharge rates.

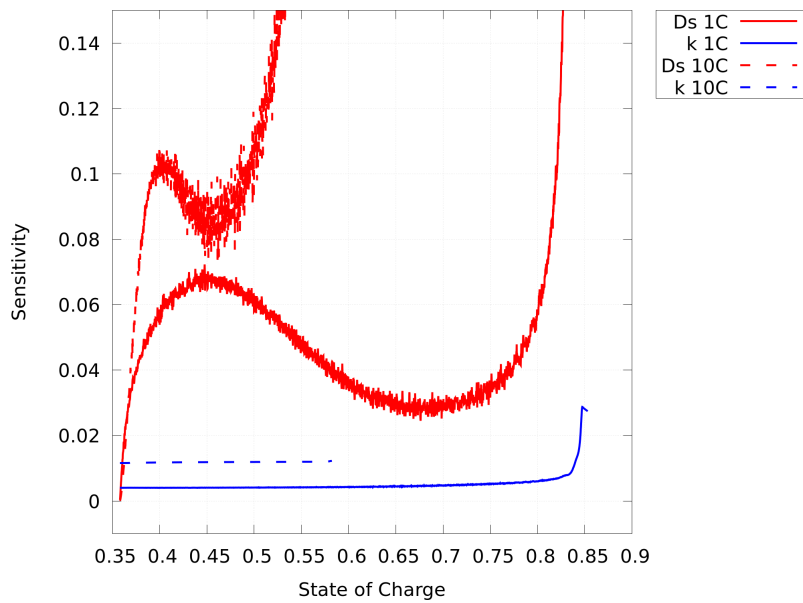


Figure 4.24: Cutout of sensitivity of cathode half cell with respect to k and D_s for 1C and 10C discharge rates.

parameter D_s would change the state of charge that shows the fast drop, the sensitivity at this state of charge has to be large.

The general behavior of the sensitivities of both parameters are almost zero in comparison to the large sensitivity of D_s at the end of the simulation. Therefore, figure 4.24 shows a cutout of the sensitivities. In this figure it can be seen that the sensitivity of k is about one order of magnitude smaller in comparison to the sensitivity of D_s . This shows that the parameter k allows for large changes without a major change in the potential curve.

Furthermore, the sensitivity of D_s shows an oscillatory behavior, which could not be explained in this project.

Anode half cell

The anode half cell is described in section 4.4.1. In this case the sensitivities are calculated at the point $q = (1.035 \cdot 10^{-8}, 10^{-12})$ in directions $\delta q = (10^{-8}, 0)$ and $\delta q = (0, 10^{-12})$.

The results are shown in figure 4.25 and 4.26.

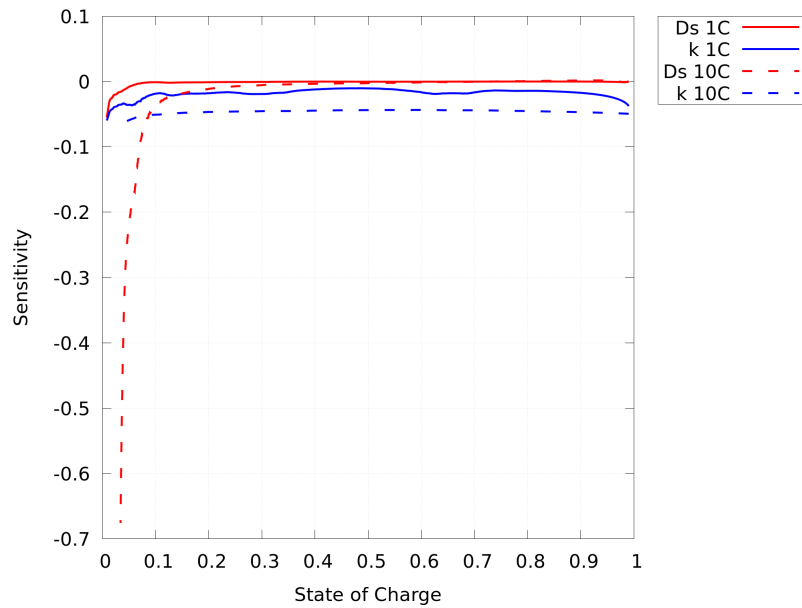


Figure 4.25: Sensitivity of anode half cell with respect to k and D_s for 1C and 10C discharge rates.

The sensitivities of the anode are shown in a similar fashion to the corresponding results of the cathode half cell. It should be mentioned again, that during discharge the anode active material has a *SOC* close to 1 at the beginning of

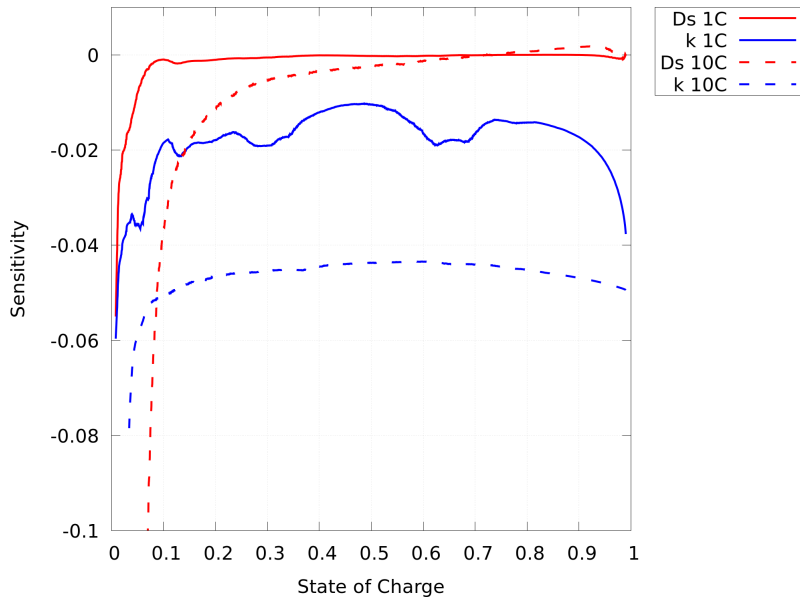


Figure 4.26: Cutout of sensitivity of anode half cell with respect to k and D_s for 1C and 10C discharge rates.

the simulation with a then decreasing SOC . Therefore, these figures need to be seen from right to left.

The results of the anode half cell show a different behavior in comparison to the cathode half cell. The one thing in common is the fact that the diffusion parameter D_s has the largest influence at the end of the simulation. But in the cutout with adjusted y-axis, it can be seen that during the simulation time the parameter k has a larger influence on the goal functional than the diffusion parameter D_s . The difference in comparison to the cathode is the fact that the diffusion parameter is two orders of magnitude faster in the anode. This suggests that both parameters play an important role in the solution process. Which parameter becomes dominant depends on their actual value, since the model is highly nonlinear.

Furthermore, it can be seen that the oscillatory behavior, that could be observed in the cathode does not show up in the anode case.

5 Conclusions

5.1 Conclusions

In this thesis several numerical aspects of the solution process of the extended P2D LIB model, introduced by Ender, were considered. The solution process was divided into two parts, the solution of the cell problem to calculate effective parameter, and the solution of the LIB model.

The cell problem is a Laplace problem on a microstructure with a mixture of Dirichlet and Neumann boundary conditions. This problem was solved with the CutCell method, which was investigated further for this problem setting. In the CutCell method, a mesh consisting of cuboid cells is defined in such a way that the domain of interest Ω is included in the mesh. Due to this definition, the mesh cells can be of three different kinds: fully contained in Ω , partially contained in Ω or not contained at all.

It was shown that the condition number of the stiffness matrix of this problem depends on the distance between the boundary of the domain of interest Ω and the boundary of mesh cells. The boundary of the domain Ω can approach cell boundaries in three different ways in three dimensions, parallel to a cell face, parallel to a cell edge or approaching a single vertex of a cell. If the distance is denoted by the variable ε , it was shown that the condition number behaves like $\mathcal{O}(\varepsilon^{-1})$, $\mathcal{O}(\varepsilon^{-4})$ or $\mathcal{O}(\varepsilon^{-7})$ for the three cases mentioned before. This result was shown numerically.

The upper bound for the condition number was further investigated analytically. In the thesis an upper bound was proven, which was worse than the numerical results, suggesting that the analytical proof is not sharp. It was proven that the condition number behaves like $\mathcal{O}(\varepsilon^{-2})$, $\mathcal{O}(\varepsilon^{-5})$ or $\mathcal{O}(\varepsilon^{-8})$ for the mentioned cases. This means in each case the analytical proof shows an additional negative power in ε .

Furthermore, a goal oriented a posteriori error estimation and its quality as error indicators was investigated. The challenge in this method was the needed reconstruction of the exact dual solution of the problem. The mesh cells were ordered into patches consisting of 8 mesh cells in a hierarchical way. Depending whether a patch is contained in the domain Ω or not a different way of reconstructing the exact dual solution patch-wise was used. In completely contained

patches, the standard approach of a patch-wise higher order interpolation was used. In only partially contained patches, on each cell the dual model was solved new with higher order finite elements. For this cell-wise dual model a Dirichlet condition was used, resulting in the fact that only one degree of freedom is given for each cell. The Dirichlet condition is defined by a mixture of the given lower order finite element solution and the patch-wise higher order interpolated solution where possible.

The quality of this approach and the quality of the error estimators as refinement indicators for local mesh refinement was investigated with several test cases and on real microstructures. The first test case has shown that the error estimator underestimates the exact error. It could be concluded that this underestimation is based on the replacement of the exact dual solution z by a quadratic reconstruction based on the linear solution. This conclusion was made by excluding the other error source. In the error estimator, one term was neglected, but by a numerical test, it was shown that the neglected term does not influence the error estimator in a significant way.

In the second test case the material domain was described by two level-set functions. It was shown that the intersection of the zero isocontour of these level-set functions creates a coupling in the stiffness matrix of the Laplace problem that should not exist. Since the number of cells, in which this wrong coupling occurs does not change significantly under refinement, it was concluded that this effect can also be neglected under mesh refinement.

Furthermore, two real microstructures were considered, a large microstructure consisting of 2822 particles and a smaller microstructure with 100 particles. For the smaller microstructure, it was shown that the error estimators underestimate the error, but they work as refinement indicators for local mesh refinement. In comparison with global mesh refinement, it was shown that the number of degrees of freedom is a factor of about 10 larger in the case of global mesh refinement than in local mesh refinement in order to produce a similar result. The large microstructure did not show this behavior. In this case the same number of degrees of freedom is used in global and local mesh refinement in order to produce a similar result. An explanation for this result may be that the size of the mesh cells was too big in comparison to the size of the particles. Therefore, a further refinement could possibly show the expected behavior like in the other microstructures. Due to computation time limits this result could not be produced and shown in this thesis.

The second big topic in this thesis was the solution process of the extended P2D LIB model by Ender. For this solution process again the condition number of the Jacobian matrix, needed due to applying Newton's method for solving the nonlinearity, was investigated. Due to the homogenization process, three of the model equations are defined on a one-dimensional domain, while one

model equation is defined on a pseudo two-dimensional domain. Both domains have a large difference in size of several orders of magnitude, resulting in a bad conditioning of the Jacobian matrix. It was shown that this bad condition number can be fixed by applying a very easy preconditioner, by a left sided scaling of the Jacobian matrix.

Beside the condition number of the Jacobian the main contribution of the thesis to this topic is the derivation of error estimators for a goal oriented a posteriori error estimation, which was not done before for a model of this pseudo two-dimensional structure. The total error can there be divided into two parts, the temporal error and the spatial error. In this thesis only the spatial error was considered.

To test the quality of the error estimation a reference solution on a very fine mesh was calculated for two different discharge rates. With the help of this reference solution a reference error was calculated by considering the difference between solutions on different meshes with the reference solution. The quality of the error estimation was then investigated by comparing the error estimation with the reference error. This approach showed that the error estimation and the reference error were always within a factor of 10 of each other. Therefore, although the error estimation is not perfect, it is still a good approximation of the actual error.

The goal of this approach was also to investigate the quality of the error estimators as refinement indicators for local mesh refinement. It was shown that the error estimators have very good properties to serve as refinement indicators. This was shown by comparing the reference error between local and global mesh refinement. The reference error for local mesh refinement was in a similar range to the reference error of global mesh refinement, while only using about a tenth of the number of degrees of freedom. Therefore, resulting in a much faster solution process for the same approximation quality.

For the numerical simulations a half cell, a cathode with half a separator, was used, where actually three meshes needed to be defined. One mesh describing the separator, one mesh describing the homogenized domain in the electrode and a third mesh describing the radial domain for the particle equation. The local mesh refinement showed that refinement was mainly needed at the boundary of the mesh corresponding to the particle equations. In the homogenized domain every other refinement step a global refinement in the electrode was done, while the separator mesh was not refined at all.

Beside the numerical aspects of this solution process, also the behavior of the model was considered. The extension by Ender introduced a distribution of different particle sizes, which are all intercalated or deintercalated in a different way. The difference can mainly be observed for an anode half cell. The anode half cell has a open circuit voltage curve, which shows different plateaus. These

different plateaus together with the distribution of different particle sizes, lead to a so called waiting behavior.

Small particles are deintercalated very fast in the beginning of the simulation. When the mean lithium concentration on the boundary of this particle reaches a transition between plateaus in the OCV curve, these particles suddenly stop deintercalating and wait until the larger particles are deintercalated into a similar range. Only then the small particles start deintercalating again. This happens at every transition between plateaus of the OCV curve. This behavior can be explained with the model equations, where it is assumed that all particle equations have the same electrical potential at the boundary. Due to the same electrical potential and different states on the OCV curve, the overpotential, which is more or less the difference between these two functions, shows different values for the different particles sizes, where it tends to zero at the transition of plateaus. Since the overpotential is the driving force of the deintercalation process, this stops the deintercalation of lithium in small particles, until the electrical potential allows a further deintercalation.

Beside this waiting behavior the diffusion process in the particles equations was considered. It was shown that the distribution of lithium concentration in the particles is almost constant for small discharge rates in the anode. Therefore, a simplified model was introduced, where the particle equation was volume averaged leading to an ordinary differential equation for the particles. The total model then was a one-dimensional model, consisting of one parabolic equation, an ordinary differential equation and two elliptic equations.

For this model it was shown that the goal functional is almost not influenced at all using this simplification, if the diffusion in the particles is fast enough. This property was given for the anode, especially at small discharge rates, around 1C. For larger discharge rates in the anode (10C), the simplified model still shows good approximations of the potential curve of the half cell, but it was shown graphically that the approximation error get bigger for larger discharge rates. In the cathode the diffusion process in the particles is too slow, therefore this simplification resulted in a very poor approximation of the goal functional. Therefore, it was concluded that the simplified ODE model can be used for approximating the anode behavior, but could not be used for the simulation of a cathode.

The last contribution of this thesis was a sensitivity analysis of the P2D LIB model. The parameter k , used in the Butler Volmer equation, and the diffusion parameter D_s in the active material cannot be determined experimentally with a good precision. Therefore, a sensitivity analysis for these two parameters was done, which is a first step in the direction of a parameter estimation. The sensitivity analysis showed that the diffusion parameter has a very high sensitivity at the end of the simulation. In the case of the cathode the sensitivity of the

parameter k was significantly smaller in comparison to the sensitivity of D_s , suggesting that a parameter estimation of both parameter at the same time might be problematic. For the anode the sensitivity of k was larger than the one of D_s . This result showed that in the anode the fast diffusion D_s has only a small influence on the potential of the battery, since for the used diffusion parameter the distribution of lithium in the active material was already almost constant.

Acknowledgment

First and foremost I thank my supervisor Dr. Thomas Carraro for this very interesting and challenging PhD topic. Your help and support during the work on my PhD project was extraordinary, I could not wish for a better supervisor for this project. You always had an open door policy, independent of your own work you always took the time to give guidance to your PhD students, especially to me.

A special thanks is required for Dr. Felix Brinkmann and Dr. Hilke Stibbe. The professional and also private discussions we had in the last years were a big support for me. Furthermore, I want to thank the whole Numerical Analysis Group of Prof. Rannacher and the Numerical Optimization Group of Prof. Kostina. For his work on the student project and the implementation of the PDE-ODE battery model, I want to thank Jan Lammel.

My friends, especially Tobias Siekmann, Patrik and Carmen Boettcher, always kept me busy in my private life. Whenever my work felt overwhelming, they had an open ear and listened to my complains, for that you have my deepest thanks. Also the regular board game nights helped me to enjoy life beside the PhD project.

I want to thank my family, my parents Rolf and Liane Wetterauer for their support during my studies and my PhD project. Furthermore, my brother Sören Wetterauer and my nephew Jannik Hartfelder, who kept my private life busy and always made sure, I have enough fun in my private time.

Bibliography

- [1] D. Arndt, W. Bangerth, T. C. Clevenger, D. Davydov, M. Fehling, D. Garcia-Sanchez, G. Harper, T. Heister, L. Heltai, M. Kronbichler, R. M. Kynch, M. Maier, J.-P. Pelteret, B. Turcksin, and D. Wells. The `deal.II` Library, Version 9.1. *Journal of Numerical Mathematics*, 27(4):203–213, 2019.
- [2] I. Babuška and A. Miller. The post-processing approach in the finite element method—part 1: Calculation of displacements, stresses and other higher derivatives of the displacements. *International Journal for Numerical Methods in Engineering*, 20(6):1085–1109, 1984.
- [3] W. Bangerth, R. Hartmann, and G. Kanschat. `deal.II` – a General Purpose Object Oriented Finite Element Library. *ACM Trans. Math. Softw.*, 33(4):24/1–24/27, 2007.
- [4] W. Bangerth and R. Rannacher. *Adaptive Finite Element Methods for Differential Equations*. Springer Basel AG, 2003.
- [5] T. Barth and M. Ohlberger. *Finite Volume Methods: Foundation and Analysis*, volume 1, pages 1–60. John Wiley & Sons, 02 2003.
- [6] R. Becker, M. Braack, and R. Rannacher. Numerical simulation of laminar flames at low Mach number by adaptive finite elements. *Combustion Theory and Modelling*, 3(3):503–534, 1999.
- [7] R. Becker and R. Rannacher. An optimal control approach to a posteriori error estimation. *Acta Numerica*, pages 1–102, 01 2001.
- [8] D. Braess. *Einführung in die Methode der Finiten Elemente*. Springer, 1991.
- [9] J. H. Bramble and J. T. King. A Robust Finite Element Method for Nonhomogeneous Dirichlet Problems in Domains with Curved Boundaries. *Mathematics of Computation*, 63:1–17, 07 1994.
- [10] S. Brenner and R. Scott. *The Mathematical Theory of Finite Element Methods*. Springer-Verlag Berlin Heidelberg, 1994.

- [11] E. Burman. Ghost penalty. *Comptes Rendus Mathématique - C R MATH*, 348, 11 2010.
- [12] E. Burman, S. Claus, P. Hansbo, M. Larson, and A. Massing. CutFEM: Discretizing geometry and partial differential equations. *International Journal for Numerical Methods in Engineering*, 104, 12 2014.
- [13] E. Burman, M. Fernández, and P. Hansbo. Continuous Interior Penalty Finite Element Method for Oseen’s Equations. *SIAM J. Numerical Analysis*, 44:1248–1274, 07 2006.
- [14] E. Burman and P. Hansbo. Fictitious domain finite element methods using cut elements: I. A stabilized Lagrange multiplier method. *Computer Methods in Applied Mechanics and Engineering*, 199:2680–2686, 10 2010.
- [15] E. Burman, P. Hansbo, M. Larson, and S. Zahedi. Cut Finite Element Methods for Coupled Bulk-Surface Problems. *Numerische Mathematik*, 133, 03 2014.
- [16] T. Carraro and C. Goll. A Goal-Oriented Error Estimator for a Class of Homogenization Problems. *Journal of Scientific Computing*, pages 1–28, 2017.
- [17] P. Ciarlet. *The Finite Element Method for Elliptic Problems*. Society for Industrial and Applied Mathematics, 2002.
- [18] F. Ciucci and W. Lai. Derivation of Micro/Macro Lithium Ion Battery Models from Homogenization. *Transp Porous Med*, 88:249 – 270, 2011.
- [19] S. Cooper, A. Bertei, P. Shearing, J. Kilner, and N. Brandon. TauFactor: An open-source application for calculating tortuosity factors from tomographic data. *SoftwareX*, 5:203, 10 2016.
- [20] T. Danner, M. Singh, S. Hein, J. Kaiser, H. Hahn, and A. Latz. Thick electrodes for Li-ion batteries: A model based analysis. *Journal of Power Sources*, 334, 12 2016.
- [21] J. Díaz, D. Gómez-Castro, and A. Ramos. On the well-posedness of a multi-scale mathematical model for Lithium-ion batteries. *Advances in Nonlinear Analysis*, pages 1132 – 1157, 02 2018.
- [22] M. Doyle, T. Fuller, and J. Newman. Modeling of Galvanostatic Charge and Discharge of the Lithium/Polymer/Insertion Cell. *Journal of the Electrochemical Society; (United States)*, 140(6), 1993.

-
- [23] W. Dörfler and M. Maier. An elliptic problem with strongly nonlinear interface condition. *Applicable Analysis*, pages 1–17, 08 2018.
- [24] M. Ender. *Mikrostrukturelle Charakterisierung, Modellentwicklung und Simulation poröser Elektroden für Lithiumionenzellen*. PhD thesis, Karlsruhe Institut für Technologie (KIT), 2014.
- [25] M. Ender. An extended homogenized porous electrode model for lithium-ion cell electrodes. *Journal of Power Sources*, 282:572 – 580, 2015.
- [26] M. Ender, J. Joos, A. Weber, and E. Ivers-Tiffée. Anode microstructures from high-energy and high-power lithium-ion cylindrical cells obtained by x-ray nano-tomography. *Journal of Power Sources*, 269, 11 2014.
- [27] Z. Farkas, I. Faragó, Á. Kriston, and A. Pfrang. Improvement of accuracy of multi-scale models of Li-ion batteries by applying operator splitting techniques. *Journal of Computational and Applied Mathematics*, 310, 04 2016.
- [28] S. Frei and T. Richter. A Locally Modified Parametric Finite Element Method for Interface Problems. *SIAM Journal on Numerical Analysis*, 52:2315–2334, 01 2014.
- [29] T. F. Fuller, M. Doyle, and J. Newman. Simulation and Optimization of the Dual Lithium Ion Insertion Cell. *Journal of The Electrochemical Society*, 141(1):1–10, 1994.
- [30] G. M. Goldin, A. M. Colclasure, A. H. Wiedemann, and R. J. Kee. Three-dimensional particle-resolved models of li-ion batteries to assist the evaluation of empirical parameters in one-dimensional models. *Electrochimica Acta*, 64:118 – 129, 2012.
- [31] A. Hansbo and P. Hansbo. An unfitted finite element method based on Nitsche’s method for elliptic interface problems. *Computer Methods in Applied Mechanics and Engineering*, 191:5537–5552, 11 2002.
- [32] A. Hansbo and P. Hansbo. A Finite Element method for the simulation of strong and weak discontinuities in elasticity. *Computer Methods in Applied Mechanics and Engineering*, 193, 01 2004.
- [33] M. Hinze, R. Pinnau, M. Ulbrich, and S. Ulbrich. *Optimization with PDE Constraints*, volume 23, pages xii+270. Springer, 01 2009.
- [34] U. Hornung, editor. *Homogenization and Porous Media*. Springer-Verlag, Berlin, Heidelberg, 1996.

- [35] T. Hutzenlaub, S. Thiele, N. Paust, R. Spotnitz, R. Zengerle, and C. Fischer-Walchshofer. Three-dimensional electrochemical li-ion battery modelling featuring a focused ion-beam/scanning electron microscopy based three-phase reconstruction of a LiCoO₂ cathode. *Electrochimica Acta*, 115:131 – 139, 2014.
- [36] O. Iliev and P. Zakharov. Domain splitting algorithms for the Li-ion battery simulation. *IOP Conference Series: Materials Science and Engineering*, 158:012099, 11 2016.
- [37] J. L. Y. Cheng, L. Ai, M. Jia, d. shuanglong, B. Yin, S. Woo, and H. Zhang. 3D simulation on the internal distributed properties of lithium-ion battery with planar tabbed configuration. *Journal of Power Sources*, 293:993–1005, 10 2015.
- [38] C. Lang, D. Makhija, A. Doostan, and K. Maute. A Simple and Efficient Preconditioning Scheme for Heaviside Enriched XFEM. *Computational Mechanics*, 54, 12 2013.
- [39] M. Mastali, S. Farhad, M. Farkhondeh, R. Fraser, and M. Fowler. Simplified electrochemical multi-particle model for LiFePO₄ cathodes in lithium-ion batteries. *Journal of Power Sources*, 275, 02 2015.
- [40] MATLAB. *9.7.0.1190202 (R2019b)*. The MathWorks Inc., Natick, Massachusetts, 2018.
- [41] N. Moës, J. Dolbow, and T. Belytschko. A Finite Element Method for Crack Growth without Remeshing. *Int. J. Numer. Meth. Engng.*, 46:131–150, 1999.
- [42] B. Müller, F. Kummer, and M. Oberlack. Highly accurate surface and volume integration on implicit domains by means of moment-fitting. *International Journal for Numerical Methods in Engineering*, 96:512 – 528, 11 2013.
- [43] J. Newman and W. Tiedemann. Porous-electrode theory with battery applications. *AIChE Journal*, 21(1):25–41, 1975.
- [44] S. Osher and R. P. Fedkiw. Level set methods: An overview and some recent results. *J. Comput. Phys*, 169:463–502, 2001.
- [45] T. Richter. *Parallel Multigrid Method for Adaptive Finite Elements with Applications to 3D Flow Problems*. PhD thesis, Heidelberg University, 2005.

-
- [46] M. Schmich and B. Vexler. Adaptivity with Dynamic Meshes for Space-Time Finite Element Discretizations of Parabolic Equations. *SIAM J. Scientific Computing*, 30:369–393, 01 2008.
- [47] N. Sukumar, D. Chopp, N. Moës, and T. Belytschko. Modeling Holes and Inclusions by Level Sets in the Extended Finite Element Method. *Comput. Methods Appl. Mech. Engrg.*, 190:6183–6200, 2001.
- [48] H. Sundqvist and G. Veronis. A simple finite-difference grid with non-constant intervals. *Tellus*, 22(1):26–31, 1970.
- [49] V. Taralova. *Upscaling Approaches for Nonlinear Processes in Lithium-Ion Batteries*. PhD thesis, Technische Universität Kaiserslautern, 2015.
- [50] K. Thomas-Alyea and J. Newman. *Electrochemical Systems*. John Wiley & Sons, 01 2004.
- [51] B. Tjaden, D. J. L. Brett, and P. R. Shearing. Tortuosity in electrochemical devices: a review of calculation approaches. *International Materials Reviews*, 63(2):47–67, 2018.
- [52] D. Westhoff, J. Feinauer, T. Mitsch, I. Manke, S. Hein, A. Latz, and V. Schmidt. Parametric stochastic 3D model for the microstructure of anodes in lithium-ion power cells. *Computational Materials Science*, 126, 01 2017.
- [53] J. Wloka. *Partielle Differentialgleichungen*. Teubner Verlag, 1987.